Dynamical Behaviour of Intrinsic Josephson Junctions

Sajid SALEEM

Department of Electronic and Electrical Engineering

University College London

A thesis submitted for the degree of

Doctor of Philosophy

2010

I Sajid SALEEM confirm that the work presented in this thesis is my own. Where information has been derived from other sources, I confirm that this has been indicated in the thesis.

To My grandparents

Sardaran Bibi (Late) & Muhammad Sharif (Late)

Abstract

Intrinsic Josephson Junctions (IJJs) are the subject of much of research due to their potential applications as high frequency oscillators and detectors in the THz range. A number of previous studies use a single junction model to explain their observations, as no fully agreed model for coupled IJJs exists. The influence of one or more IJJs in the voltage state on other junctions in the IJJ array is not yet fully understood. I have studied the dynamical behaviour of $Tl_2Ba_2CaCu_2O_8$ thin film IJJ arrays, focussing on how one junction in the voltage state influences the other junctions. This I have done by measuring (a) the switching current distributions, and (b) the influence of r.f. irradiation on the DC current-voltage characteristics.

I have compared the switching current distributions when switching from the supercurrent branch with those when switching from the first quasiparticle branch. The supercurrent branch was found to be overdamped at the escape frequency whereas the first quasiparticle branch is underdamped, resulting in a larger switching current for the former than the latter. RF irradiation suppresses the mean switching current on the supercurrent branch accompanied by the appearance of a low-voltage flux flow branch. There is however no effect on the switching current of the quasiparticle branches. I explain these results in terms of the dissipative environment in which the junctions are embedded, and, furthermore, that switching of a single IJJ into the voltage state significantly changes the dissipation. IJJs were sub-

sequently isolated from their environment by FIB-deposited tungsten resistors of resistance between 100 and 500 Ω.

The complete resistor-junction-resistor (RJR) structure is multibranched and shows a change in the DC current-voltage characteristics below and above the T_c of the tungsten. However, the presence of high resistance in the RJR structure at 4.2 K needs further investigation.

Acknowledgements

First and foremost, I would like to record my gratitude and appreciation for my supervisor, Dr. Paul A. Warburton in University College London (UCL) and the London Centre for Nanotechnology (LCN) for his guidance, assistance and most of all for his patience, during the course of this research. Without his supervision and insightful guidance, I would not have gone this far in my PhD research. Furthermore, the research group, Quantum Nanoelectronics Group in LCN in general and Dr Jon Fenton in particular have been extremely helpful and encouraging in facilitating and assisting my PhD research. Mr. Johannes Leiner was a great help during his stay in LCN. I thank our collaborators Professor C.R.M. Grovenor, Dr Susannah C. Speller and Mr. M. Korsah at Oxford University for providing Tl2212 thin film samples. I thank Professor Kazuo Kadowaki and Dr. Takashi Yamamoto of Tskuba University Japan for providing Bi2212 single crystal samples.

I am indebted to the National University of Sciences and Technology (NUST), Pakistan for funding my studies. In addition to this I thank Pakistan Navy for sparing me for the duration of the studies. I also acknowledge the funding support provided by UCL in the form of UCL alumni scholarship 2006/2007 and 2007/2008. The UCL Graduate School provided partial funds for my visit to the ASC 2008 conference, which enabled me to present my work there.

Last but not least, I wish to thank my family and especially my wife and daughter for their support during this research. They always put up with me and enabled me to work with full focus and concentration.

Contents

List of Figures

Chapter 1

Introduction

1.1 Intrinsic Josephson Junctions

Superconductivity was first discovered in mercury in 1911 by Dutch physicist Heike Kamerlingh Onnes of Leiden University. Superconductivity was also discovered in a number of other metallic elements. Collectively these elements are called low temperate superconductors (LTS). The Josephson effect based on LTS was first predicted by Brian D. Josephson in 1962 [Josephson, 1962]. A Josephson junction consists of two superconductors connected by a weak link.

In 1986, Alex Muller and Georg Bednorz discovered superconductivity in a brittle ceramic Ba-La-Cu-O compound at 30 K [Bednorz & Muller, 1986]. A number of other compounds like yttrium barium copper oxide, bismuth strontium calcium copper oxide and thallium barium calcium copper oxide have been found to superconduct at even higher temperatures. The highest superconducting temperature of 138 K was observed in a thallium-doped, mercuric cuprate in 1994. A new family of arsenic based superconducting materials termed oxypnictides has been discovered recently [Takahashi *et al.*, 2008]. These compounds are collectively called high temperature superconductors (HTS).

The standard technique to realise high quality Josephson junctions in LTS is

to fabricate a Nb/AlO_x/Nb tri-layer structure. This technique is routinely used to fabricate junctions for commercial purposes. HTS Josephson junctions can be fabricated using similar tri-layer technique. The quality of these HTS junctions is however poor due to the small coherence length of HTS. A new type of Josephson junction, called the Intrinsic Josephson junction (IJJ) was discovered in HTS in the early nineties [Kleiner *et al.*, 1992]. IJJs exploit the short coherence length in HTS. IJJs are naturally formed by alternating layers of superconducting and insulating material within the unit cell of a cuprate HTS and hence contain no engineered barrier. The stack of layers acts as a combination of a large number of Josephson junctions in series when current flows perpendicular to the cuprate planes.

The fact that IJJs consist of an array of junctions can be exploited to fabricate tuneable oscillators with narrow linewidth in the THz range. THz sources based on intrinsic Josephson junctions have been reported in recent years [Ozyuzer *et al.*, 2007]. The radiated power from these junctions is very small and new methods for enhancing emitted power are under investigation. By coherently coupling many IJJs together, all of which are in the voltage state, it may be possible to achieve high power output levels and narrow linewidths in the THz regime. In addition IJJs may possibly be used as qubits one day. For both THz and qubit applications, it is therefore important to understand the electrodynamics of coupled IJJs and the role of dissipation in an IJJ stack and how this depends upon the number of junctions which are in the voltage state.

In my research I have studied inter-junction coupling in arrays of moderately-damped intrinsic Josephson junctions by measuring the switching current distributions from the supercurrent branch and the first quasiparticle branch at various temperatures. The effect of RF irradiation on the switching current of the supercurrent and the quasiparticle branches is also investigated in order to understand the role of dissipation. Specifically I have studied the dependence of the switch-

ing current upon the microwave field and how this depends upon the number of junctions in the array which are in the voltage state.

1.2 Form of the Dissertation

The next chapter begins with a theoretical review of superconductivity and the Josephson junction. This theory provides the reader with the necessary level of the detail required to follow the experimental and analytical work. Major topics discussed include types of superconducting materials, the Josephson equations, the role of damping in current voltage (IV) characteristics, Josephson junction types, intrinsic Josephson junctions, heating in IJJs and switching current measurements. Chapter 3 discusses the experimental methods and preparatory work carried out. This includes film growth, patterning and IJJ stack fabrication. The measurement setup, including a custom built current source is discussed at the end of the chapter. Chapter 4 contains the experimental results and analysis. The superconductivity of the films, and the general form of the IV hysteresis is discussed. The results of switching current distribution (SCD) measurements are presented and analysed. The effects of RF irradiation on IJJ arrays are analysed. The requirements for environmental isolation of the IJJ stack with FIB-deposited tungsten resistors, approaches for FIB deposition and the effect of resistors on the IV is discussed. Concluding remarks are presented in Chapter 5. A list of references and an appendix is attached.

Chapter 2

Theoretical Details and Background

2.1 Superconductivity

To understand the results and follow the argument presented in the results chapter, it is necessary to have the basic background knowledge required to understand superconductivity. This section will only present the key aspects of the superconductivity related with this work. A very thorough treatment of the subject at an undergraduate level is available in Poole [2007]. Graduate level treatment of the subject is available in for instance Tinkham [1996] or Waldram [1996].

The field of superconductivity was born with the liquefaction of helium in 1908 and the discovery of superconductivity in 1911 by Kamerlingh Onnes. Two major requirements for a material to be considered as superconductor are, (i) zero resistance below a certain temperature and (ii) the ability to expel a magnetic field. The appearance of zero resistance below a certain temperature is the easiest property to be measured. The temperature at which the resistance of the material goes to zero and perfect conductivity appears is termed the critical temperature, T_c.

The second fundamental property of a superconductor is its ability to expel a magnetic field from its bulk at a temperature lower than T_c. This property distinguishes a superconductor from a perfect conductor. A perfect conductor like a pure metal at $T = 0$ K can in principle have zero resistance but it does not have the ability to expel magnetism from its bulk. This effect in the superconductor is termed the Meissner effect after the name of its discoverer in 1933. The magnetic field is screened from the bulk of the superconductor by screening currents flowing on the surface of the superconductor. The screening currents allow the magnetic field to penetrate the superconductor up to a very small length inside the superconductor, termed the penetration depth λ. Screening currents can only screen the magnetic field up to a certain critical field H_c. Any magnetic field value greater than H_c will destroy the superconductivity and the superconductor will return to its normal state.

Not only the external magnetic field but also the dc current flowing in the superconductor can destroy the superconductivity. The critical current density J_c is the maximum current that a superconductor can support. Above J_c the dc current breaks the Cooper pairs, and thus destroys the superconducting state. The supercurrent density is a material property which was first established by Silsbee [1916].

Superconductivity occurs when normal electrons inside the material form pairs and results in a condensate with a lower energy than the normal electrons. A microscopic theory of superconductivity, later termed the BCS theory, was presented in 1957 [Bardeen *et al.*, 1957]. Pippard introduced the concept of coherence length ξ for the superconducting wave function. The coherence length ξ is the length inside which any change to the electron wave function at one point will propagate to the other electrons. BCS theory was based around the formation of Cooper pairs. Cooper in 1956 showed that an attraction between electrons forms Cooper pairs, which have spatial extent of the order of the coherence length ξ

[Cooper, 1956]. Electrons with equal and opposite momentum and spin join to form the Cooper pairs below T_c. The net momentum of the pair is thus zero corresponding to the lowest energy state.

In the superconducting state at $T = 0$ all the Cooper pairs are in the ground state. This is separated from the allowed excited states by an energy gap $\Delta(T)$. BCS theory relates the energy gap at $T = 0$ to the critical temperature where

$$2\Delta(0) = 3.52kT_c \tag{2.1}$$

Pippard suggested that only the electrons within an energy range $\approx kT_c$ of the superconducting ground state take part in the superconductivity. At a non-zero temperature some of the Cooper pairs break and quasiparticles are generated. Quasiparticles include both electron-like and hole-like excitations. With increasing temperature the quasiparticles are excited across the gap and there are fewer Cooper pairs in the superconducting ground state so that $\Delta(T) \rightarrow 0$ at $T = T_c$ and the number of Cooper pairs reduces to zero.

2.1.1 Types of Superconductors

Superconductors can be classified using a number of criteria, e.g, mechanism of superconductivity, material types, elements or compounds, transition temperature etc. One way to classify is how the superconductor responds to an applied external magnetic field. Response to the applied external magnetic field can be predicted by the Ginzburg-Landau parameter κ, which is defined by

$$\kappa = \lambda/\xi \tag{2.2}$$

The supercurrent electron density n_s increases from zero at the boundary of the superconductor to a constant value inside the superconductor and the length scale over which this occurs is ξ. The magnetic field B decays exponentially to zero inside the superconductor with length scale of λ. Superconductors are classified into two main types depending on the value of κ. Type-I superconductors have $\kappa < 1/\sqrt{2}$ and $\kappa > 1/\sqrt{2}$ for Type-II superconductors.

2.1.1.1 Type-I Superconductors

In a Type-I superconductor the coherence length is larger than the penetration depth. Any applied magnetic field up to the critical magnetic field B_c is thus not able to disturb the coherence of the Cooper pairs. Once the applied field value is above the critical field value, the coherence of Cooper pairs is destroyed and the superconductor returns to the normal state.

2.1.1.2 Type-II Superconductors

In a Type-II superconductor the penetration depth λ is larger than the coherence length. In this case the external magnetic field penetrates inside the superconductor up to several coherence lengths. Type-II superconductors screen out all the applied magnetic field up to a value B_{c1}. A magnetic field greater than B_{c1} enters the superconductor in the form of thin lines known as flux lines or vortices. Each vortex contains a quantised amount of magnetic flux which is screened by the circulating currents inside the superconductor. This quantity is known as flux quantum and has a value of $\Phi_0 = h/2e = 2.07 \times 10^{-15}$ Wb.

2.2 The Josephson Junction

A Josephson junction consists of two superconductors connected by a weak link as shown in Figure 2.1. Within a weak link a real wave function exists which is continuous across the superconductor-insulator-superconductor boundaries. In such a weak link the wave functions of the superconductors will overlap each other as shown in Figure 2.1. The Josephson junction is named after Brian D. Josephson who in 1962 predicted that Cooper pairs can tunnel through the classically forbidden region, provided the gap between the superconductors was very small and they were weakly coupled to each other [Josephson, 1962]. Josephson's prediction was soon verified by a number of experiments [Anderson, 1963; Jaklevic, 1964]. In contrast to popular belief at the time, it was shown that the tunnelling rate of Cooper pairs and normal electrons was almost the same.

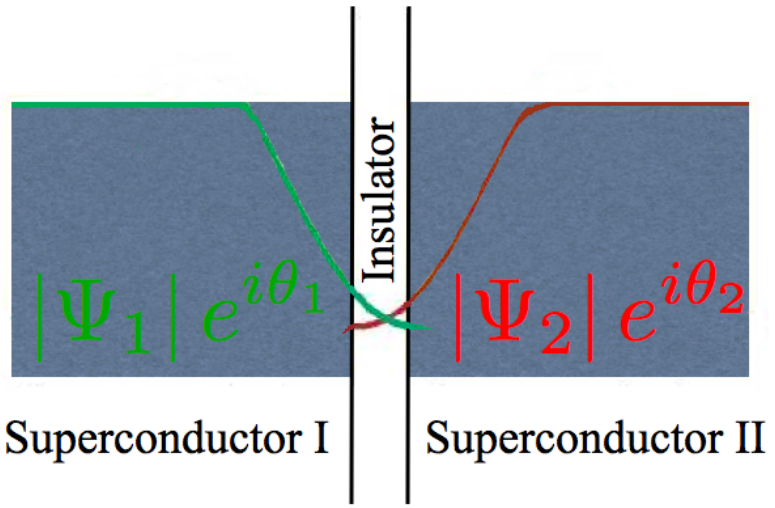

Figure 2.1: Schematic representation of a Josephson Junction.

2.2.1 The Josephson Equations

Josephson predicted that the current through a junction would be a sine function of the difference ϕ between the phases, θ_1 and θ_2, of the two superconductors on either side of the weak link. By following the treatment of Feynman who added

a coupling term and used the Schrodinger equation, one can derive the governing equations of the Josephson junction [Feynman, 1966]. The first Josephson equation is given as

$$I = I_c \sin\phi \tag{2.3}$$

and is called the Current-Phase Relation (CPR). I_c is the Josephson critical current and is the maximum current the structure can support without dissipating power.

The second Josephson equation deals with the application of a constant voltage across the junction. This results in an evolving phase difference between the superconductors. The equation is given as

$$V = \frac{\hbar}{2e}\frac{d\phi}{dt} \tag{2.4}$$

In this case there is an alternating current of amplitude I_c and frequency

$$f_J = \frac{2eV}{\hbar} \tag{2.5}$$

Here $2e/\hbar$ is equal to 483.6×10^{12} Hz/V. The above two effects are known as the dc and ac Josephson effects.

The critical current I_c is a measure of the coupling strength between the two superconductors on the either side of the Josephson junction. This energy depends on how thin the insulating layer is and what material it is made of. The coupling energy in the junction can be inferred from Equation 2.3 and 2.4 by

integrating the electrical work. The coupling energy is found to be [Tinkham, 1996]

$$E_J = \frac{\hbar I_c}{2e} \tag{2.6}$$

I_c scales with the inverse of the junction normal state resistance R_n. Thus, $I_c(T)R_n$ has a fixed value which depends only on the material and temperature and not on the junction dimensions. I_cR_n is used as a measure to check the performance of the junction against the ideal case. The temperature dependence of I_c was calculated by Ambegaokar & Baratoff [1963] for Josephson junctions and is given by

$$I_c(T)R_n = \frac{\pi\Delta(T)}{2e}\tanh[\frac{\Delta(T)}{2k_BT}] \tag{2.7}$$

Figure 2.2 shows the temperature dependence of I_c. At $T = 0$ Equation 2.7 reduces to $I_cR_n = \pi\Delta(0)/2e$. The critical current and conductance of tunnel junctions decrease exponentially with increasing barrier thickness.

2.2.2 Josephson Junction Models

Equation 2.3 and $I_c(T)$ sufficiently describe the zero voltage dc properties of the Josephson junction. Equations 2.3 and 2.4 only describe the ideal case, when all the current is being carried by the electron pairs. However, a more comprehensive model is required to understand the full Josephson junction characteristics. The two mostly used models for the Josephson junction include the RCSJ model (electrical model) and tilted washboard model (mechanical model). Both these models are briefly discussed below.

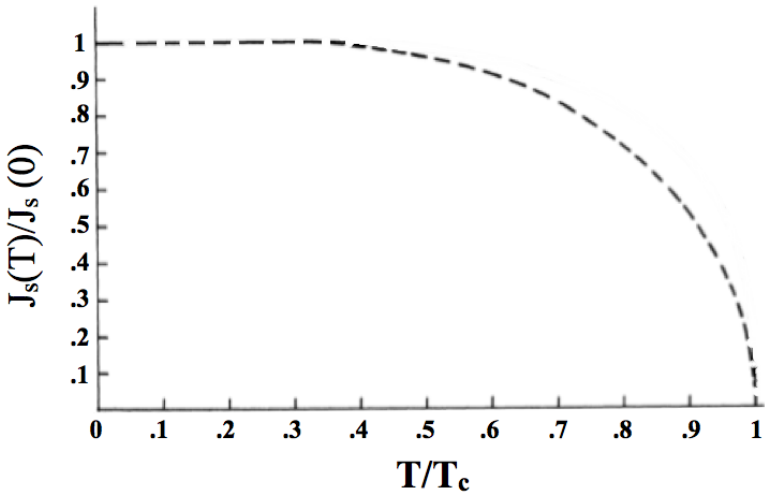

Figure 2.2: Reduced Josephson current density versus reduced temperature. Original Figure from Ambegaokar & Baratoff [1963]

2.2.2.1 RCSJ Model

In the resistively and capacitively shunted junction (RCSJ) model the physical Josephson junction is modelled by an ideal junction (described by Equations 2.3 and 2.4) in parallel with a resistor R and a capacitor C as shown in Figure 2.3. The Josephson junction is represented by the cross in the model. The resistance R builds in dissipation in the voltage state due to quasiparticle tunnelling while C is the geometric capacitance between the two electrodes. In the BCS model conductance is zero below the gap voltage and increases exponentially above the gap. In HTS, conductance is normally approximated by the inverse of normal state resistance R_n. The total current I through the circuit is a combination of the current through the individual components and is given by

$$I = I_J + I_R + I_{cap} \tag{2.8}$$

By using Equation 2.3 and 2.4, this becomes

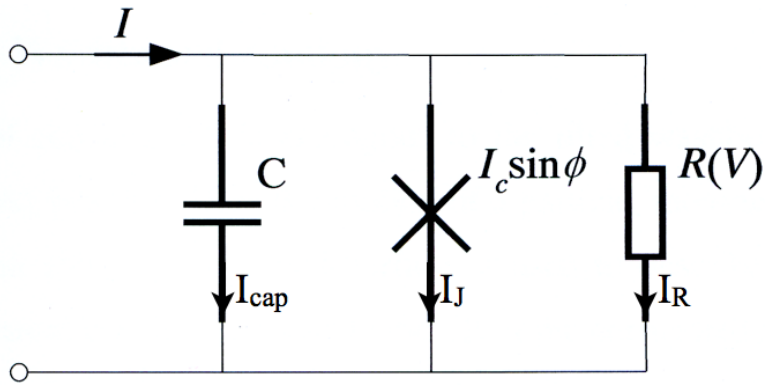

Figure 2.3: The RCSJ model. The Josephson junction is represented by the cross. The total current is the combination of individual component currents.

$$I = I_c \sin\phi + \frac{\hbar}{2eR}\frac{d\phi}{dt} + \frac{C\hbar}{2e}\frac{d^2\phi}{dt^2} \tag{2.9}$$

This is a differential equation for ϕ which is non linear because of the $\sin\phi$ term. At zero temperature, for $I < I_c$, ϕ settles rapidly to a constant stable value. For $I > I_c$ there is no static solution and the phase is time-varying. Hence the voltage has a ac component and also components at all multiples of the Josephson frequency. If we ignore the last term in Equation 2.9 and solve the equation, the product $I_c R_n$ determines the maximum ac voltage amplitude for a given frequency. The dc voltage in this case for $I > I_c$ is given by

$$V = I_c R_n \sqrt{I/{I_c}^2 - 1} \tag{2.10}$$

This is shown graphically in Figure 2.4.

In the RCSJ model, the Josephson junction behaves as an inductor and its inductance is given by

$$L_J = \frac{\hbar}{2eI_c}(1 - (I_J/I_c)^2)^{-1/2} \tag{2.11}$$

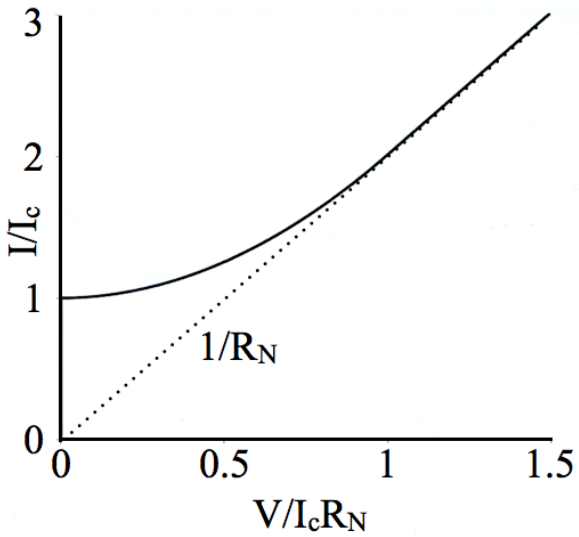

Figure 2.4: Normalised current voltage characteristics of a Josephson junction with C=0.

The RCSJ model can now be compared with a parallel RLC circuit. At a certain frequency the reactive impedances of the Josephson junction and the capacitor become equal. This resonant frequency is termed the plasma frequency and is given by

$$\omega_p = \frac{1}{\sqrt{L_J C}} = \sqrt{\frac{2eI_c}{\hbar C}} \left(1 - \left(\frac{I_J}{I_c}\right)^2\right)^{1/4} \tag{2.12}$$

where as $\sqrt{\frac{2eI_c}{\hbar C}}$ is termed as ω_{p0}. The quality factor Q of the plasma resonance is given by

$$Q = \omega_p RC \tag{2.13}$$

If we take into account the capacitance (i.e the last term of Equation 2.9) then we expect hysteretic behaviour. This was experimentally confirmed by Stewart and McCumber [McCumber, 1968; Stewart, 1968]. If the current is measured in units of I_c, the voltage in units of $V_c = I_c R$, the time in units $\tau_c = (\Phi_0/2\pi I_c R)$,

where V_c is the characteristic voltage and $f_c = 1/(2\pi\tau_c)$ is the characteristic frequency, we can write Equation 2.9 in a dimensionless form:

$$i = sin\phi + \dot{\phi} + \beta_c\ddot{\phi} \tag{2.14}$$

This equation has only a single device-dependent parameter. This is the Stewart-McCumber parameter given by

$$\beta_c = \frac{2\pi I_c R^2 C}{\Phi_0} = Q^2 \tag{2.15}$$

This parameter is a measure of the damping in the system. Damping and how it affects the IV characteristics of the Josephson junction will be discussed later in this section.

2.2.2.2 Tilted Washboard Model

Various mechanical models are used to explain the dynamics of the Josephson junction. These models help to gain an insight which might not come from studying numerical results. A detailed account of the mechanical models is given by Fulton [1977]. The most commonly used model is the tilted washboard model shown in Figure 2.5. This model considers the motion of a fictitious particle on a tilted washboard to model the time dependent behaviour of the Josephson junction. The average slope of the board corresponds to the bias current, the mass of the ball to the capacitance (which is an energy storage factor), and the drag imposed on the movement of ball corresponds to the resistance in the actual junction. The height of the potential barrier is given by $\Delta U{=}(I_c\Phi_0/2\pi)\left[\sqrt{1-x^2} - xcos^{-1}x\right]$ where $x = I/I_{c0}$.

The particle of mass $(\hbar/2e)^2C$ moves along the ϕ axis in an effective potential

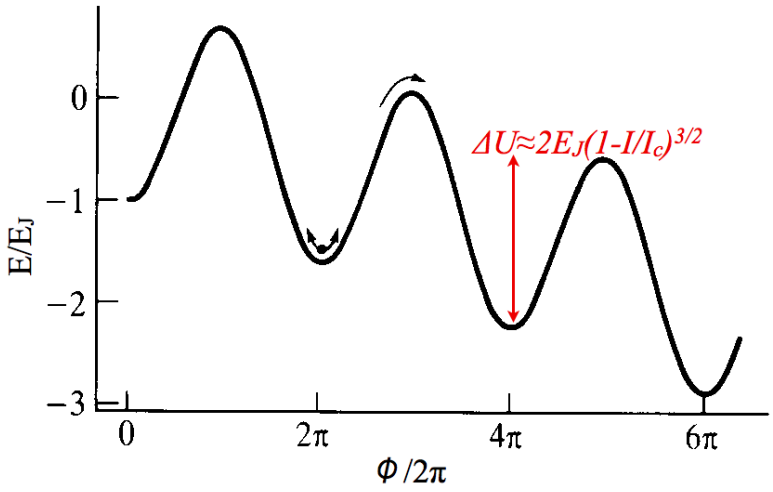

Figure 2.5: The tilted washboard model. The tilt corresponds to the dc current injected. Electrical noise is equivalent to brownian motion. Figure from Tinkham [1996].

given by

$$U(\phi) = -\frac{\hbar}{2e}(I_c cos\phi + I\phi) \tag{2.16}$$

Depending on the bias current, temperature and damping in the system the particle can either be in steady state or running state.

2.2.3 Damping in the Josephson Junction

Damping plays a major role in determining the dynamical behaviour of the junction. It weakly affects the escape rate while the particle (in the tilted washboard model) is at rest in one of the local minima. Its biggest effect, however, is once the particle has escaped from the local minimum. Post-escape behaviour from the local minimum is significantly affected by the damping in the system.

Damping in the Josephson junction is characterised by the McCumber parameter β_c which determines the amount of hysteresis in the system and is defined

in Equation 2.15. It can also be defined in terms of various other parameters

$$\beta_c = Q^2 = \left(\frac{\omega_c}{\omega_p}\right)^2 = \sqrt{\frac{4I_{c0}}{\pi I_{r0}}} = \frac{2\pi I_c R^2 C}{\Phi_0} \tag{2.17}$$

where Q is the quality factor of the junction, ω_p is the plasma frequency, ω_c is the characteristic frequency of the Josephson junction given by $\omega_c = \frac{2e}{\hbar}V_c$ and I_{r0} is the retrapping current. The dynamical behaviour can be divided into different categories based on the damping present in the system.

2.2.3.1 Negligibly damped Junction at $T = 0$

With zero bias current the wash board has a zero average slope and the particle rests in one of the local minimum. As the ball is trapped in a local minima, so $d\phi/dt$ is zero and hence V is zero as well. The height of potential well in this case is given by $2E_J$. When the tilt of the washboard is increased by the application of the bias current the particle starts to gain momentum. While the bias current *(I)* is less than the critical current I_c, the particle does not gain enough energy to overcome the ridge and stays in the minimum. Increasing the bias current increases the tilt of the washboard and at the same time reduces the height of the barrier. The height of the barrier in this case can be approximated to $\Delta U = 2E_J(1 - I/I_c)^{3/2}$. Once the bias current is equal to the critical current, the height of barrier ΔU is zero and the particle can escape. The particle now starts to roll down the washboard and $d\phi/dt$ is non-zero. The average velocity achieved by the particle then corresponds to the junction dc voltage. This is called the running state.

If the bias current is decreased once the particle has entered the running state, the potential barrier starts to rise and local minima start to reappear. The particle is slowed down until it is re-trapped again in one of the minima. The

re-trapping current I_r, is smaller than the critical current due to the inertia of the particle in the running state. In the particular case with no damping and T=0, I_r is zero. Since escape current is larger than the retrapping current, the IV of the Josephson junction is hysteretic. At any given current between zero and I_c, the Josephson junction can be either in the zero voltage state($d\phi/dt = 0$) or the non-zero voltage state ($d\phi/dt > 0$). If the bias current is slowly ramped up to a value greater than I_c and then ramped down while plotting the voltage, the form of the IV is as shown in Figure 2.6.

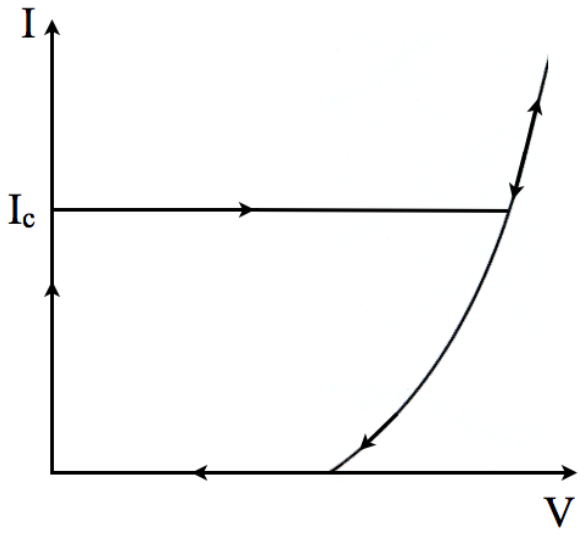

Figure 2.6: Hysteretic current-voltage characteristics for a Josephson junction with negligible damping at T=0.

2.2.3.2 Underdamped Junction at $T > 0$

In an underdamped junction (with $\beta_c \gg 1$) at $T > 0$, the particle will undergo thermal fluctuation while localised in one of the local minima. Its average position is given by $\phi = \sin^{-1}(I/I_c)$. The amplitude of thermal fluctuations increases with temperature. Thermal fluctuations cause the particle to escape from the minimum at a bias current less than the critical current I_c. The average time, τ_{TA}, taken for the particle to escape through this thermal activation is given by

$$\tau_{TA}^{-1} = a_t \frac{\omega_p}{2\pi} exp\left(-\frac{\Delta U}{k_B T}\right) \tag{2.18}$$

where $\omega_p = \omega_{p0}((1 - I/I_c)^2)^{1/4}$ is the attempt frequency and a_t is a pre-factor whose value is given by Ota *et al.* [2009a]

$$a_t = 4/\left[\sqrt{1 + (Qk_B T/1.8\Delta U)} + 1\right]^2 \tag{2.19}$$

The current at which the switch from zero voltage state to resistive state happens is termed the switching current I_{sw}. Thermally activated escape is a statistical process and hence the switching does not occur at a fixed value every time the measurement is repeated. If the bias current is slowly ramped up to a value I_{sw} and then ramped down while plotting the voltage, the form of the IV is shown in Figure 2.7.

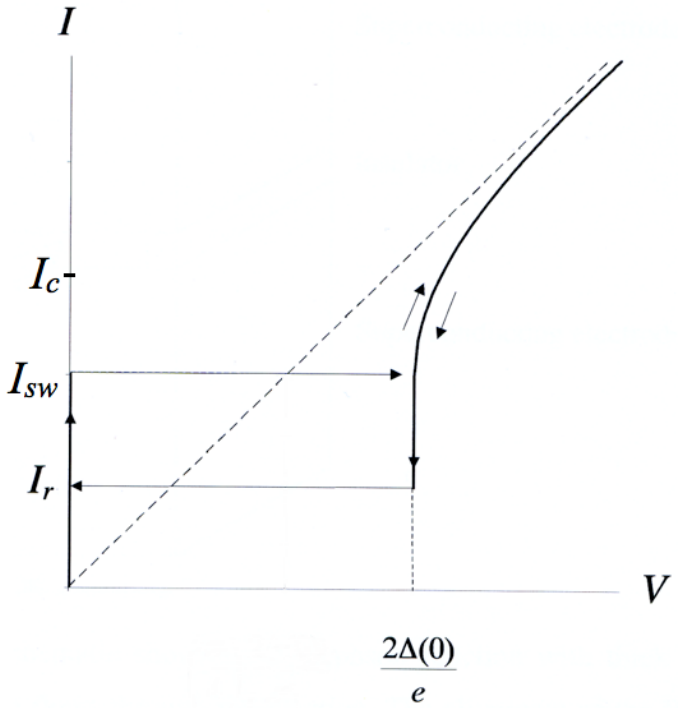

Figure 2.7: Hysteretic current-voltage characteristics for an underdamped Josephson junction at $T > 0$.

2.2.3.3 Appreciably damped Junction at $T > 0$

In an underdamped junction the particle keeps on rolling down the washboard due to its inertia, once it has escaped from the local minimum as explained previously. However, if the junction is highly damped (i.e. in the presence of a viscous fluid in the washboard analogy), the particle does not enter the running state after escape from local minimum. The particle is instead trapped in the next minimum. After some time the particle escapes again (after average escape time τ_{TA}) and gets re-trapped. This repeated escape and re-trapping is termed phase diffusion. This behaviour is markedly different from the underdamped case where the particle enters the running state after escaping. The theoretical voltage in this case is still given by Equation 2.4; however the experimentally measured valued is proportional to the average number of escapes per second. A detailed description of overdamped junctions is given in Ambegaokar & Halperin [1969]. They have mathematically modelled the junctions for small values of β_c.

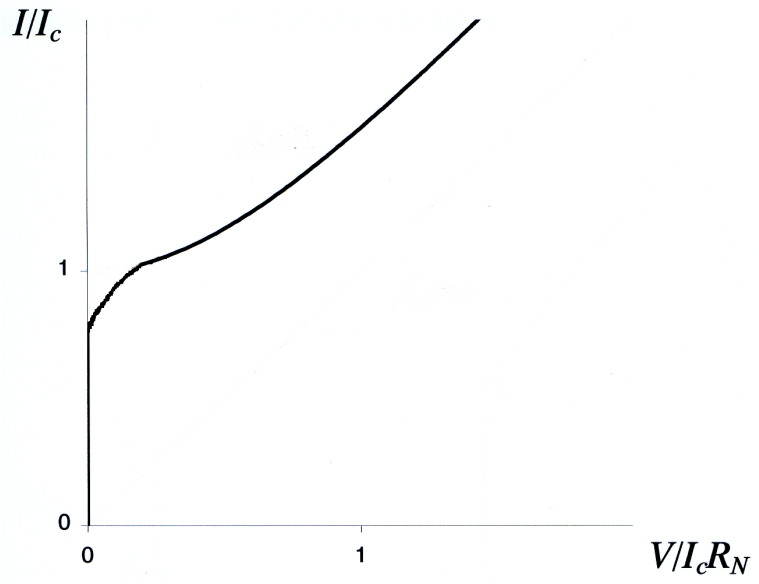

Figure 2.8: Normalised current-voltage characteristics for a Josephson junction with appreciable damping.

The two major effects of appreciable damping on the IV characteristics are

(i) suppression of hysteresis and (ii) phase diffusion. Phase diffusion results in a voltage on the supercurrent branch. Appreciable damping does not affect the escape rate to a great extent as it does the re-trapping rate. In phase diffusion the particle escape rate as given by Mannik *et al.* [2005]

$$\Gamma_{PD} = \Gamma_{TA}(1 - P_{RT})\frac{ln(1 - P_{RT})^{-1}}{P_{RT}} \tag{2.20}$$

where P_{RT} is the probability of the particle to be trapped in the next minimum once it has escaped from a local minimum. The re-trapping rate for the particle as given by Benjacob *et al.* [1982]

$$\Gamma_R = \frac{I - I_r}{I_c}\omega_p\sqrt{\frac{E_J}{2\pi kT}}exp\left(-\frac{E_J Q^2(I - I_r)^2}{2kTI_c^2}\right) \tag{2.21}$$

2.2.4 Switching Current Distribution

Switching of the Josephson junction from zero voltage to a voltage is a stochastic process. By repeatedly measuring the switching current of the Josephson junction a histogram $P(I)$ can be built, whose width and shape can be used to infer the dynamics of the Josephson junction. The shape and width of the histogram is affected by $\Gamma_{TA}, \Gamma_R, \Gamma_{PD}$ and damping in the system. Fulton & Dunkleberger [1974] did a detailed theoretical and experimental analysis of switching from zero voltage to the voltage state using the RCSJ model. They developed a relationship to link the experimentally measured $P(I)$ with the life time (the inverse of the escape rate of the particle in the washboard model) of the zero voltage state. Their equation was given as

$$\Gamma(I) = \frac{1}{\Delta I}\frac{dI}{dt}ln\frac{\sum_{i\geq I} P(i)}{\sum_{i\geq I+\Delta I} P(i)} \tag{2.22}$$

where ΔI is a small current interval, the probability of a switch between I and $I + \Delta I$ is given by $P(I)\Delta I$ and dI/dt is the bias current ramp rate. SCD will be discussed in detail in a subsequent section in this chapter.

2.2.5 RF Effects in Josephson Junctions

2.2.5.1 A.C. Josephson Effect

If a dc voltage is applied across a Josephson junction, then by integrating Equation 2.4 we find $\phi = \phi_o + (2e/\hbar)Vt$. By substituting this value in the Equation 2.3 the current is $I = I_c \sin(\omega_j t + \phi_0)$ where ϕ_0 is a constant of integration. This gives us a supercurrent which oscillates at a voltage-dependent frequency $f_J = \frac{\omega_J}{2\pi} = \frac{2eV}{2\pi\hbar}$. f_J is known as the Josephson frequency and is directly proportional to the applied dc voltage. This effect is called the **ac Josephson effect**. This effect was experimentally verified by Yanson [1965] and Giaever [1965]. The coefficient f_J/V is 483.6×10^{12} Hz/V.

2.2.5.2 Inverse A.C. Josephson Effect

If a Josephson junction is driven by both a dc voltage (which will make it oscillate at ω_j) and an ac voltage at frequency of ω_s, then from Equations 2.3 and 2.4 the current through the junction is given by

$$I_s(t) = I_c \sin\left[\int_0^t \frac{2e}{\hbar} v(t)d(t) + \phi_0\right] \tag{2.23}$$

where $v(t) = V + V_s \cos(\omega_s t)$ is the instantaneous voltage. Integrating Equation 2.23 we get

$$I_s(t) = I_c \sin\left[\frac{2eV}{\hbar}t + \frac{2eV_s}{\hbar\omega_s}\sin(\omega_s t) + \phi_0\right] \tag{2.24}$$

where ϕ_0 is a constant of integration. Using trigonometric identities and Bessel functions the above equation is rewritten as

$$I_s(t) = I_c \sin \sum_{n=-\infty}^{\infty} (-1)^n J_n \left(\frac{2eV_s}{\hbar\omega_s} \right) \sin\left[(\omega_j - n\omega_s)t + \phi_0\right] \tag{2.25}$$

At $\omega_j = n\omega_s$ there are current steps (Shapiro steps) at constant voltage in the junction current-voltage characteristics as shown in Figure 2.9. As these steps are evenly spaced in frequency, they are also evenly spaced in voltage, occurring at $V = n\hbar\omega_s/2e$. Similarly an ac current causes Shapiro steps in the IV characteristics as shown in Figure 2.10. Theoretical and experimental values of the step height for first step (n=0) are shown in Figure 2.11.

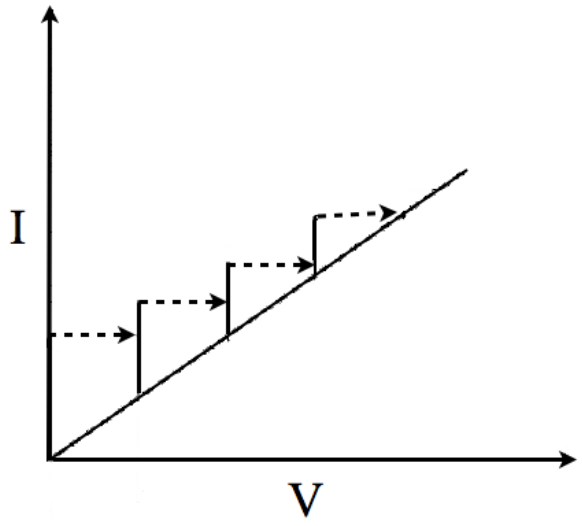

Figure 2.9: IV Characteristics of voltage biased Josephson junction with Shapiro spikes. Figure from Van Duzer & Turner [1998].

2.2.6 Magnetic Field Effect in Josephson Junctions

Until now it has been assumed that no magnetic fields are applied to the Josephson junction, and the self-field (generated by the Josephson current in the junction) is negligible. If the self-field is negligible then any applied magnetic field will

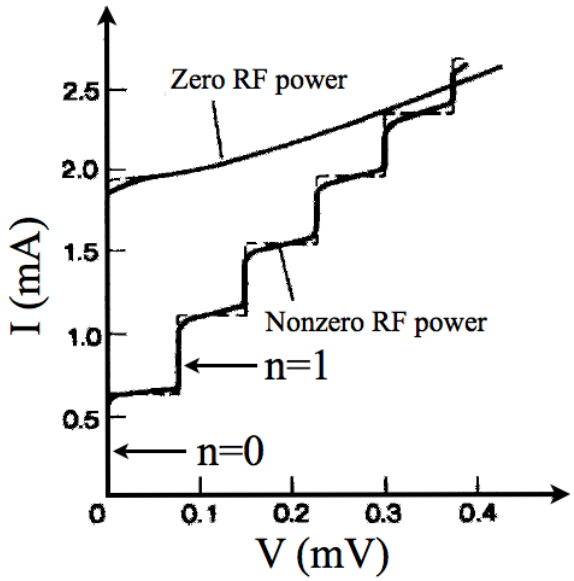

Figure 2.10: IV Characteristics of a current biased Josephson Junction with Shapiro steps. Figure from Taur *et al.* [1974].

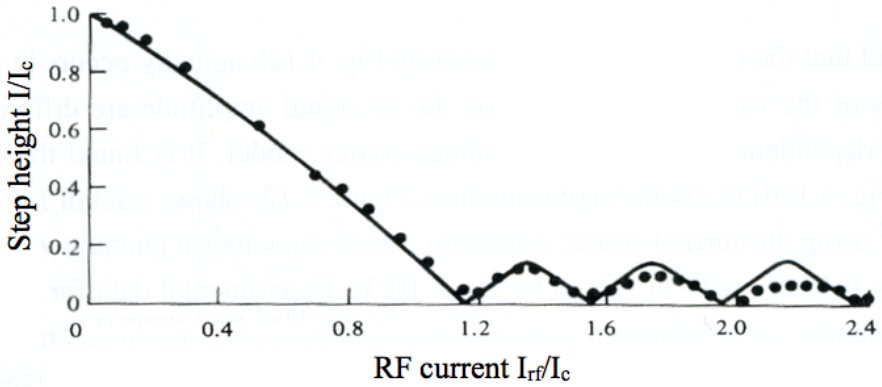

Figure 2.11: Experimentally determined dependence of the zeroth step height ($n = 0$) for the data in Figure 2.10 in comparison with theoretical calculations. Figure from Taur *et al.* [1974].

completely penetrate the junction. On the other hand, if the Josephson currents in the junction are large, the self-field will not be negligible and an applied magnetic field will only penetrate the sides of the junction to a certain width termed the Josephson penetration depth λ_J. For a conventional Josephson junction with superconducting electrodes much thicker than the London penetration depth λ_L, the Josephson penetration depth is given by $[\Phi_0/2\pi\mu_0 J_c(2\lambda_L + t)]$ for a barrier thickness t and critical current density J_c. For an intrinsic Josephson junction with superconducting electrodes (single cuprate double plane), the thickness is smaller than the London penetration depth λ_L and the Josephson penetration depth is given by $\lambda_J = \gamma t$ where $\gamma = \lambda_c/\lambda_{ab}$ is the anisotropy and t is the separation of adjacent copper oxide double planes [Irie *et al.*, 2000; Kleiner *et al.*, 1994].

In my cuprate samples the separation (t) of adjacent copper oxide double planes is 1.3 nm and the typical value of γ is 1000 [Kleiner *et al.*, 1992, 1994]. This gives a value for λ_J of approximately 1 μm [Mros *et al.*, 1998; Warburton *et al.*, 2004]. A Josephson junction which has one or more dimensions longer than λ_J is called a long Josephson junction. A small Josephson junction has dimensions smaller than λ_J. All junctions presented in this research are small Josephson junctions.

To understand the effect of magnetic field on Josephson junction consider the junction shown in Figure 2.12 with an applied magnetic field along the z-direction. The total in plane applied magnetic flux Φ changes the phase difference ϕ, across the Josephson junction. The phase difference across the junction is given by

$$\phi = \phi_1 - \phi_2 + 2e/\hbar \int \mathbf{A}.d\mathbf{l} \tag{2.26}$$

where ϕ_1 and ϕ_2 are the phases in zero field and $\mathbf{A}$ is the magnetic vector po-

tential. The applied field makes the phase ϕ spatially varying in the x-direction. To incorporate the effect of this varying phase difference, Equation 2.3 can be rewritten as $J_s(x) = J_c \sin\phi(x)$ where $J_s(x)$ is the supercurrent density per unit width in the x direction and J_c is the critical current density.

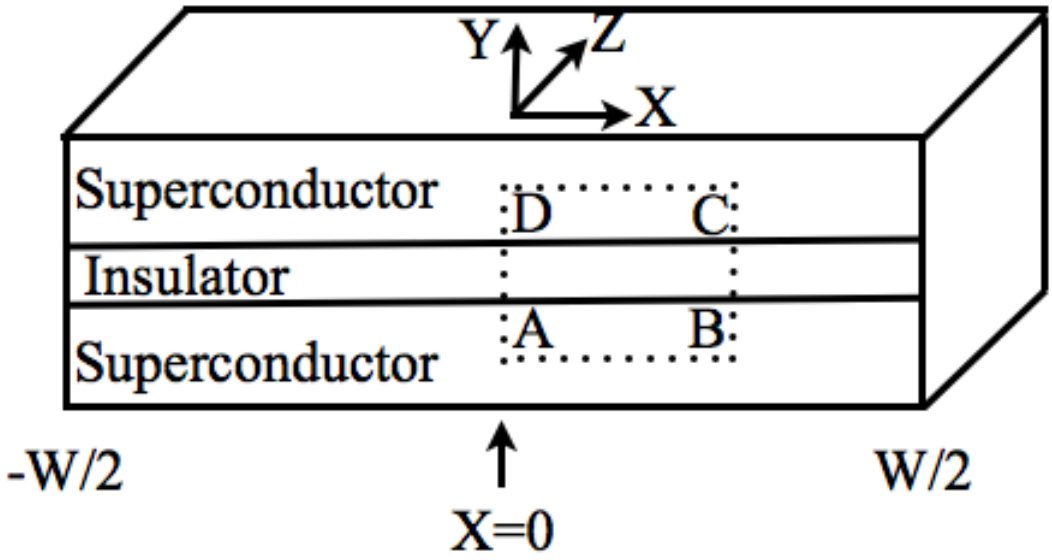

Figure 2.12: Application of a magnetic field along the z-direction to a Josephson junction. Figure from Poole [2007].

Here $\phi(x)$ can be found by integrating along the dotted path ABCD in Figure 2.12 and is given by

$$\phi(x) - \phi(0) = 2\pi\Phi(x)/\Phi_0 \tag{2.27}$$

where $\Phi(x) = \Phi_x/W$ is the applied magnetic flux in the junction between 0 and x; and Φ_0 is the flux quantum. The Josephson current density can now be rewritten as

$$J_s(x) = J_c \sin\left(\phi(0) + 2\pi\frac{\Phi(x)}{\Phi_0}\right) \tag{2.28}$$

and

$$I_s = \frac{J_c w \Phi_0}{\pi\Phi}\sin(\phi(0))\sin(\frac{\pi\Phi}{\Phi_0}) \tag{2.29}$$

The maximum supercurrent flows through the junction when $\phi(0) = \pm\pi/2$. The magnetic field dependence of the the critical current is therefore given by

$$I_c(\Phi) = I_c(0)\frac{\sin\frac{\pi\Phi}{\Phi_0}}{\frac{\pi\Phi}{\Phi_0}} \tag{2.30}$$

where $I_c(0) = J_c w$ is the critical current in zero field. The magnetic field dependence of the critical current is shown graphically in Figure 2.13. This pattern is similar to a two slit diffraction pattern commonly observed in optics and is called the Fraunhofer pattern. The magnetic field B_0 at the first minimum of the Fraunhofer pattern is given by

$$B_0 = \frac{\Phi_0}{w(d + 2\lambda)} \tag{2.31}$$

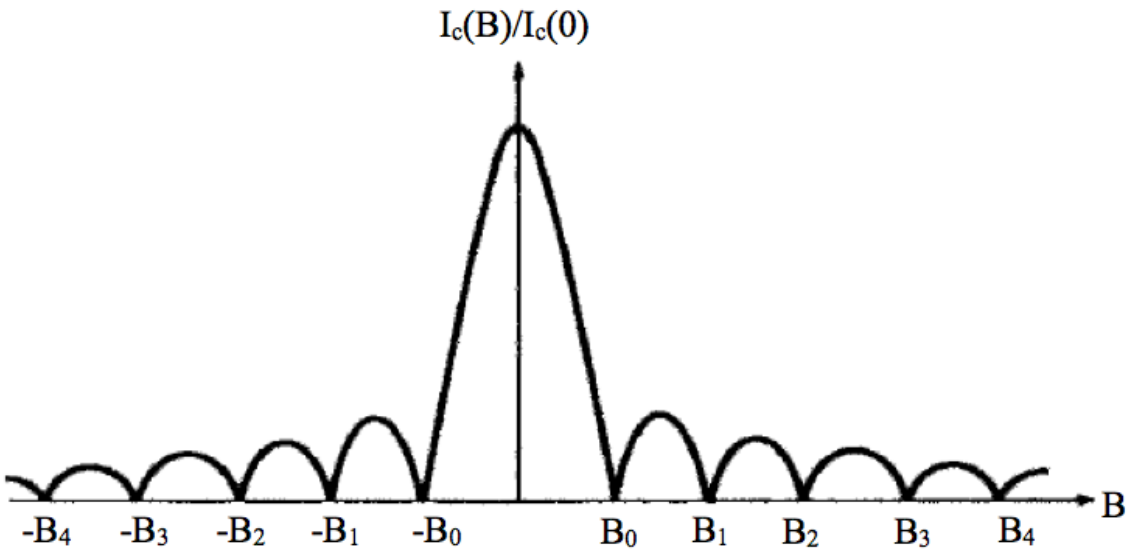

Figure 2.13: Josephson Fraunhofer diffraction pattern showing the maximum normalised zero-voltage current.

2.3 High and Low Temperature Superconductors

Since Onnes's initial observation, many superconducting materials have been found. Along many metallic elements, metallic alloys with transition temperatures up to 23.2 K were found by 1973. In 1986, Bednorz and Muller showed that copper oxides could have a transition temperature as high as 35 K [Bednorz & Muller, 1986]. In the following years many more compounds were discovered with even higher T_c. Mercury based cuprates have the highest T_c of 134 K at present. The metallic superconductors are usually called low temperate superconductors (LTS) [Van Duzer & Turner, 1998]. Collectively the materials with transition temperature above 23.2 K are referred to as high temperature superconductors (HTS).

In LTS, six out of the twenty five elemental superconductors have a transition temperature above the boiling point of liquid helium. Niobium (Nb), one of these six, with a critical temperature of 9.2 K is favoured for junction fabrication due to its higher chemical and mechanical stability. Various Nb alloys are also used for junction fabrication. The superconducting energy gap Δ is uniform in all directions in LTS.

Three major HTS materials used to fabricate JJs are yttrium barium copper oxide (YBCO), bismuth strontium calcium copper oxide (BSCCO) and thallium barium calcium copper oxide (TBCCO). The majority of the work in this research was carried out with $Tl_2Ba_2CaCu_2O_8$ (Tl2212) thin films. Some work was also carried out using Bi2212 single crystals. The crystal structure of Tl2212 is shown in Figure 2.14. The structure has a layered series combination of superconducting copper and insulating planes made of Tl. The copper oxide layer is about 3 Å thick with an interlayer spacing of 12 Å [Duan *et al.*, 1991]. It is established that the superconductivity in HTS is based on Cooper pairs [Gough, 1987]. Unlike

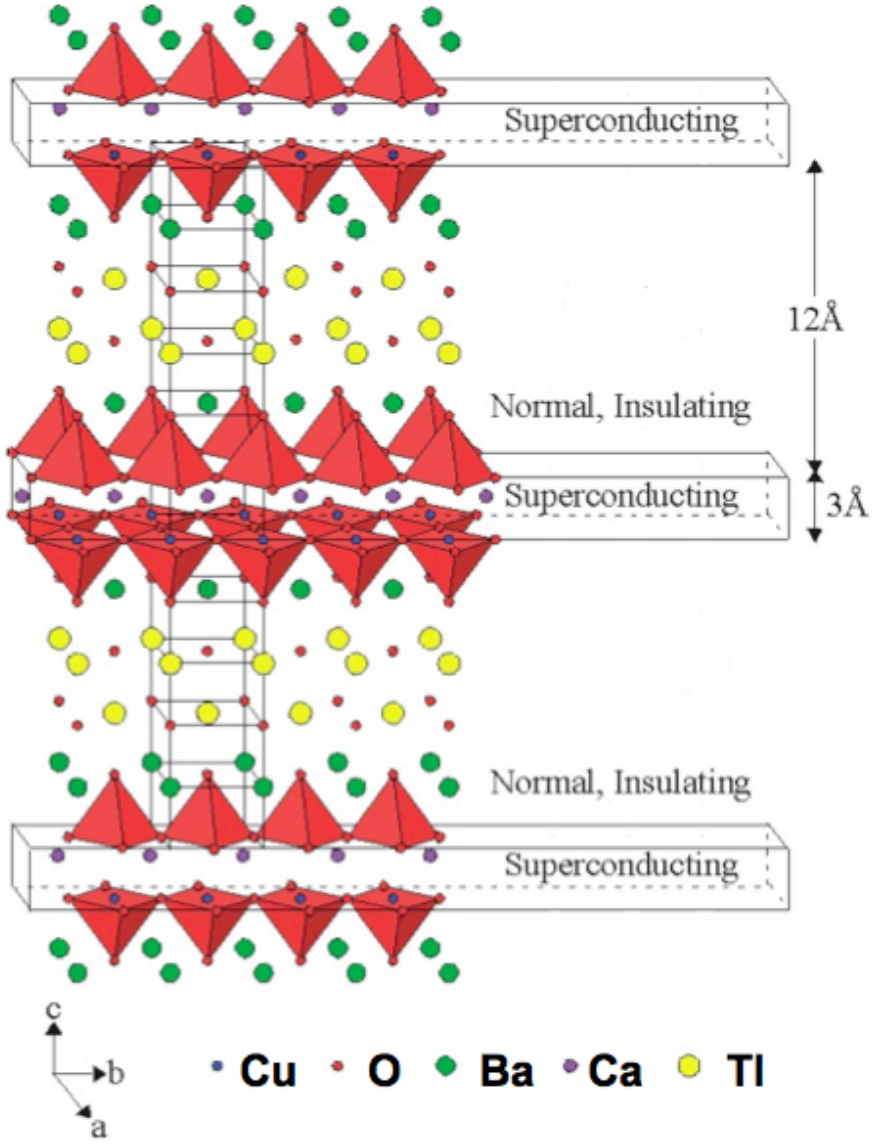

Figure 2.14: Crystal structure of Tl-2212. The distance between the two copper layers of a single superconducting element is 3 Å and between the adjacent copper oxide layers (on either side of the insulating material) is 12 Å.

LTS for which the microscopic BCS theory exists, there is no single agreed upon microscopic theory for HTS.

HTSs do not have a uniform superconducting energy gap in all directions and probably possess a d-wave symmetry. They have large anisotropy and are more prone to thermal fluctuations due to smaller energy gap in certain directions. The coherence length ξ in HTS is very small compared to LTS. In cuprates ξ is on the order of 2 nm in the ab-plane and 0.5 nm in the c-direction [Waldram, 1996]. The short coherence length, interface problems, sensitivity to oxygen stoichiometry and unwanted grain boundaries all tend to degrade the reliability and reproducibility of HTS Josephson junctions. HTS samples also degrade over time.

2.4 Josephson Junction Types

The basic concept of how a Josephson junction works is same in both LTS and HTS. However the way the junction is realised is different. A review of low and high temperature Josephson junctions was given by Darula *et al.* [1999] and technologies for the HTS Josephson junctions were reviewed by Gross *et al.* [1997] and Delin & Kleinsasser [1996].

2.4.1 LTS Josephson Junctions

LTS junction fabrication technology is rather mature by comparison with HTS. LTS JJs use a normal metal, insulator or semiconductor as the barrier layer to separate the Nb films. Large arrays of LTS JJs have been fabricated using multistage fabrication techniques and used for voltage calibration applications [Schulze *et al.*, 2000]. Superconducting Quantum Interference devices (SQUID) have been used to detect extremely weak magnetic fields [Clarke, 1989]. Rapid single flux quantum (RSFQ) circuits using LTS materials operating at 100 GHz have been manufactured [Kleinsasser, 2001]. LTS JJs have been shown to act as coherent far-infrared radiation sources [Barbara *et al.*, 1999]. The basic reason for the success of LTS JJs is their longer coherence length. This means that LTS JJs are insensitive to small (i.e. smaller than the coherence length) defects at the interface between the superconducting films and the barrier layer.

2.4.2 HTS Josephson Junctions

2.4.2.1 Extrinsic Josephson junctions

In extrinsic Josephson junctions the interface between the two superconductors (i.e the weak link) is artificially fabricated. Various fabrication techniques are available to manufacture the extrinsic Josephson junctions like grain-boundary junctions, bi-crystalline junctions, step-edge junctions, gap-edge junctions, ramp

junctions, weakened structures and tri-layer junctions [Barone & Pagano, 1994]. These junctions are not reviewed here as no extrinsic junctions were used in this research.

2.4.2.2 Intrinsic Junctions

In Figure 2.14, insulating material between the copper oxide layers acts as a weak link. Adjacent copper oxide layers are weakly coupled and the whole structure (copper oxide layer-insulating layer-copper oxide layer) acts as a series of Josephson junctions. Hence, intrinsic Josephson junctions (IJJs) do not have any artificially-fabricated interfaces. Junctions are formed naturally between the superconducting a-b planes of the crystal, along the c-direction. Figure 2.15 shows the amplitude of the order parameter along c direction for the Tl2212 crystal structure shown in Figure 2.14.

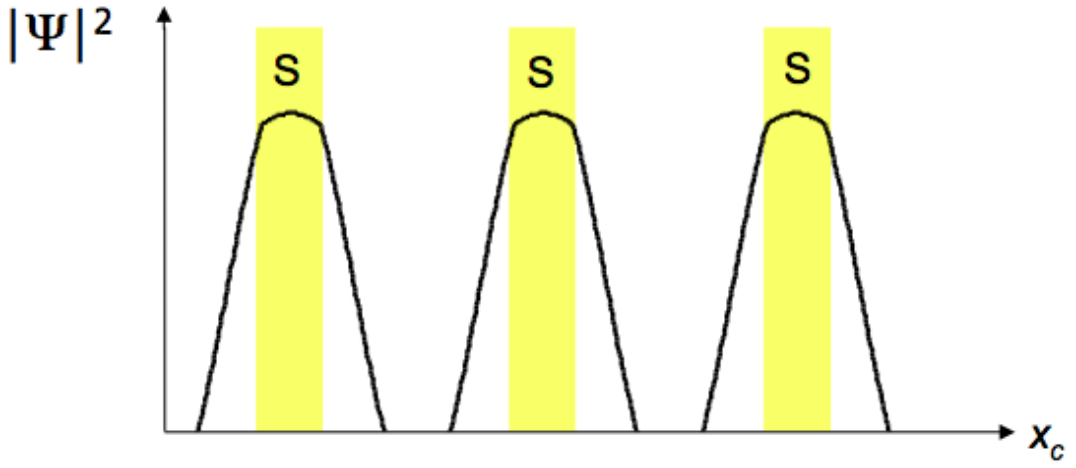

Figure 2.15: Amplitude of the order parameter along c direction for the Tl2212 crystal structure shown in Figure 2.14.

Intrinsic Josephson junctions are also based on the Josephson effect i.e. the tunnelling of Cooper pairs between adjacent CuO_2 planes. The presence of Josephson junctions can be verified by

- Hysteresis in the IV characteristics

- Temperature dependence of switching current
- Magnetic field dependence of the switching current
- Shapiro steps

$Ba_2Sr_2CaCu_2O_8$ (Bi2212) was the first material in which IJJs were discovered by Kleiner *et al.* [1992]. They performed all the above tests to establish the Josephson nature of coupling between the BSCCO layers. Their main results are shown in Figure 2.16.

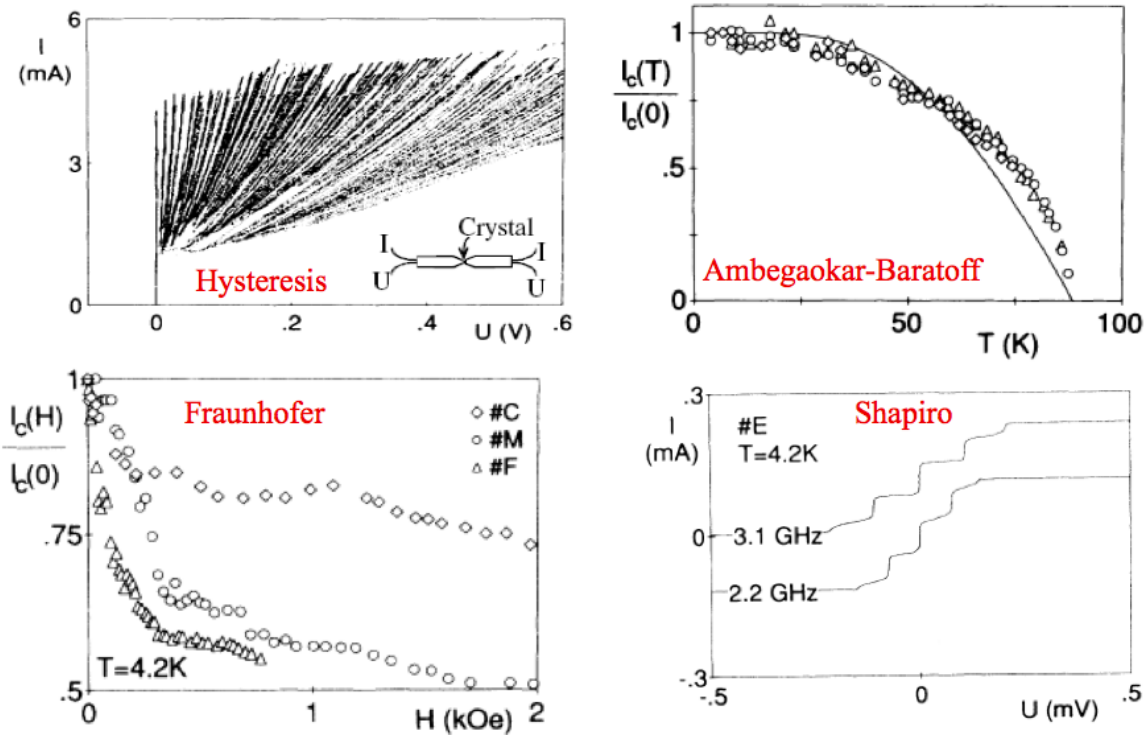

Figure 2.16: Current voltage characteristics, temperature and magnetic field dependence of the switching current and Shapiro steps measured in IJJs by Kleiner *et al.* [1992].

They measured the IV characteristics and found a concave curvature (graph labelled 'Hysteresis') in the resistive state. The curvature of the branches is explained by the V-shaped quasiparticle conductance observed in c-axis tunnelling experiments [Mandrus *et al.*, 1991]. The IVs are very similar to the IV charac-

teristics of arrays of small underdamped Josephson junctions [McCumber, 1968]. The switching current of the Josephson junctions also followed the Ambegaokar-Baratoff relation. They measured the field dependence of the switching current and extracted the junction width w, which was in agreement with the geometric scale of the junction. This enabled them to prove conclusively that Josephson junctions were formed by two adjacent CuO_2 double layers. They observed Shapiro steps in the IV at two different frequencies and found several IJJs to be phase locked. All these results confirmed the presence of Josephson junctions in BSCCO.

Coupling between the different layers of BSCCO has also been investigated by Krasnov *et al.* [2005a]. They studied this by measuring thermal fluctuations in intrinsic Josephson junctions. The switching current statistics of the IJJ were well described, without fitting parameters, in terms of thermal activation from the tilted washboard potential with a sinusoidal current-phase relation. This was used as direct evidence of the dc-intrinsic Josephson effect. The fluctuation-free I_{c0}, extracted from the analysis of switching current histograms, exhibited a T dependence typical for SIS tunnel junctions, also consistent with the tunnelling nature of interlayer transport in Bi-2212.

The magnetic field-dependence of the switching current has been extensively studied by Gaifullin *et al.* [2003]; Latyshev *et al.* [1997, 2004]. Their measurements confirm the Fraunhofer-like field dependence of the switching current as shown Figure 2.17. The fact that minima are far from the magnetic field axis is attributed to the formation of Josephson vortices. The amplitude of the oscillations decreases with increasing H.

They also report flux-flow in their field dependent measurements in IJJs. The applied field introduces Josephson vortices in the junction. In high fields the regions of vortices overlap strongly because the inter vortex distance a along the ab-plane becomes smaller than λ_j. All the interlayer spacings become filled

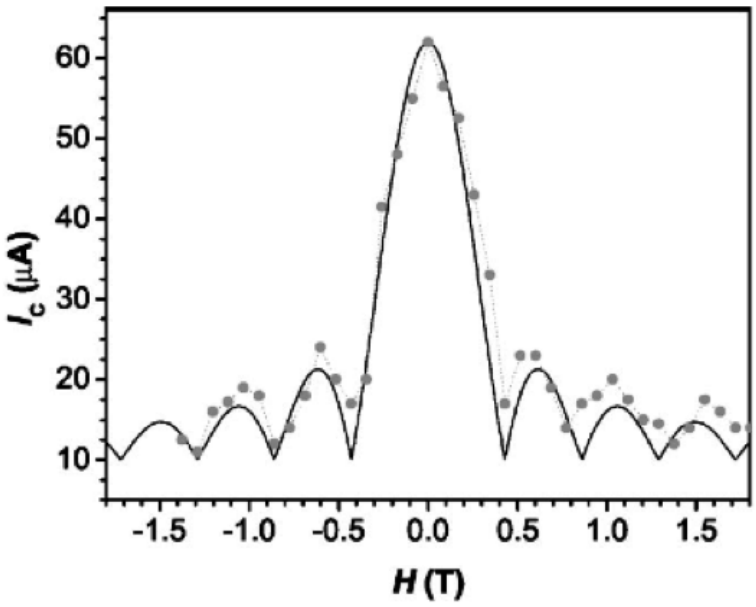

Figure 2.17: Dependence of the critical current I_c of Bi2212 IJJ on the parallel magnetic field H at T=4.2 K. The solid lines correspond to the function $I_c = I_{c0}\,|\sin(x)/x| + I_{c1}$ with $x = \pi H w l/\Phi_0$, where w is the width of the junction and l is the thickness of the junction. Figure from Latyshev *et al.* [2004].

by vortices forming a triangular lattice. This lattice is rigid and moves as a whole [Bulaevskii *et al.*, 1996]. A resonance occurs when the velocity of the fluxons becomes equal to the velocity of the electromagnetic field propagation in the junction. In flux flow, fluxons are created at one boundary of the junction and annihilate at the other boundary [Latyshev *et al.*, 1997]. The movement of fluxons creates a voltage (V_0) whose field dependence is shown in Figure 2.18. Initial Shapiro steps reported in IJJs were explained by the phase locking of several IJJ junctions. Wang *et al.* [2000a] used the gold shunt and reduced the normal resistance (R_n) of the junction stack to 0.5 Ω and observed the individual Shapiro steps shown in Figure 2.19.

All the above mentioned experiments establish the fact that coupling between the layers of cuprates is Josephson like. The majority of the work on IJJs has been done using BSCCO. Josephson junctions have however been found in a number of HTS materials including TBCCO and YBCO [Rapp *et al.*, 1996; Warburton

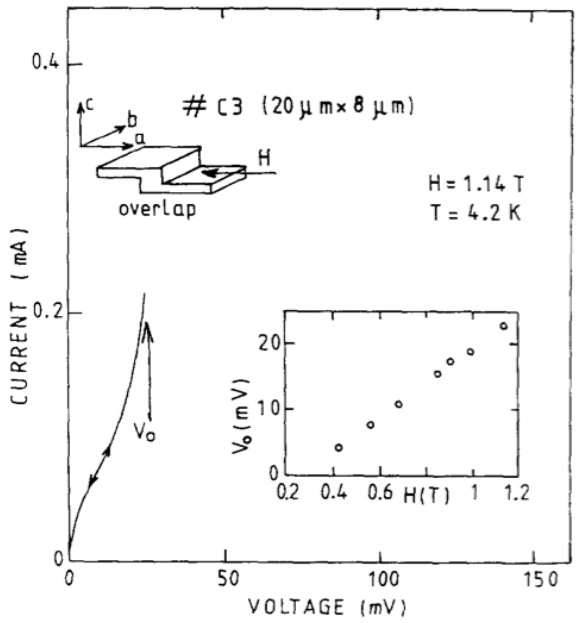

Figure 2.18: Large scale I-V characteristic of BSCCO overlap structure in magnetic field H parallel to ab plane at 4.2 K. Inset shows a dependence of the maximum step voltage of the flux-flow, V_o, on the magnetic field. Figure from Latyshev *et al.* [1997].

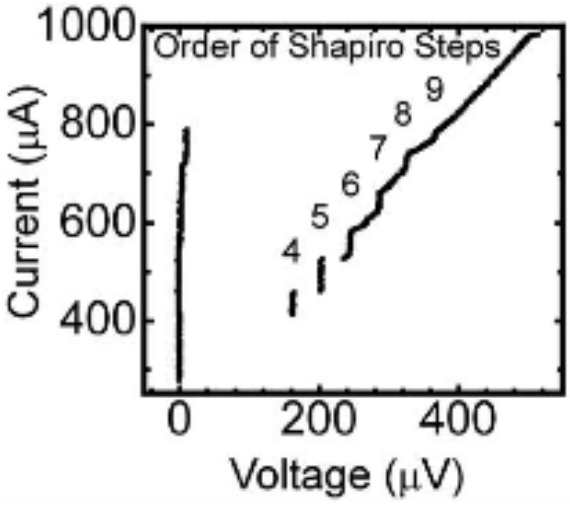

Figure 2.19: Typical current voltage (IV) characteristics with microwave irradiation at 20 GHz, of a resistively shunted intrinsic Josephson junction. Figure from Wang *et al.* [2000a].

et al., 2003a]. A topical review of the intrinsic Josephson junction was given by Yurgens [Yurgens, 2000].

Tl2212 has a T_c of 115 K and its crystal structure is shown in Figure 2.14. Tl2212 has been studied extensively [Ozkan *et al.*, 1999; Subramanian, 1988; Wang & Ma, 2005; Warburton, 2007]. A number of experimental methods exist to fabricate IJJs, including lithography, ion implantation and artificial multilayer on single crystals, vicinal thin films and thin films. Most common methods to fabricate the IJJs using single crystals and thin film include the bridge structure [Kim *et al.*, 1999] and the mesa structure [Wang *et al.*, 2001]. HTS IJJs have the advantage of a better integrity of insulating layers and high critical temperatures.

2.5 Heating in IJJ IVs

The superconducting energy gap Δ can be extracted from the dc IVs of LTS JJs from voltage at $dI/dV \rightarrow \infty$. A similar feature ($dI/dV \rightarrow \infty$) appears in the dc IVs of IJJs. This value of voltage ($dI/dV \rightarrow \infty$) in IJJs has been used to calculate the apparent superconducting energy gap. However, it has been argued that the gap value 2Δ deduced from the dc IVs and located at $dI/dV \rightarrow \infty$ of an IJJ stack suffers from self-heating [Fenton *et al.*, 2002; Gough *et al.*, 2000; Thomas *et al.*, 2000]. The mesa temperature rises above the bath temperature due to the power dissipation. This increase in temperature reduces ρ_c and hence the voltage across the junction begins to fall. More current flows through this reduced resistance and raises the temperature even higher resulting in a further voltage drop. At higher bias currents the self heating can even cause back bending.

Heating in the IJJ stack is proportional to the number of junctions in the voltage state. Thomas *et al.* [2000] measured mesa temperatures over a range of bath temperatures and bias currents and found significant heating at all bath temperatures. By using short pulse measurements Gough *et al.* [2000] established that the major source of non-linearity and back bending was heating. Time resolution of better than 1 μsec is required to rule out the effects of self-heating. It was shown that I-V characteristics and the voltage at which dI/dV becomes infinite are strongly dependent on the time after the application of a pulsed current, consistent with heating. A 10% drop in voltage value was observed 500 ns after the application of the pulse [Fenton *et al.*, 2002].

Recently Kurter *et al.* [2008] have established that back bending in Bi2212 mesas has its origins in the particular temperature dependence of $R_{qp}(T)$. The strong time dependence of the shape of the characteristics makes it clear that the infinite slope and onset of the back bending feature is not an intrinsic feature associated with the gap voltage. Hence using the voltage at which the dynamic

conductance becomes infinite [Yurgens *et al.*, 1996] is therefore not a very useful method to provide a meaningful measurement of the energy gap. This change in Δ value with temperature explains why there is no unanimously agreed value of Δ for Tl2212.

2.6 Previous Results - Switching Current Measurements

2.6.1 Temperature Dependent Switching Current Distribution Measurements

The dynamical behaviour of Josephson junctions can be divided in three distinct regions depending on the operating temperature. For $E_J \gg k_B T$ a single escape event, either due to thermal activation or macroscopic quantum tunnelling, will cause the junction to switch rapidly from the zero voltage state to voltage state (running state in washboard model). For $T \gg T_{cr}$ (T_{cr} defined later) the width σ of SCD, $P(I)$, which is a measure of the strength of thermal fluctuations, is given by $\sigma \propto T^{2/3}$ and this region is termed as underdamped thermal activation distribution (UTAD). For $T \ll T_{cr}$ the width (σ) is independent of T and this region is called macroscopic quantum tunnelling (MQT). T_{cr} is the temperature below which the behaviour of the junction changes from UTAD to MQT and is given by

$$T_{cr} \approx \frac{\hbar \omega_p}{2\pi k_B} \tag{2.32}$$

for a junction with plasma frequency f_p of 500 GHz, T_{cr} is 3.8 K.

In presence of higher damping, the particle has a significant probability of being retrapped in a subsequent well after the initial escape. Thus, escaping from the initial well does not necessarily cause the junction to switch to the running state. The state in which repeated escape and retrapping occurs is called the phase diffusion (PD) state. The temperature at which behaviour changes from UTAD to PD is termed as T^*. All three regions are shown in Figure 2.20 and briefly discussed below.

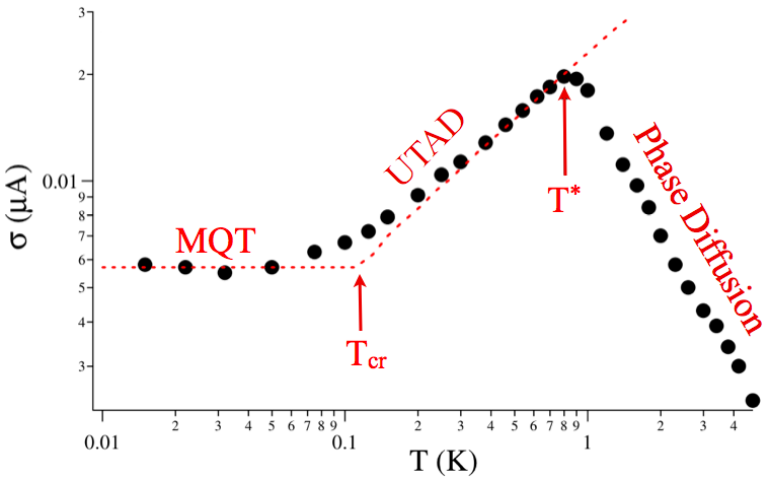

Figure 2.20: Temperature dependence of the width of the switching current distribution (symbols) and the theory of UTAD and MQT theory (lines). Three distinct regions of dynamic behaviour of Josephson junction are labelled as macroscopic quantum tunnelling (MQT), underdamped thermal activation (UTAD) and phase diffusion (PD). Figure from Li *et al.* [2007].

2.6.1.1 Underdamped Thermal Activation

One way for the particle to escape from the energy minimum is by thermal activation. Thermal fluctuations provide the energy to particle to overcome the barrier and enter the running state, provided the damping in the system is low. Escape rate in UTAD is given by Kramers [1940] as

$$\Gamma_E(I) = a_t \frac{\omega_p}{2\pi} exp\left(-\frac{\Delta U}{k_B T}\right) \tag{2.33}$$

where a_t is a pre-factor ($0 < a_t < 1$) which is normally taken as unity.

Thermal activation has been studied for moderate damping by Castellano *et al.* [1996]; Fulton & Dunkleberger [1974]; Ruggiero *et al.* [1998] and low damping by Martinis *et al.* [1987]; Ruggiero *et al.* [1998]. Fulton & Dunkleberger [1974] measured SCD on Sn-Sn tunnel junctions and determined the life time of the zero voltage state as a function of bias current. They established the relation between the escape rate of the particle and the experimentally measured SCDs mentioned

in Equation 2.22.

Castellano *et al.* [1996] measured the escape temperature in underdamped Nb tri-layer junctions with different fabrication processes and having different characteristics. It was found that dissipation properties of the Josephson junctions were strongly influenced by the current density, with lower current density resulting in lower intrinsic dissipation. The relation between SCD width σ and sample temperature $T^{2/3}$ has been confirmed by Franz *et al.* [2004]; Krasnov *et al.* [2005b]; Ruggiero *et al.* [1998]'s measurements.

In summary in UTAD the width of SCD follows the theoretical $T^{2/3}$ dependence as observed by number of research groups. $d\sigma/dT$ is positive until a maximum temperature termed T^* above which $d\sigma/dT$ is negative.

2.6.1.2 Macroscopic Quantum Tunnelling

Tunnelling of the particle through the barrier at $T < T_{cr}$ is termed as MQT and escape rate of the particle is given by

$$\Gamma_{MQT}(I) = a_q \frac{\omega_p}{2\pi} exp^{(-7.2 b_q \Delta U/\hbar\omega_p)} \tag{2.34}$$

where $a_q \approx [120\pi(7.2\Delta U\omega_p)]^{1/2}$ and $b_q \approx (1 + 0.87/Q)$.

Preliminary results on MQT in single junctions were reported by Jackel *et al.* [1981]; Voss & Webb [1981]. Experimental results on LTS JJs from both groups showed MQT like behaviour. Devoret *et al.* [1985] measured MQT in a current biased junction in which they determined all the relevant parameters in-situ using classical phenomena. This enabled them to compare their experimental data with theory without any adjustable parameter. They observed MQT below 25 mK for the LTS Josephson junctions. It is important to note that, in addition to MQT, temperature-independent σ can be generated by experimental limitations such

as self-heating, extraneous noise, and inadequate measurement resolution. A detailed discussion of MQT can be found in Likharev [1986].

MQT in IJJ was first reported by Inomata *et al.* [2005]. Bauch measured MQT in YBCO at 40 mK where as Inomata measured MQT in Bi2212 at 1 K, the highest reported temperature for MQT until then. Inomata *et al.* [2005] compared the experimentally measured SCD σ and T_{esc} to theory and found a temperature independent behaviour below a certain crossover temperature T_{cr}. Their result established the fact that it is possible to measure MQT despite the quasiparticle dissipation. This is different from the LTS case where no quasiparticle exists below the superconducting energy gap.

Jin *et al.* [2006] measured the MQT in single junction switching and uniform junction switching IJJ stacks shown in Figure 2.21. They found an enhanced escape rate of MQT in uniformly switching IJJs stacks as compared to single junction switching. The crossover temperature from MQT to UTAD was also found to be higher for the uniform switching stack. The enhancement of escape rate for the uniform switching stack was approximately N^2 where N was the number of junctions in the stack. It was argued that large quantum fluctuations due to interactions among the N junctions were responsible for the enhanced escape rate and also result in a significant increase of the crossover temperature. I have investigated uniform switching and will present my results on uniform switching in thermal regime in the next chapter.

Li *et al.* [2007] measured all three regimes in a submicron IJJ in which I_c of the uppermost IJJ was 25 times smaller than the other IJJs in the stack. The identical results of their $P(I)$ measurements at several temperatures below T_{cr} with different cooling times between individual switches ensured that the T-independent behaviour of σ for $T < T_{cr}$ could not have been caused by self-heating. Their results do not shown any dependence of I_c on temperature or the presence of higher harmonic terms at low temperature as reported by Bauch *et al.*

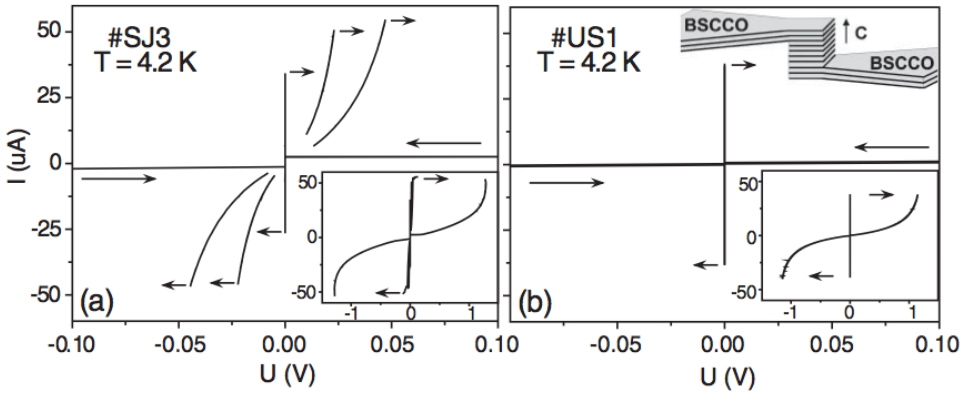

Figure 2.21: I-V characteristics: (a) One-by-one switching of three junctions in a stack, SJ3; (b) uniform switching of the whole stack, US1. The insets show the full-range I-V curves for both samples. The sample geometry is sketched in the upper right corner. Figure from Jin *et al.* [2006].

[2005].

Historically Josephson junction dynamics have mainly been studied by observing switching from supercurrent branch. The majority of SCD measurements are made from the zero voltage state to voltage state. To better understand the working of the junctions in an IJJ stack and their effect on one another, some groups have recently reported switching current distributions from quasi-particle branches [Kashiwaya *et al.*, 2008, 2009; Ota *et al.*, 2009a,b].

Kashiwaya *et al.* [2008] reported one of the first measurements of MQT from the quasiparticle branch. They compared the SCD from the supercurrent branch and the first quasiparticle branch. They reported two main results: (i) The temperature at which the SCD width saturated was found to be higher on the quasiparticle branch than on the supercurrent branch; (ii) the reversal of the switching currents of the supercurrent branch and quasiparticle branch above and below the T_{cr}. They explained the higher T_{cr} for the quasiparticle branch in terms of self heating due to one junction being in voltage state. They used the model of coupled IJJs proposed by Koyama & Tachiki [1996]; Machida & Koyama [2004]; Machida *et al.* [1999] to explain the reversal of the switching currents.

They have also reported the reversal of the mean of the switching current that is $I_{sw1} > I_{sw2}$ below T_{cr} and $I_{sw1} < I_{sw2}$ above T_{cr}. They explain the higher value of T^{cr} for first branch in terms of a self heating effect in the resistive state after the first switch. They found different temperature dependences for I_{sw1} and I_{sw2} and attribute the switching current reversal to this temperature dependence.

Recently Kashiwaya *et al.* [2009] have measured switching current distributions from quasiparticle branches by changing the output resistance of the current source as shown in Figure 2.22. They distinguish three types of switching: Single Junction Switching (SJS) where the junction with the smallest switching current switches first independent of the load line as reported in Kashiwaya *et al.* [2008]; Multiple Junction Switching (MJS) when more than one but not all the junctions switch to voltage state and the number of junctions being switched can be controlled by the load line and Uniform Switching (US) in which all junctions in the stack switch to the voltage state as reported by Jin *et al.* [2006].

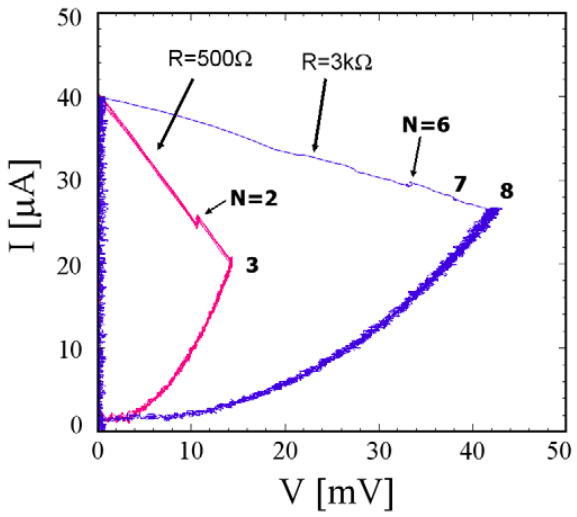

Figure 2.22: Use of load line to control the number of junctions being switched from zero voltage state to non-zero voltage state in Bi2201. By changing the resistance in series with the IJJ stack the switching from various quasiparticle branches can be measured. Figure from Kashiwaya *et al.* [2009]. N is the number of junctions being switched on.

They have found that MJS occurs more frequently in Bi2201 than Bi2212 as

the thickness of the superconducting layer in Bi2201 (0.15 nm) is less than Bi2212 (0.3 nm). This reduced thickness cannot effectively shield the other junctions from finite electrical and/or magnetic fields produced when a junction switches to the voltage state. They also show that the width of the SCD is independent of the load line by comparing the SCD from the second and third quasiparticle branches.

Ota *et al.* [2009b] measured SCD from both the supercurrent branch and the first quasiparticle branch in Bi2212 with two different device geometries. One was a small mesa with two or three IJJs and the other was a bridge structure with a stack of a few hundred IJJs. They found that T_{cr} was higher for the quasiparticle branch than the supercurrent branch. They argue that the higher saturation temperature of the SCD for the quasiparticle branch is not due to self heating as had previously been reported by Kashiwaya *et al.* [2008] as the heat dissipation environment for both device structures is different. They measured the SCD from the quasiparticle branch at various ramp rates and found the escape rate to be independent of the ramp rate as shown in Figure 2.23. They propose an effective increase in the electronic temperature due to quasiparticle injection.

The fact that the extracted fit temperature (10.2 K) is independent of the bias current for the range between 14 μA to 17 μA suggests that there is negligible self heating. My work involves the SCD measurements from the supercurrent branch and first quasiparticle branch but not at MQT temperatures. I use the experimental SCDs of these branches to explain uniform switching at temperatures higher than T_{cr}

SCDs from quasiparticle branches seem to consistently show a higher T_{cr} value than the supercurrent branch. It has been argued that the higher T_{cr} is due to the self-heating in the IJJ stack but the measurements performed on different device geometries, with different ramp rates and different cooling times between the individual switches the biasing current show that self-heating alone can not

explain the higher T_{cr} for quasiparticle branch.

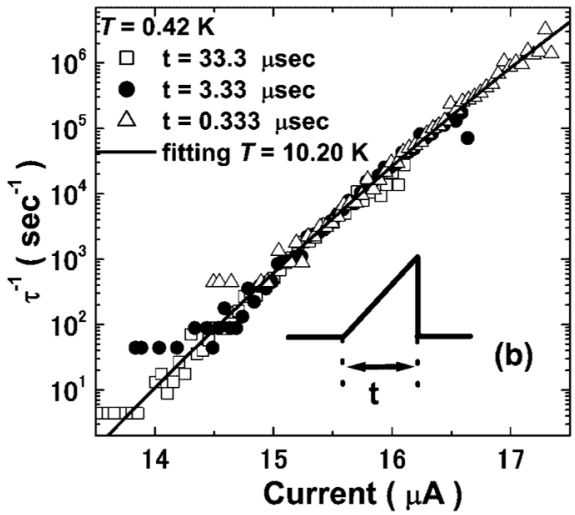

Figure 2.23: The escape rate for the quasiparticle branch measured by different ramp rates. $T_{bath} \ll T_{eff}$ has a good fit only at 10.2 K in the current range from 14 μA to 17 μA. Solid line is the calculation using the TA theory with T=10.2 K. Figure from Ota *et al.* [2009b].

2.6.1.3 Phase diffusion

The Josephson junction dynamic regime where σ decreases with an increase in temperature is termed the Phase Diffusion regime [Li *et al.*, 2007]. The crossover temperature from UTAD to PD is termed T^*. Unlike the change from MQT to UTAD there is no established analytical formula to calculate the crossover temperature denoted by T^* from UTAD to PD. The T^* from UTAD to Phase diffusion as shown in Figure 2.20 is from the experimental data only. Crossover temperature between UTAD and phase diffusion was first reported by Franz *et al.* [2004]. Crossover in temperature from UTAD to phase diffusion, T^* has been also reported by Kivioja *et al.* [2005]; Mannik *et al.* [2005].

In non-hysteretic (overdamped) junctions in the absence of noise, for bias current $I < I_c$, only the stable state for the particle in the washboard model is a potential minimum and in presence of noise, phase diffusion proceeds as a random walk among these equilibrium positions. Phase diffusion is not commonly observed in hysteretic junctions because thermally induced escape from a potential minimum usually results directly in a switch to the voltage state [Fulton & Dunkleberger, 1974; Lee, 1971]. Experimentally phase diffusion is observed as nonzero voltage at dc bias levels below the critical current. Phase diffusion in overdamped junctions is a well established phenomena [Simmonds & Parker, 1970] and follows the theoretical predictions [Ambegaokar & Halperin, 1969].

Phase diffusion in underdamped hysteretic single JJs was studied experimentally and theoretically by Kautz & Martinis [1990]; Martinis & Kautz [1989]. They described phase diffusion in junctions with hysteretic IVs and concluded that junctions have frequency dependent damping. The junctions were underdamped at low frequency ($f \ll \omega_p$) and over-damped at high frequency ($f \approx \omega_p$). Franz *et al.* [2004] explained the shift from UTAD to phase diffusion by a temperature dependent Q. This change in behaviour was said to be applicable for moderate damping. However, Krasnov *et al.* [2005b] showed that T^* will appear

even for a temperature independent Q provided the damping is moderate. He suggested that T^* can be used as a measure to estimate damping in the system by giving $T^* = T^*(Q)$.

Fenton & Warburton [2008, 2009] have performed simulations for a moderately damped junction with temperature independent $Q$and I_c. They have investigated in detail the behaviour of Josephson junctions around T^* by using Monte Carlo simulations including retrapping from the running state into the supercurrent state as given by a model due to Benjacob *et al.* [1982]. They use the escape rate Γ_E given by Equation 2.33, the retrapping rate Γ_R given by 2.21 and the normalised current ramp $\Gamma_I = \frac{1}{I}(dI/dt)$ to predict the shape of SCD. Their results are shown in Figure 2.24.

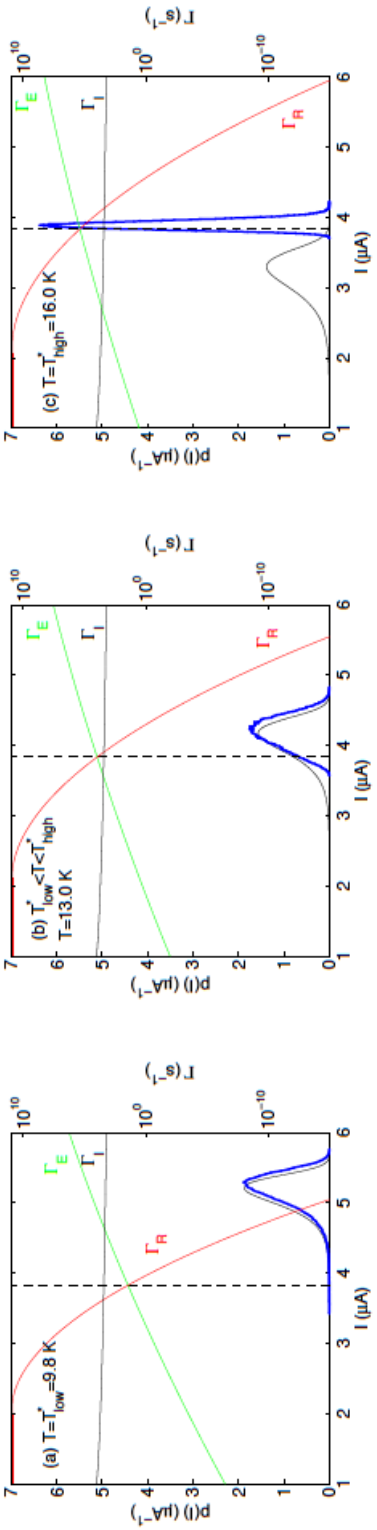

Figure 2.24: Variation in characteristic rates with current at three temperatures for Q=7, along with the switching distribution. The heavy blue points show the simulated switching distribution. The lower black curve shows the underdamped thermally activated switching distribution. The broken black line depicts the current I_{ER}. (a) T=9.8 K; I_{ER} coincides with the bottom of the thermal distribution. (b) T=13.0 K. (c) T=16.0 K; I_{ER} coincides with the top of the thermal distribution. Simulated distributions were based on 100,000 switching events. Figure from Fenton & Warburton [2008].

They identify that retrapping only has a significant effect on the dynamics when there are escapes at currents $I < I_{ER}$ (where I_{ER} is defined as the current at which $\Gamma_E = \Gamma_R$). Therefore for parameters where there are no escapes for $I < I_{ER}$ the switching distribution does not depart from the conventional underdamped thermal distribution as shown in Figure 2.24a. As the temperature increases to T^* the current I_{EI} (where I_{EI} is defined as the current at which $\Gamma_E = \Gamma_I$) decreases and multiple escape and retrapping events occur; that do not result in the count of a switch due to too small average voltage (note the missing tail in the blue points). Switching only occurs at currents $I > I_{ER}$. The shape of the SCD at this temperature starts to depart from the theoretical underdamped case as shown in Figure 2.24b. At $T > T^*$ shown in 2.24c, for normalised bias current $\Gamma_I < \Gamma_{ER}$, Γ_R is much higher than Γ_E and as soon as an escape event occurs, the particle is retrapped. Higher Γ_R does not allow any switch events to register unless normalised bias current Γ_I is above Γ_{ER}. This makes the switching distribution narrower as compared to the underdamped thermal case. In summary PD in hysteretic IJJs occurs due to higher damping at the escape frequency ($\approx \omega_p$) in the Josephson junction and its effects include a reduction of σ and a negative $d\sigma/dT$.

2.6.2 Switching Current Measurements with RF Irradiation

Measurements under RF irradiation on IJJs were performed by Irie & Oya [1995]; Irie *et al.* [1994, 1996]; Oya *et al.* [1992]. On irradiating the IJJ stack the critical current of the junction was found to be suppressed with low RF power and at higher RF power, microwave steps appeared on the IV as shown in Figure 2.25. The fundamental step (FS) appeared with lower microwave power and with further increase in microwave power several smaller steps termed subharmonic steps (SSs) with nearly equal voltage spacing V_s appeared. V_s was two orders of magnitude larger than that based on the Josephson relation $\Delta V_s = f\Phi_0(\approx 20\mu A)$ where f was the frequency of the irradiating microwave. In addition, it was found that the series of SSs were characterised by even and odd steps, respectively, depending on the frequency of the irradiating microwave. The step voltage V_s showed a $\sqrt{P}$ dependence on the microwave power as shown in Figure 2.26. A V_s much larger than the expected value can be interpreted as the phase locking of a number of fluxons.

A similar power dependence of fundamental and subharmonic steps above a critical power P_c was also observed in Irie & Oya [1997]. The linear dependence of the fundamental step height on $\sqrt{P}$ suggested that it was caused by unidirectional flux-flow caused by the external microwave. The origin of the FS and SS were related to the phase locked flux flow and the synchronous coupling between the microwave induced fluxon motion in the IJJ and microwave signal. It was hypothesised that in the naturally stacked Josephson junctions the two-dimensional standing wave associated with the directions of length and height of a mesa, arising from the interactions between fluxons in adjacent junctions, was stabilising the coherent motion of fluxons.

Prusseit *et al.* [1997] observed gap suppression, critical current reduction and

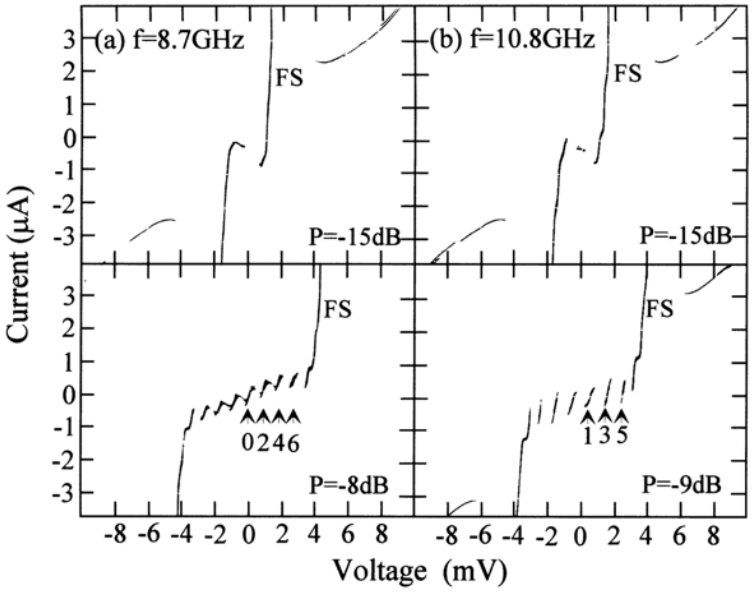

Figure 2.25: IV characteristic of a BSCCO mesa with RF irradiation at 4.2 K. FS is the fundamental step and subharmonic steps are labelled by numbers 0,2,4,6 and 1,3,5. Figure from Irie *et al.* [1996].

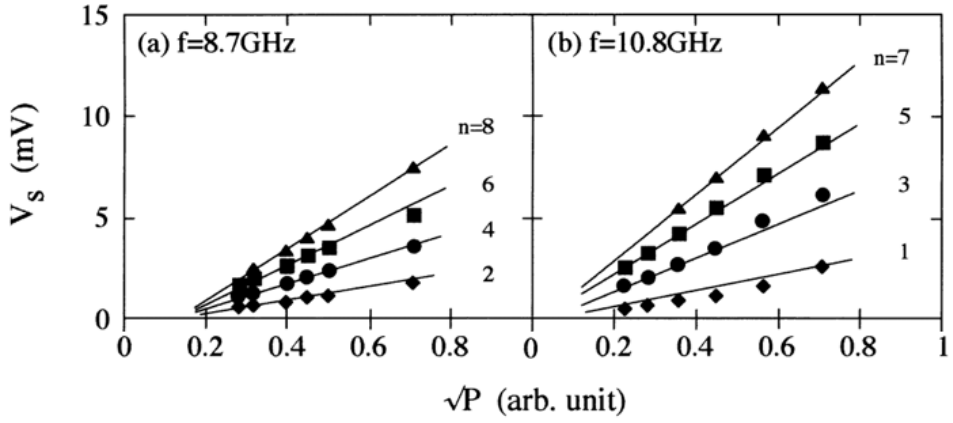

Figure 2.26: Power dependence of the voltage V_s of the microwave induced steps. n is the step number in the dc IV. Figure from Irie *et al.* [1996].

a variety of complex structures in the IJJ IVs under microwave irradiation. Although the IJJs used by Prusseit *et al.* [1997] were about 100 times smaller than the IJJs used in Irie & Oya [1997] study, the results were also explained by coherent vortex motion in the IJJ stack. Although the mesa size was smaller in area than the magnetic penetration depth, it was still larger than the Josephson penetration depth, which determines the scale of phase variations, and hence the junctions could still be treated as long junctions. Vortex-flow motion has been observed in IJJs by other researchers as well [Helm *et al.*, 2000; Krasnov *et al.*, 1999; Odagawa *et al.*, 1999].

A different kind of step structure has also been reported which does not have the $\sqrt{P}$ power dependence [Johnson *et al.*, 1997; Tachiki *et al.*, 2005; Wang *et al.*, 2000b]. These steps can not be explained by fluxon motion. Tachiki explained that these steps were produced by the inverse ac Josephson effect. It was concluded that the step voltage was caused by higher harmonics of the microwave frequency. Tachiki's experimental results and simulations verified the proposed explanation [Tachiki & Uchida, 2007]. In both kinds of steps the observed step voltage is much larger than the Shapiro step voltage from the microwave frequency possibly due to phase locking of more than one junction.

The distribution of microwaves inside the junction stack was studied by Bae *et al.* [2003]. Microwaves were found to be uniformly distributed below a cut-off frequency of approximately 84 GHz as shown in Figure 2.27. Above this cut-off microwaves were found to have a stronger distribution in the middle of the stack. The cut-off frequency was found to be related to the IJJ stack size. Thus, to apply a microwave uniformly across an entire stack of IJJs, it may be desirable to design the stack geometry so as to select measurement frequencies ranging between the Josephson plasma frequency of individual IJJs and the lowest cutoff frequency of the sandwiched stack.

Major result of microwaves application to IJJs is suppression of the critical

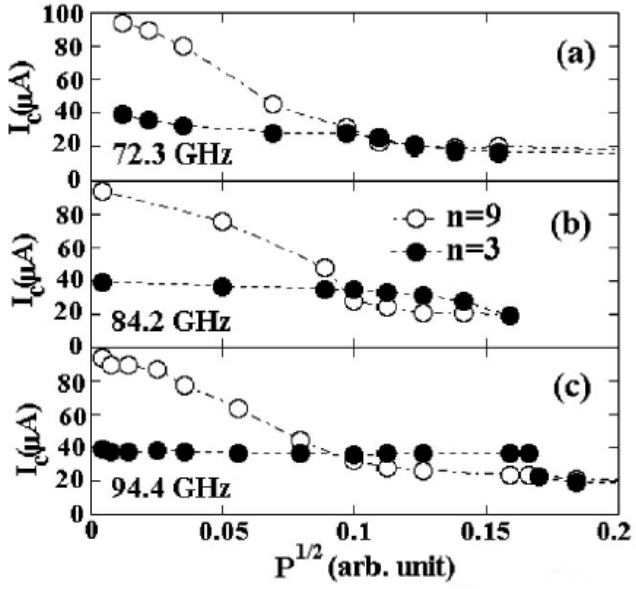

Figure 2.27: The suppression of I_c of the third and the ninth branches as a function of square root of microwave power. The lines denote the average values of I_c, 25mA, and 38 mA, for the frequency range of 70 GHz and 90 GHz, respectively. Figure from Bae *et al.* [2003].

current. Steps on the dc IV appear. The power dependence of the RF-induced steps is similar to flux flow behaviour and hence RF induced steps are termed as flux-flow branches. The distribution of microwaves inside the IJJ stack is dependent upon the stack's dimensions and the plasma frequency of IJJs.

In this chapter basic concepts and theoretical background required to follow the results presented in a later chapter were discussed. Superconductivity and type-I and type-II superconductivity were discussed. The Josephson junction, Josephson equation, different models of Josephson junction and effect of damping and magnetic field on the current voltage characteristics of Josephson junction were also presented. High temperature superconductors and low temperature superconductors were discussed with various types of Josephson junctions realised in these materials. Switching current distribution and previous results of SCD were presented. Effect of microwaves on current voltage characteristics finally concludes this chapter.

Chapter 3

Experimental Details

This chapter discusses the sample preparation and measurement setup. The sample preparation section describes thin film growth, photolithography, argon ion milling and Focused Ion Beam (FIB) processing along with FIB material deposition. The measurement set up section describes details of the measurement probe and its associated electronics. The procedure to obtain current voltage characteristics is discussed followed by switching current distribution of the supercurrent and higher order branches.

3.1 Thin Film Sample Preparation

This section describes the procedure followed to fabricate a thin film sample. Sample preparation starts with the growth of a Tl-2212 film on a $LaAlO_3$ (LAO) substrate. As-grown films were characterised to ensure the phase purity and quality of the film. Photolithography was then used to transfer the device pattern onto the films in the clean room. An argon ion miller was used to remove the film from areas not covered by photoresist. Argon milled films were finally processed in the FIB to make a stack of Intrinsic Josephson Junctions (IJJs) for measurements.

3.1.1 Film Growth

The Tl-2212 thin films were grown on LAO substrates via a two-step physical vapour deposition technique. A typical cycle of film production involved degreasing of the LAO substrate, Ba-Ca-Cu-O amorphous thin film sputtering, and thalliation annealing of the resulting structure in a Tl_2O vapour to crystallise the films in the 2212 phase. The thin films used in this work were grown and characterised by Dr. Susannah Speller and Mr. Michael Korsah of Oxford University[1].

Film growth was a two step process. The first step was sputter deposition of an amorphous Ba-Ca-Cu-O (BCCO) precursor on an LAO substrate. One side polished c-axis oriented [001] LAO substrates were sourced from Crystal GmbH[2]. Crystals had an area of 10 mm by 10 mm and thickness of 0.5 mm. The LAO crystals were used because of good lattice matching with Tl2212 [Bramley *et al.*, 1999; Hollmann *et al.*, 1994; Phillips, 1996; Young *et al.*, 1991]. The LAO substrate was degreased by ultrasonic cleaning in acetone followed by a rinse in methanol. Cleaned substrates were then blow-dried using nitrogen. This removed any surface contaminants which might compromise the film growth and its quality at a later stage. Radio Frequency (RF) magnetron sputtering was used to deposit amorphous Ba-Ca-Cu-O thin films, slightly deficient in copper, in a Nordiko sputterer system. The Cu deficiency gives a better film stability [Speller, 2003]. The films were deposited in an atmosphere of 90%Ar-10%O_2 at a final pressure of 5×10^{-4} mbar. In a typical sputter deposition run, the LAO substrate were mounted onto a copper plate with with an approximate distance of 9 cm below the Ba-Ca-Cu-O target. A deposition rate of 100 nm/30 minutes (confirmed with a cross-section scanning electron microscopy (SEM) technique) was used to achieve a final film thickness of 700 nm. The substrate temperature rose to 100 °C during film deposition due to plasma bombardment. In order to

[1] http://www.materials.ox.ac.uk/
[2] http://www.crystal-gmbh.com

protect the film and its highly reactive elements Ba and Ca from condensation of water vapour, films were allowed to cool down for over one hour before breaking the vacuum. The prepared films were immediately sealed in plastic bags and stored in a desiccator with silica gel before thalliation.

The second step in film growth was thalliation of the BCCO thin film. This process was carried out in a custom-built glove box at Oxford University. In the thalliation process, 0.8 g of freshly prepared $Tl_2Ba_2CaCu_2O_8$ source powder was put in a sealed 2.5 inch alumina crucible together with the amorphous BCCO precursor film , which was positioned in the centre of the furnace. Sealing of the crucible was important as any Tl_2O vapour escaping would result in non-stoichiometric phases. During the thalliation process the temperature was fast ramped from 0 to 600 °C at 900 °C/Hr, and then at a slower rate of 300 °C /Hr to the final temperature which was in the range of 790 to 860 °C; this was maintained for between 1 and 15 hours. After the set time, the furnace was allowed to cool overnight to a final temperature of 50 °C before the film was removed from the crucible. The Tl-2212 film was then sealed in a plastic bag and washed with water for 2 minutes. The fully grown film was then retrieved for microstructure characterisation. A thin layer of gold, about 700 nm was ex-situ sputter deposited to protect the film from the environment.

3.1.2 Sample Fabrication

Sample fabrication consisted of photolithography, Ar ion milling and Focused Ion Beam (FIB) processing. Photolithography was used to transfer the device pattern onto the thin films. Ar ion milling was used to selectively remove the thin film material from the substrate. The final step in the sample fabrication was patterning with a Focused Ion Beam (FIB). An overview of the sample fabrication is shown in Figure 3.1.

Stage 1	
1. Photolithography - Edge bead removal (Mask C1) 2. Expose and develop 3. Photolithography - Device pattern (Mask C3) 4. Expose and develop	1. Mask the central region of thin film covered with S1818, leaving one mm for exposure on all sides. 2. Expose for 20 seconds using 18-20 mW, develop for 20 seconds in a 1:2 mixture (1 part Microposit , 2 parts water) 3. Mask the area of photoresist under the device pattern 4. Expose for 3-4 seconds using 18-20 mW, develop for 20 seconds in a 1:2 mixture(1 part Microposit , 2 parts water)
Stage 2	
Argon Ion milling	Selectively mill away the areas of thin film with no photoresist using Argon ions at 500 volts and beam current of 20 mA for 10 to 20 minutes.
Stage 3	
Focused Ion Beam (FIB) patterning	1. Narrow down the central track to 1 micron using 200 pA current 2. Clean and polish the narrowed track using 10/20 pA current 3. Drill two cuts in the polished side wall to achieve an overlap area using 10 pA current. 4. EHT of FIB during all processing is 30 KeV

Figure 3.1: An overview of sample fabrication process.

3.1.2.1 Photolithography

The first step after film growth for junction fabrication was photolithography. Pattern transfer was achieved by using S1818 photoresist, a 4" ultraviolet photolithography mask and Karl Süss MJB 3 mask aligner. The mask aligner operated at a wavelength of 400 nm and had a resolution of roughly 0.6 μm, which was higher than the smallest features of 4 μm on the device pattern. The exposure power used in this work was 18-20 mW.

Two masks were used in this research for photolithography, both having almost the same design but with different widths of the central track. The mask mostly used for this work was designed by Dr. Jon Fenton and is shown in Figure 3.2. The width of the central track in this mask was 4 μm and the width of connecting arms was 20 μm except for the four end arms, two on either side where width was 70 μm.

S1818 was spin coated at 4000 rpm for 30 seconds on the thin film giving a final thickness of about 2 μm. One millimetre of photoresist from the substrate edges was removed using an edge bead removal mask. The thin film with the edge

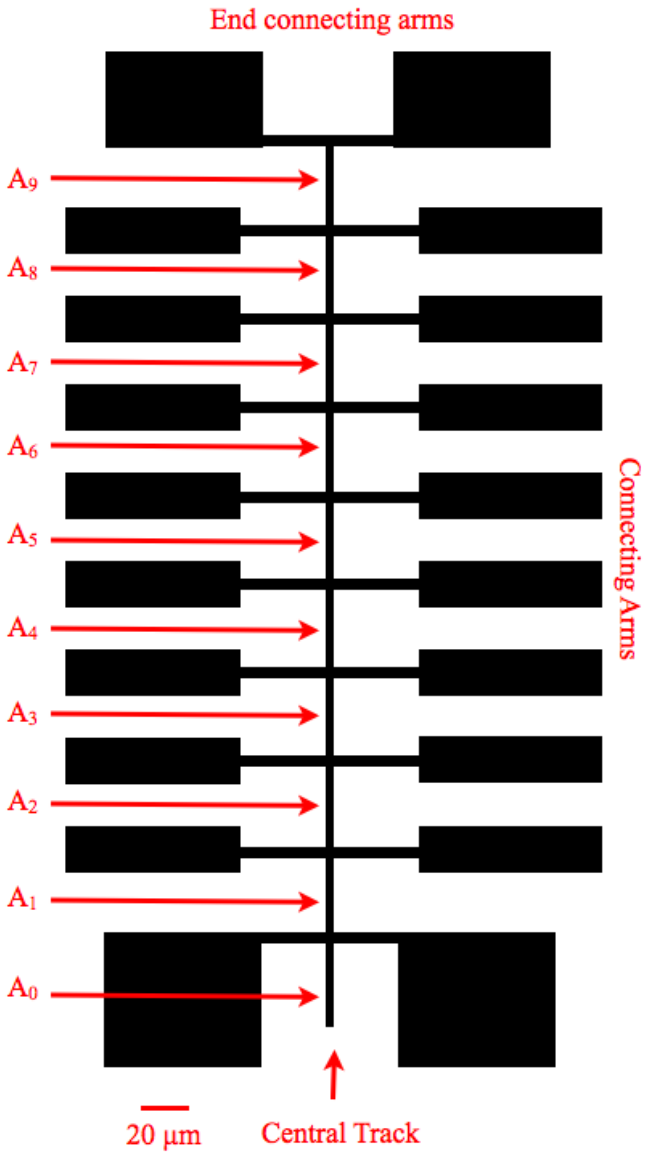

Figure 3.2: Close up of original mask showing 9 sites on central track for FIB processing. Numbering starts from the bottom with A_0 to A_9. A_0 is for identification purposes and is also used for practice runs and alignment in FIB. Actual device pattern where Tl2212 film is left after argon milling is shown in black with annotation in red.

bead mask in contact was exposed to ultraviolet light for 12 seconds and then developed in a mixture of 1 part Microposit 351 and 2 parts water. Edge bead removal was required due to the square nature of substrate, as the photoresist thickness is non uniform and the thickness at the edges was greater than at the centre of substrate. If edge bead removal was not performed, the actual device mask (C3) would not be fully in contact with the film everywhere and the resulting exposed pattern would have poor definition. Edge bead removal was repeated if the optical microscope showed that all the exposed photoresist had not been removed. The actual device pattern was then exposed for 3 seconds at 18-20 mW and then developed for 20 seconds. At the end of this step photoresist had been removed from everywhere on the film except for the actual device pattern. The patterned thin film was then hard baked at 110 °C for one minute to improve the bonding between the photoresist and thin film.

3.1.2.2 Argon Ion Milling

Argon ion milling was used to selectively remove the parts of the thin film not covered by the photoresist. A non localised vertical broad beam of argon ions accelerated through 500 volts with a beam current of 20 mA was used for milling. Control of this step was visual and the decision to stop milling was made by periodic inspections of the film being milled. The milling rate varied substantially with the age of tungsten filament. The milling time also varied depending upon the thickness of film and gold. On average it took about 10 to 20 minutes to mill the films.

This step was performed using argon miller in the nanoscience centre at Cambridge University by Dr. Jon Fenton since no suitable argon ion miller was available at University College London. A picture of an Ar milled track is shown in Figure 3.3.

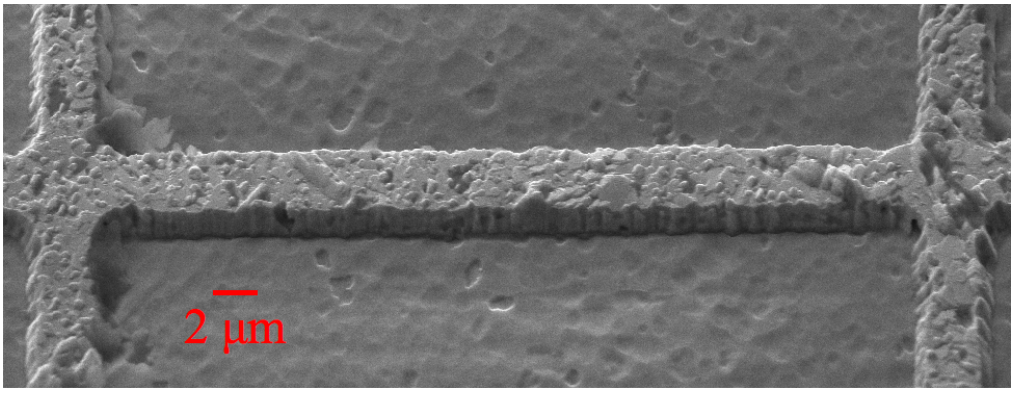

Figure 3.3: Thin film after argon ion milling after removal of the residual photoresist. The horizontal track shows clean, vertical edges.

3.1.2.3 FIB Device Patterning

FIB produces and directs a stream of high-energy ionised gallium atoms, focuses them using electric fields and directs them onto the sample for both milling and imaging. During this research a Carl Zeiss 1540 Crossbeam system as shown in Figure 3.4 was used. The system comprised of a Gemini SEM column from Carl Zeiss with an add-on Orsay Physics Canion 31 FIB column. A broad 3 cm Ar ion miller was added recently. All three beams share the same vacuum space and hence all the processing can be done in a single run without breaking the vacuum and without exposing the sample to air during the processing.

The two most common milling modes of FIB used in this research were 'Mill for time' and 'Deposition' mode. The basic difference between the two milling modes is the beam scanning pattern. In mill for time mode ion beam scans in a line from one side to the other side of the milling object as displayed on computer screen [SMT, 2008]. The mill for time mode calculates the dwell time of the beam by using the milling time, the size of the milling object, the increment style and the number of layers. The depth of the milling pattern results from these parameters and is material dependent [SMT, 2007]. In deposition mode the object area is evenly exposed to the ion beam. The beam is scanned in a continuous raster

fashion from one side to the other side and back. Beam movement is controlled by two scanning frequencies, X scan frequency for control in horizontal direction and Y scan frequency for vertical control.

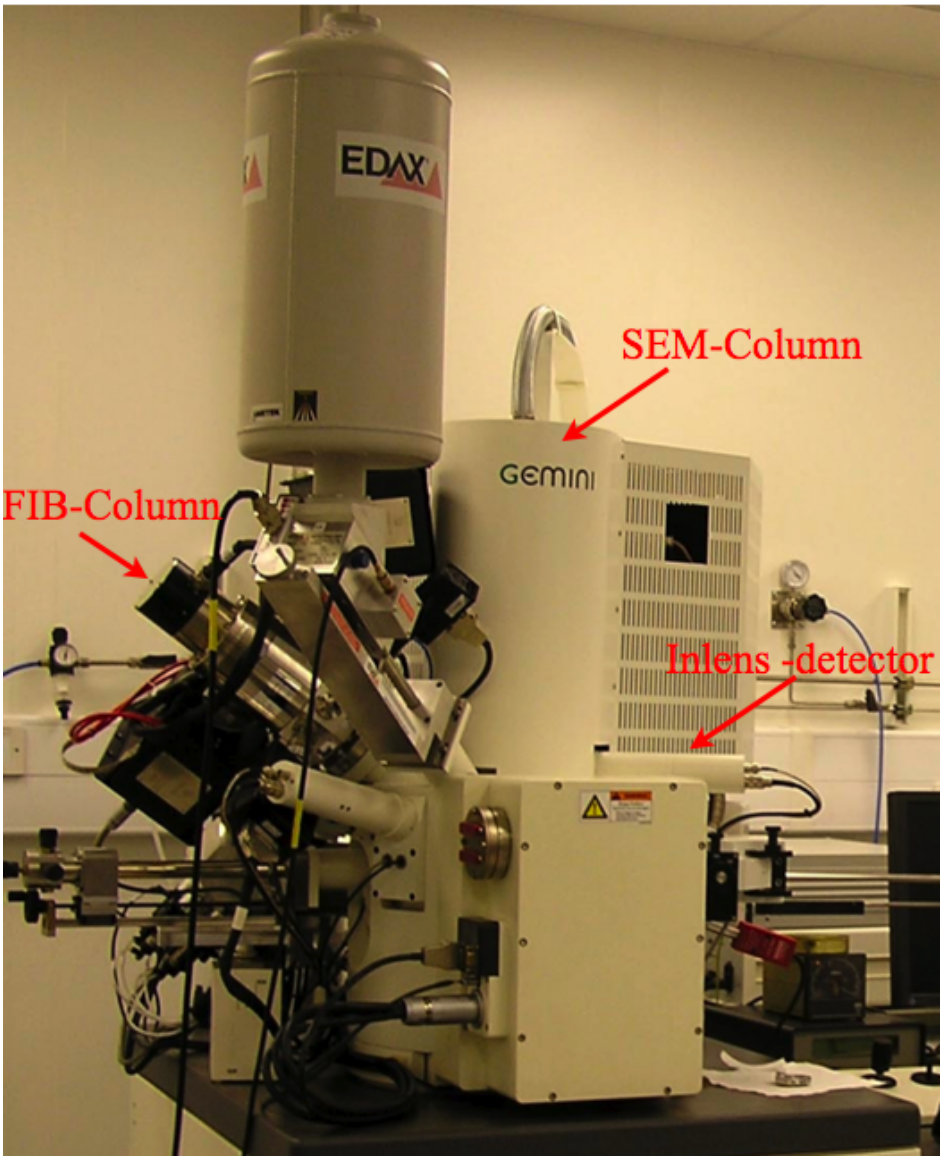

Figure 3.4: Triple beam Leo 1540 at UCL. The SEM column is vertical labelled 'Gemini'. The FIB column is mounted 54°from the vertical axis on the left. A 3 cm 1 kV argon gun is also installed (not visible in picture). The system has an energy dispersive x-ray spectroscopy system; the coolant storage tank is shown in the picture labelled 'EDAX'.

The sample was mounted on the universal stage and grounded with either silver paint or carbon tape for FIB processing. FIB processing was done in three

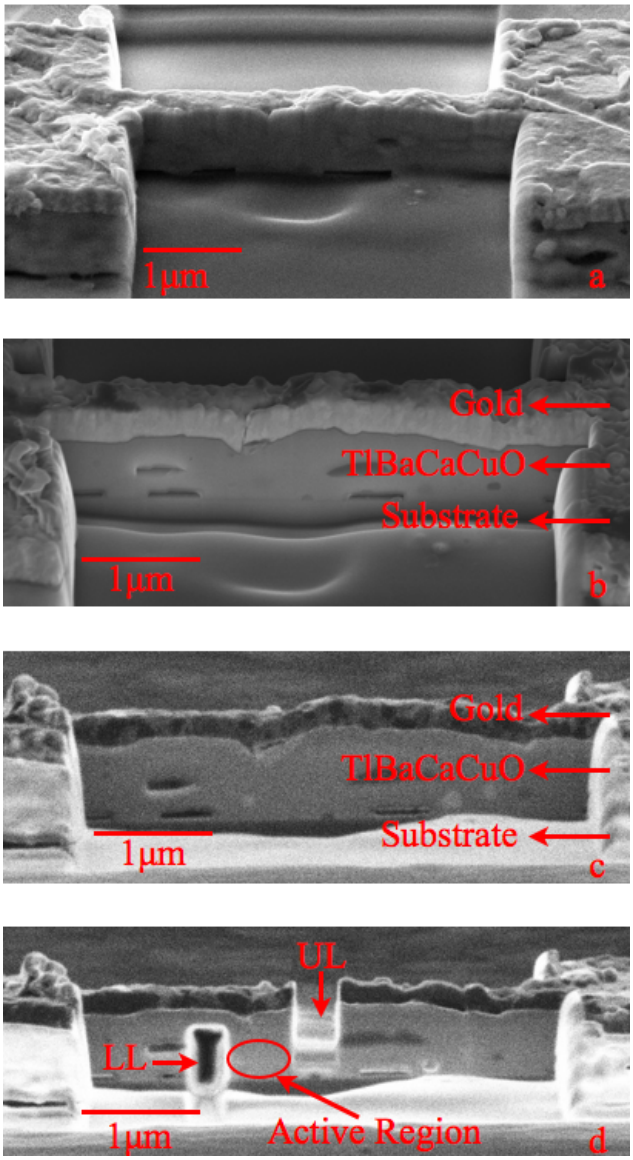

Figure 3.5: FIB patterning:(a) SEM view of a narrowed down track using 200 pA. Note that the layering interface between gold & Tl2212 and Tl2212 & substrate is not visible. (b) SEM view of a track which has been polished to remove the amorphous region. Interface between different layers is clearly visible. (c) FIB view of the polished track. The FIB Beam is at 5°to the substrate. (d) FIB view of a fully prepared, device geometry showing the active region i.e overlap region between the Upper Lateral (UL) cut and Lower Lateral (LL) cut. Imperfections in the film are also visible.

steps, narrowing down of central track, polishing of the track and lateral drilling as shown in Figure 3.5. The first and second steps are performed with the FIB beam perpendicular to the central track whereas for the third step FIB beam is at an angle of 5°to the central track. In the first step a small region of 4 to 6 microns in length was narrowed down from both sides. The width was reduced from 4 microns to one micron. Reduction of the width was required to make a sub micron junction area and to reduce the time of lateral drilling in step 3. This narrowing down makes the sloping side walls become vertical. Narrowing down was usually done in deposition mode with a 200 pA beam current, an X scan frequency of 20000 Hz and a Y scan frequency of 0.2 Hz. The interface between the Gold and Tl2212 layers was not visible at the end of the first step due to the presence of amorphous material generated by the high FIB current as shown in Figure 3.5 a.

The second step in FIB fabrication was to polish the narrowed down track to remove the amorphous material from the first step. Polishing was done using a lower FIB beam current of 10 pA or 20 pA in mill for time mode with typically the time set to 800 seconds and the number of layers set to 80. The width of the polished track was typically about 500 nm to 600 nm. Polishing improved the interface detail as shown in Figure 3.5 b.

Two lateral cuts were made in the central track in the third FIB fabrication step; one labelled Upper Lateral (UL) and the second one labelled Lower Lateral (LL). An FIB beam current of 10 pA was used in deposition mode with X scan frequency of 20000 Hz and Y scan frequency of 0.2 Hz. The FIB beam was at 5°to the substrate while drilling UL and LL. This is the minimum angle required to avoid charging up of the insulating substrate. A complete device is shown in Figure 3.5 d.

3.1.3 Problems in Sample Preparation

The sample preparation procedure discussed above although straightforward, had two specific problems which occurred repeatedly:

- The width of the central track was too narrow after the argon ion milling step.
- Sample charging in FIB.

3.1.3.1 Track Thinning

The whole procedure of photolithography and Ar ion milling would ideally result in a sample with a central track having clean vertical walls ready for FIB processing as shown in Figure 3.3. However, at times the resulting sample at the end of the Ar milling step had a very narrow central track width. This could not be used to make stacks of IJJs in FIB. One such sample is shown in Figure 3.6. If we compare this sample with the one shown in Figure 3.3 we see that the width of central track is much narrower and the side walls are sloping and not vertical.

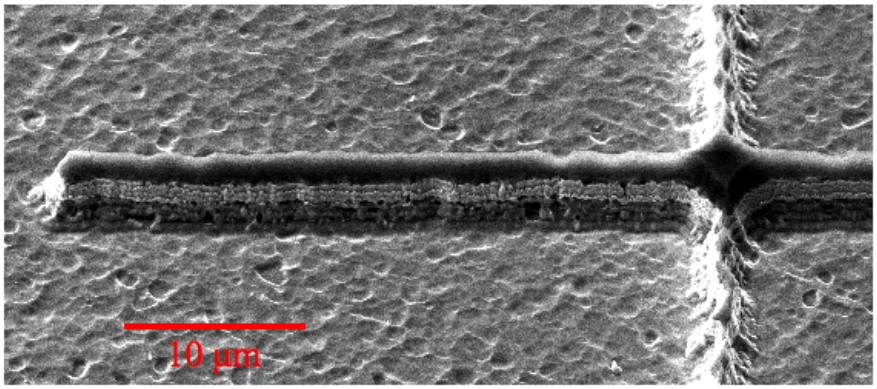

Figure 3.6: A thin film after photolithography and Ar Ion milling. The width of the central track is considerably narrower and the side walls are sloping as compared to Figure 3.3. The top most layer (dark in the image) is photoresist.

One reason for track thinning could be poor contact between the mask and thin film during photolithography. Poor contact can be due to uneven film thick-

ness due to edge bead. Poor contact between the mask and film was avoided by removing the thicker edge bead. Contact between the mask and substrate was ensured by observing colour fringes on the substrate when mask was in contact with the film substrate. The area of unexposed photoresist will be narrower than on the actual mask if there is poor contact. In order to ensure that films are exposed correctly and the width of unexposed photoresist track was the same as on the mask, films were inspected under a powerful optical microscope (maximum magnification 1000 times). The films were reprocessed whenever the final patterning in the lithography was not satisfactory.

The end point detection in Ar ion milling could be another problem. The milling time was a trade-off between over-thinning of the tracks by milling too long or leaving material between the tracks by milling too little. Both of these problems can be overcome by increasing the width of central track. A new mask was therefore designed using Layout Editor[1]. This was essentially the same as original mask design but with wider central track width. The width of the connecting arms was also made uniform throughout their entire length and increased to 20 μm. A close up of part of the new mask plate is shown in Figure 3.7. The new mask has different devices with central track widths of 6 μm, 10 μm, 14 μm and 18 μm. The mask was manufactured by Compugraphics Limited.[2]. The increased central track width ensured that samples could be patterned in the FIB even if they were over-milled.

3.1.3.2 Sample Charging in FIB

The FIB uses ionised gallium for imaging, milling and metallisation. When these charged ions strike an insulating surface or a conductor which is not properly grounded, a charge starts to build up. One immediate effect is instability in the FIB image. The FIB image starts to move depending on the severity of the charge

[1] http://layout.sourceforge.net/

[2] Compugraphics International Ltd, Glenrothes, Fife, KY7 4NT, UK

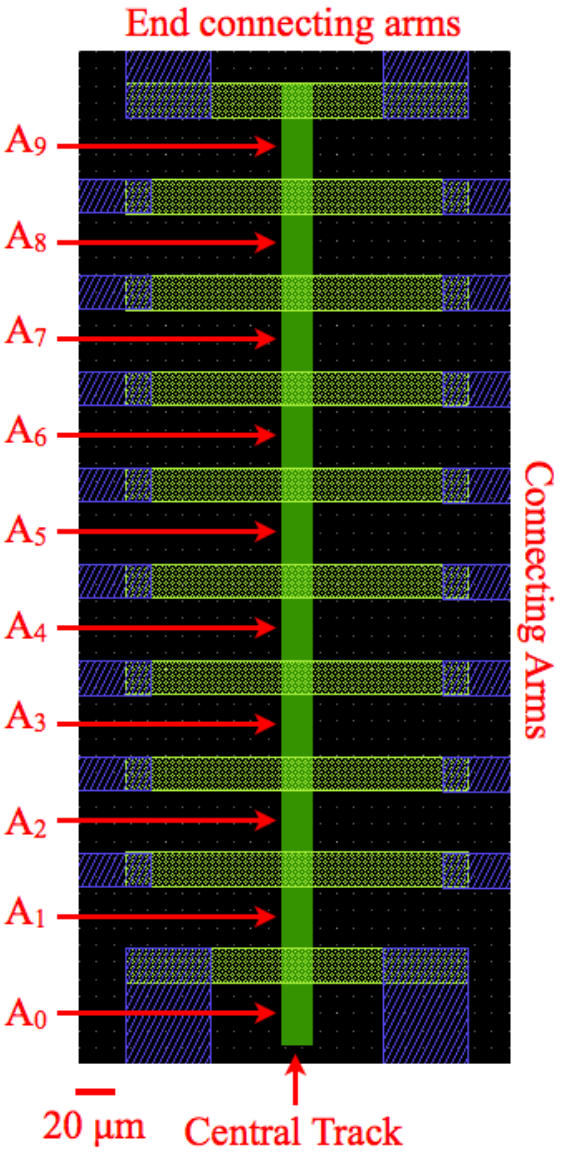

Figure 3.7: Close up of the new mask showing increased width (18 μm) of the central track shown in green. The width of the connecting arms was made uniform (20 μm) throughout.

build up. To avoid sample charging the sample needs to be properly grounded.

Initially Agar Scientific's [1] silver paint G3648 (silver paint) was used to ground the thin film to the SEM stub. This provided a very good and quick grounding mechanism. One problem realised on repeated application and removal of silver paint was the presence of stray particles of silver paint on thin films. An SEM image of such stray flakes is shown in Figure 3.8.

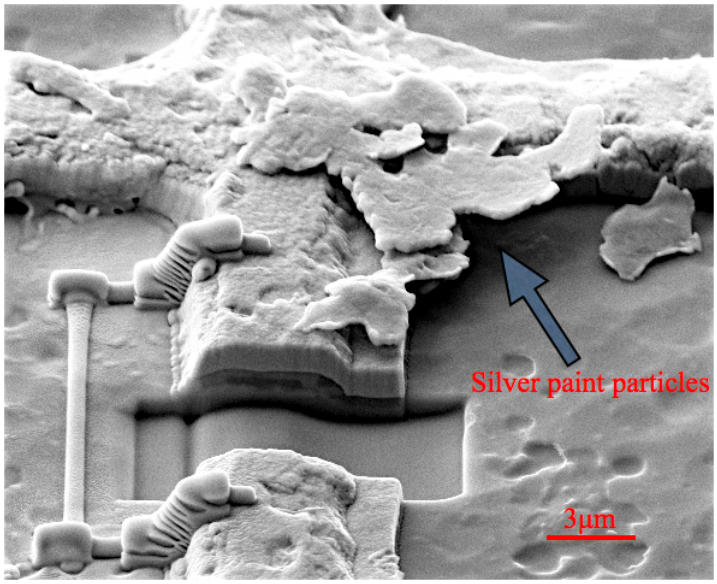

Figure 3.8: Small portions of silver paint used to mount and ground the sample on SEM stub can break off and stick to the substrate. These flakes cause charging in the FIB and this results in an unsteady image.

These stray particles cause severe charging and depending on their location, it might not be possible for the LL and/or UL cuts to be drilled. To avoid this problem, silver paint was replaced by conducting carbon tape, G3939 from Agar scientific. Figure 3.9 shows carbon tape used to ground the sample.

[1] http://www.agarscientific.com

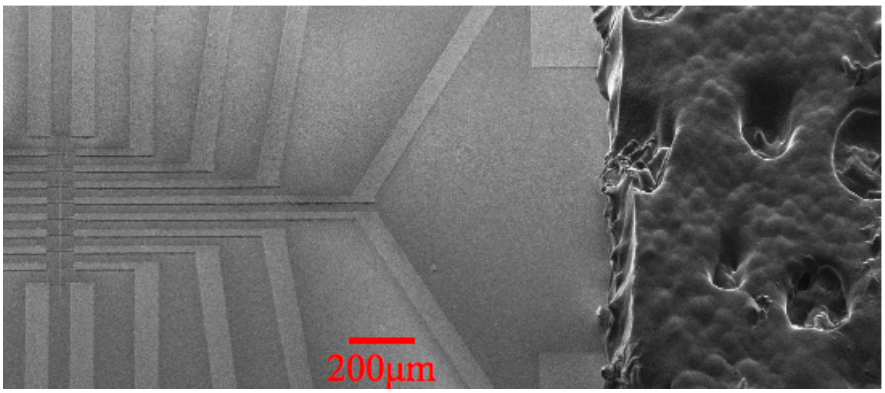

Figure 3.9: Double sided carbon conducting tape visible on the right side in black is used to mount and ground the thin films on the SEM stub.

3.2 Focused Ion Beam (FIB) Deposition

FIB deposited tungsten was used to isolate the IJJ stacks from environment. Principle of FIB tungsten deposition is shown in Figure 3.11. A gas precursor of Tungsten hexacarbonyl, $W(CO)_6$ was introduced close to the sample surface through the GIS nozzle. The precursor created a local high pressure in the region scanned by the ion-beam and was adsorbed on the surface. Focused Ga ion beam decomposed the adsorbed gas molecules on sample surface and converted them to non-volatile and volatile products. Volatile products of the decomposition desorbed from the surface and were removed through the vacuum system. Non-volatile products i.e W was left fixed on the sample surface. Deposited material was not pure as it contains some of the Ga^+ ions and other amorphous materials such as carbon.

To perform tungsten deposition, the sample was put inside the chamber, and the tungsten source and control capillary were heated. The sample was then moved to the incident point (working distance of 5 mm from SEM column) at an angle of 54 °as shown in Figure 3.10 to make the sample perpendicular to the Gas Injection System (GIS) and FIB. The tungsten nozzle was brought to the sample once the tungsten reservoir was heated to the required temperature.

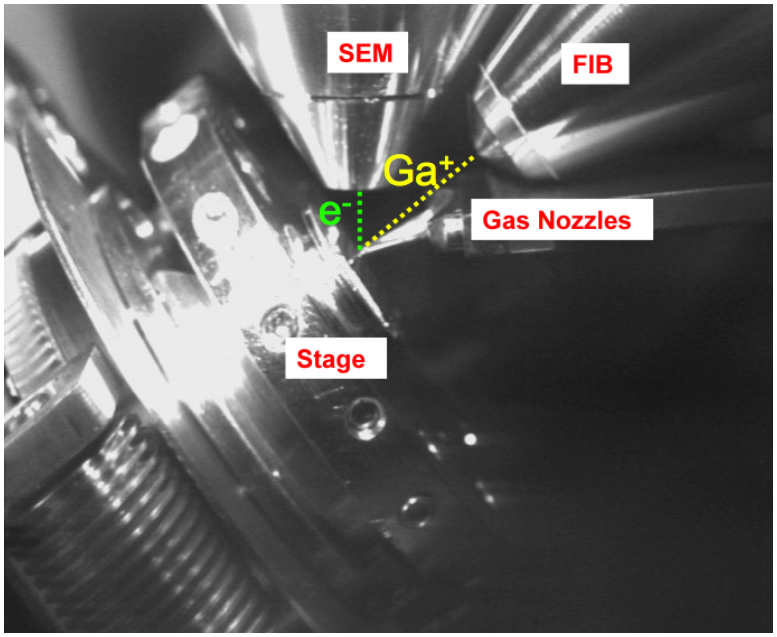

Figure 3.10: Schematic showing sample and nozzle position during FIB deposition.

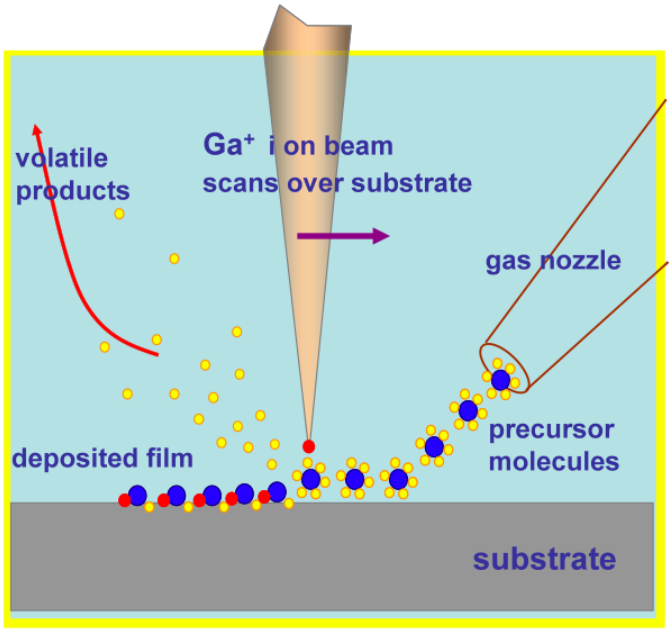

Figure 3.11: Principle of FIB deposition.

The typical temperature for tungsten reservoir during deposition was 67 °C to 69 °C. A deposition object was drawn on the computer screen at the required place with the deposition beam current set to typical value 20 pA, The X scan frequency (20 kHz), Y scan frequency (0.2 Hz) and deposited material (tungsten) were selected before opening the control valve to allow the gas precursor to enter the vacuum chamber. It is pertinent to mention that the Leo 1540 software can only allow a rectangular object to be drawn for deposition. The typical base chamber pressure before introduction of the precursor gas was 2.4×10^{-6} mbar and during deposition it was between 1-2 $\times 10^{-5}$ mbar.

It is important to remember that incident ion beam not only breaks down the precursor gas for deposition but it also mills at the same times. In order to maximise the deposition rate and minimise the milling rate, right value of ion beam current has to be selected. Selection of ion beam current depends on the deposition area, an empirical value of 100-150 pA/μm^2 for $W(CO)_6$ is recommended [Yao, 2007]. Lower beam currents than the recommended value although has a slower milling rate but it will not decompose all the gas and therefore will have a slower growth rate and long deposition time. In contrast a too high value of beam current will have a higher milling rate than the deposition rate as all gas is used up by only part of ion beam and the remainder ions then mill the sample.

3.3 Measurement Set up

The FIB patterned sample was mounted on a custom made chip carrier and electrically wired using silver paint. A sample mounted on a chip carrier is shown in Figure 3.12. The chip carrier was inserted in the receptacle on a dip probe as shown in Figure 3.13. A mu-metal shield was used to screen the magnetic field from the sample space. The sample was cooled down by inserting the dip probe in a dewar of liquid helium. Control of the sample temperature was obtained by controlling the height of the dip probe inside the dewar. Two types of measurements were performed on the fabricated samples: current-voltage characteristics and switching-current distributions. Both measurements use the same dip probe but different current control electronics.

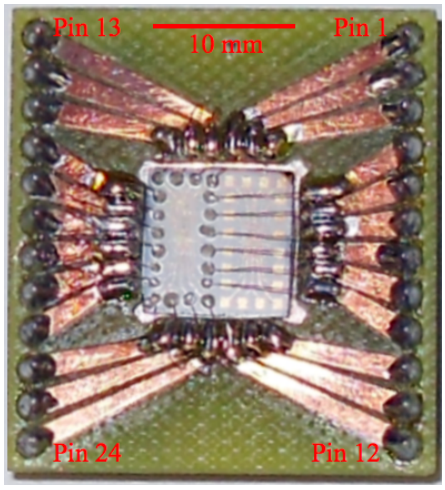

Figure 3.12: A thin film chip mounted in the chip carrier ready for measurement. One complete half with 9 sites wired is shown.

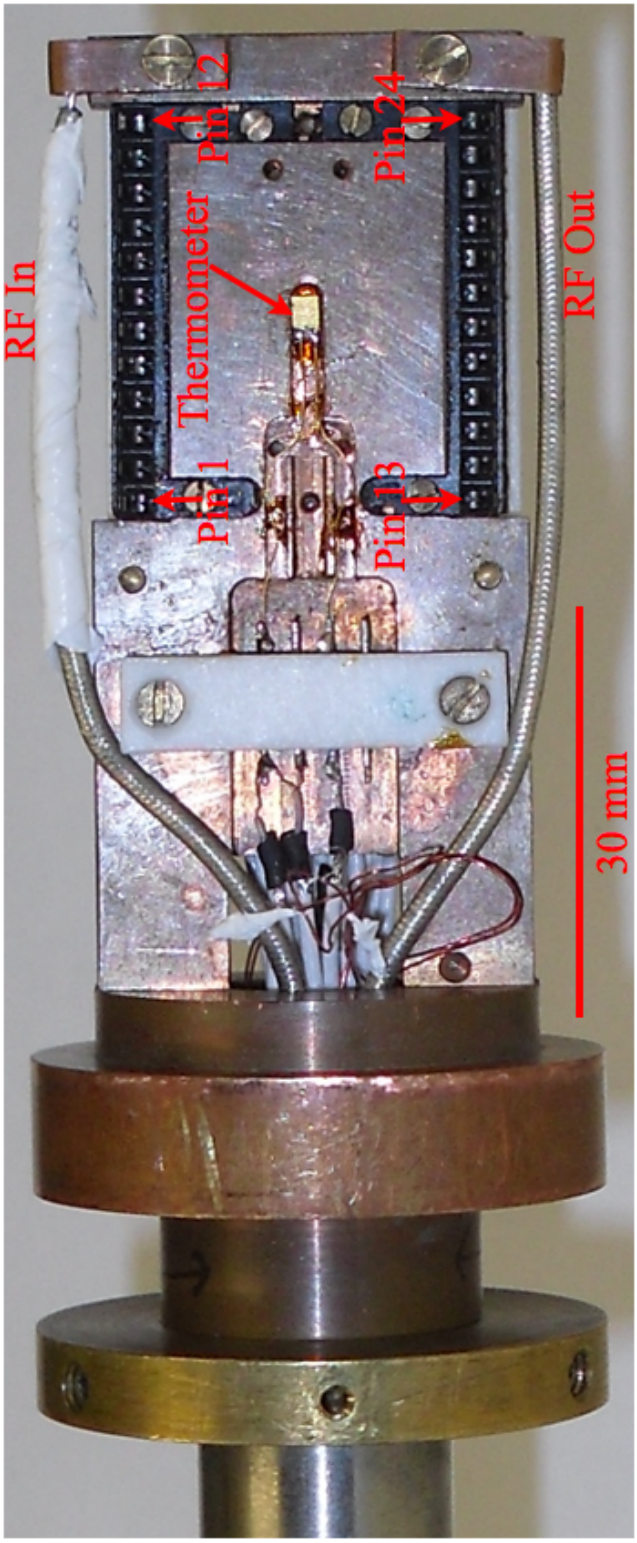

Figure 3.13: Lower portion of dip probe with housing arrangement for chip carrier. The groove in the middle of copper block houses the temperature sensor, CX-1070-SD-4L from LakeShore which has a resolution of 36 μK at 4.2 K. The RF in cable at the top has PTFE tape around it to prevent shorting the sample. Connecting wires from sample pass from the back of copper block to inside of metal tubing. The circular disc towards the left shows the holes where the mu-metal shield (not shown) is fixed.

3.3.1 Dip Probe

The dip probe was designed and built by Dr Asan Kuzhakhmetov, a former member of the group. The dip probe has three major parts. The lower portion has a receptacle housing for the custom made chip carrier. The chip carrier receptacle is built around a copper block as shown in Figure 3.13. A groove in the copper block houses the thermometer for sample temperature measurement. The thermometer used for temperature measurement is CX-1070-SD-4L from LakeShore which has a resolution of 36 μK at 4.2 K. Two semi rigid RF cables running from the top of the probe are also terminated in the lower portion; one of these was used for feeding the RF signal to the sample space. A total of twenty-four sample coaxial lines (not visible in Figure 3.13) are soldered at the back panel of the chip carrier receptacle.

The middle portion of the dip probe consists of a hollow tubing. All wires including sample coaxial lines, thermometer wiring and RF cables coming from the sample space pass through this tube to their associated electronics at the top of the probe. The hollow tubing besides providing the space for housing the wiring provides the mechanical strength and a means of coarse temperature control by controlling the height of the sample inside the helium dewar.

The top portion of the probe consists of a voltage amplifier, an analogue current source, a programmable matrix board and filters. Sample coaxial lines from the sample pass through miniature threaded LC circuit filters DLT4/L/22000 from Oxley. These filters remove unwanted noise and attenuate undesired signals. The filters have a typical insertion loss of 12 dB at 1 MHz and 70 dB at 10 GHz. The outer conductors of all the sample coaxial wires are connected to the common chassis ground. The RF cables are connected to their respective male SMA connectors ANNE-50X at the top of the probe and have a frequency range of dc - 40 GHz.

All sample coaxial lines after passing through the filters are connected to a

programmable matrix board from Farnell. The matrix board consists of two parallel decks with bus bars at right angles to each other. Contact between the bus bars is made by using a contact plug. Selected sample coaxial lines are connected to the current source and voltage amplifier. Use of the matrix board allows us to measure any of the wired devices by using contact plugs in a four terminal fashion without having to extract and reinsert the probe.

3.3.2 Current - Voltage Characteristics

An overall block diagram of the current voltage measurement set up is shown in Figure 3.14. The measurement set up consists of a manual DC current control, analogue current source, patch panel, filters, voltage amplifier, temperature controller (used only for reading the sample temperature) and RF source. A manually controlled multi turn variable resistor inside the current control provided the driving voltage for the current source. Current from the current source routed by the patch panel and filtered by LC filters was fed through the IJJ stack, represented by the X in Figure 3.14. The voltage across the junction stack was fed to the voltage amplifier after filtering. The analogue value of the current to the sample and the voltage from the amplifier was fed to the data acquisition card inside the PC. The sample temperature was also recorded using a GPIB interface. Data acquired was then displayed and saved to a text file using Labview code originally written by Dr Asan Kuzhakhmetov. Major modifications were made later by Dr Jon Fenton. I modified the existing code on requirement, e.g for switching current distribution measurements.

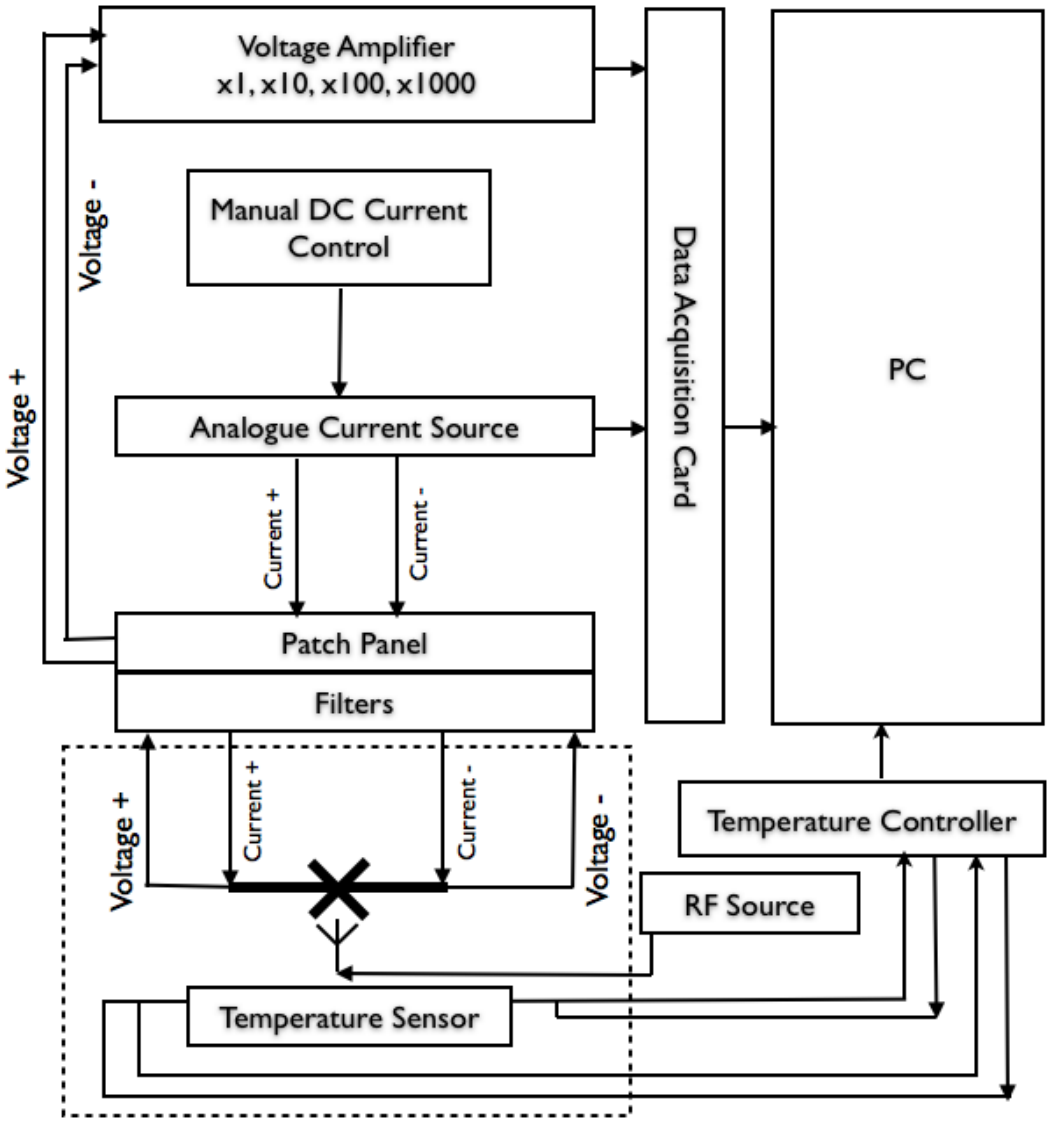

Figure 3.14: Schematic view of the I-V measurement set up. The area inside the dotted rectangle includes the IJJs (shown by the cross), the temperature sensor and RF antenna and is inside the liquid helium dewar, while the rest of the electronics is at room temperature. The temperature controller was used only to read the sample temperature.

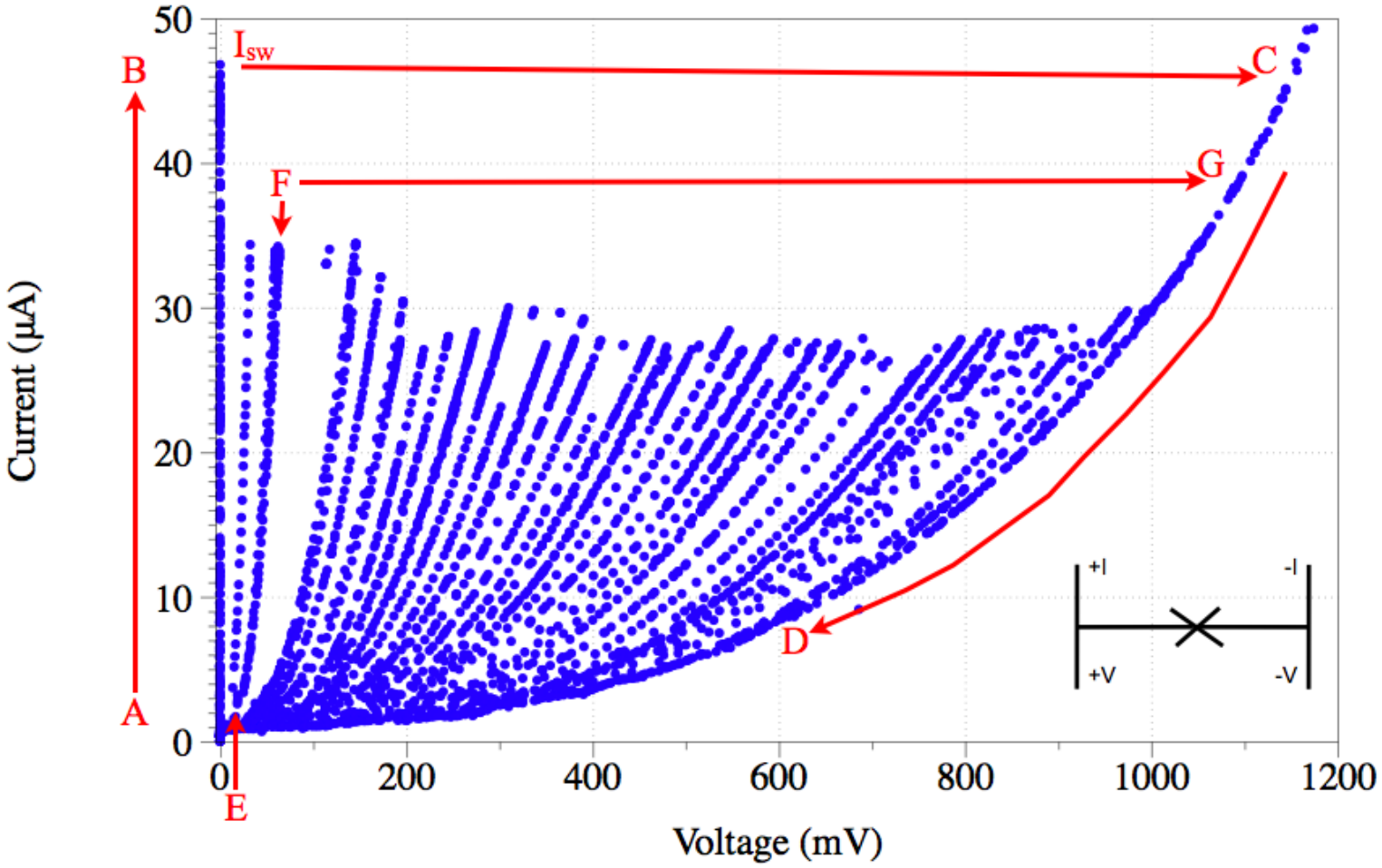

Figure 3.15: Current-Voltage characteristics of an IJJ stack at 4.2 K. Actual data points are shown in black. Red arrows indicate the path to obtain the data shown. I_{sw} represents the switching current of the supercurrent branch (Branch 0). The IJJ array is represented by a cross and the four terminal configuration is shown.

Current voltage characteristics were obtained using a four terminal configuration. Typical IV characteristics of an IJJ stack are shown in Figure 3.15. The junction stack is current biased to obtain these characteristics. To obtain the IV characteristics shown in Figure 3.15, the current was manually increased from zero to I_{sw} (47 μA in Figure 3.15) along the arrow from A to B. This branch with no voltage is called the supercurrent branch or branch 0. When the current value reached I_{sw} the IJJ stack switched from the zero voltage state (point B) to voltage of about 1.1 volt (point C). The current was then reduced from C to D and then to E. The current was increased again from point E allowing us to trace one branch of the IJJ stack (from E to F). When the current reached the switching current of the E-F branch, the IJJ stack again switched to high voltage value along F to G. All the branches in the IJJ stack can be traced by this repeated increase and decrease in the biasing current.

3.3.3 Switching Current Distributions

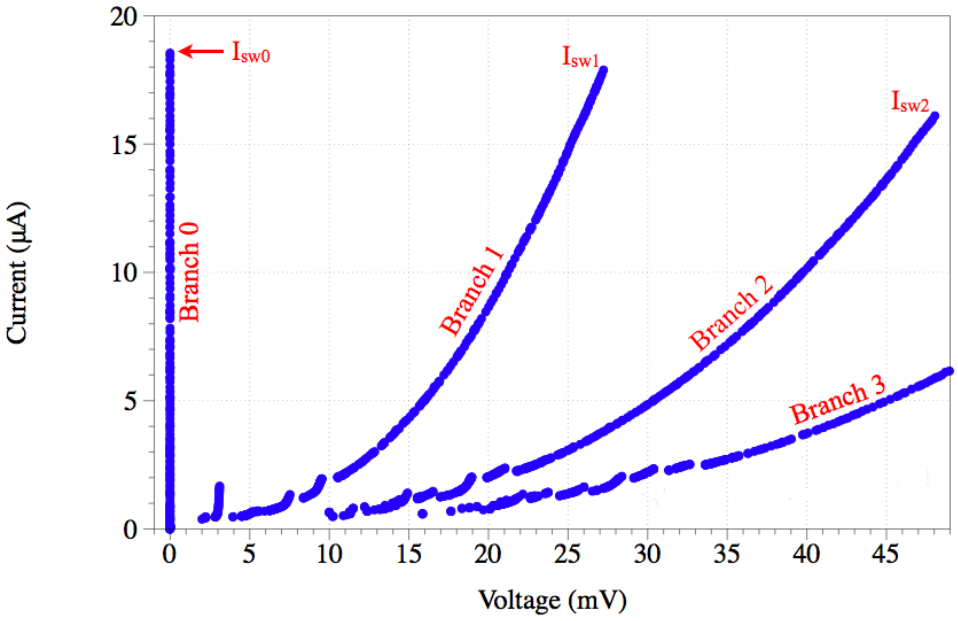

Figure 3.16: Low-voltage region of the IV characteristics of a sample at 4.2 K. Only the first four branches are shown.

Switching current measurements were made once the IV characteristics had been measured. The low-voltage region of the IV characteristics of a sample is shown in Figure 3.16. Switching current measurements were divided into two groups: one from the supercurrent branch (branch 0) and the other from all other higher order branches e.g branch 1, branch 2 and so on. Switching current measurements build up a histogram of the switching current values on each branch. Typically 5000 measurements were made for each histogram. To build up a histogram, the basic measurement set-up was same as shown in Figure 3.14, but the manual dc current control was replaced with an automatic current control.

3.3.3.1 Switching Current Distribution of Supercurrent Branch (Branch 0)

To measure the switching current distribution from the supercurrent branch the manual dc current control in Figure 3.14 was replaced by a triangular wave generator. Either a custom-built triangular waveform generator or a commercially available function generator from RS Components were used to measure switching current distributions from the supercurrent branch.

To measure the switching current distributions from the supercurrent branch, current was ramped up at a constant ramp rate of typically few mA/sec from A to B as shown in Figure 3.17. The amplitude of triangular wave was adjusted to obtain a peak current slightly more than the maximum switching current I_{sw0} of the supercurrent branch. A threshold voltage V_{th0} set close to the supercurrent branch was monitored to detect a switch. Typical values used for V_{th0} were below 1 mV. Once the IJJ stack switched from the zero voltage to the voltage state and a voltage greater than the V_{th0} was detected, the current value at which the switch occurred was recorded. The current was ramped to the maximum amplitude (slightly higher than the maximum switching current) and then ramped down. Whilst ramping down the current followed the same path as already discussed in

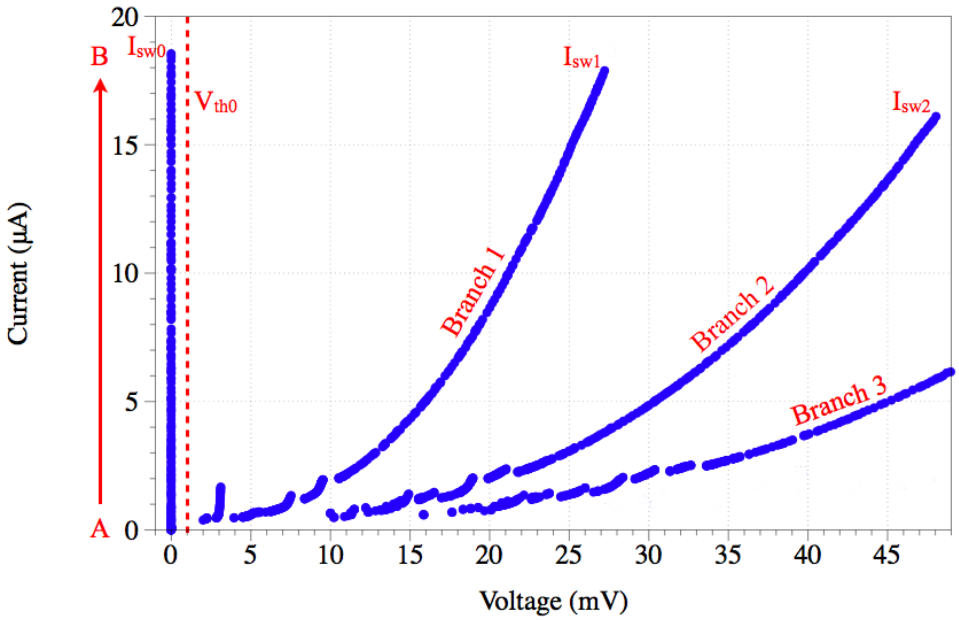

Figure 3.17: Switching detection from supercurrent branch. A switch is recorded whenever a voltage greater than V_{th0} was detected on an increasing current ramp.

section 3.3.2. Once the current reached zero, it was ramped up again to record the next switch. This automatic repetition of ramping up and ramping down of the bias current enables the histogram to be collated. The switching current distribution of the supercurrent branch (branch 0) of the sample shown in Figure 3.16 is shown in Figure 3.18.

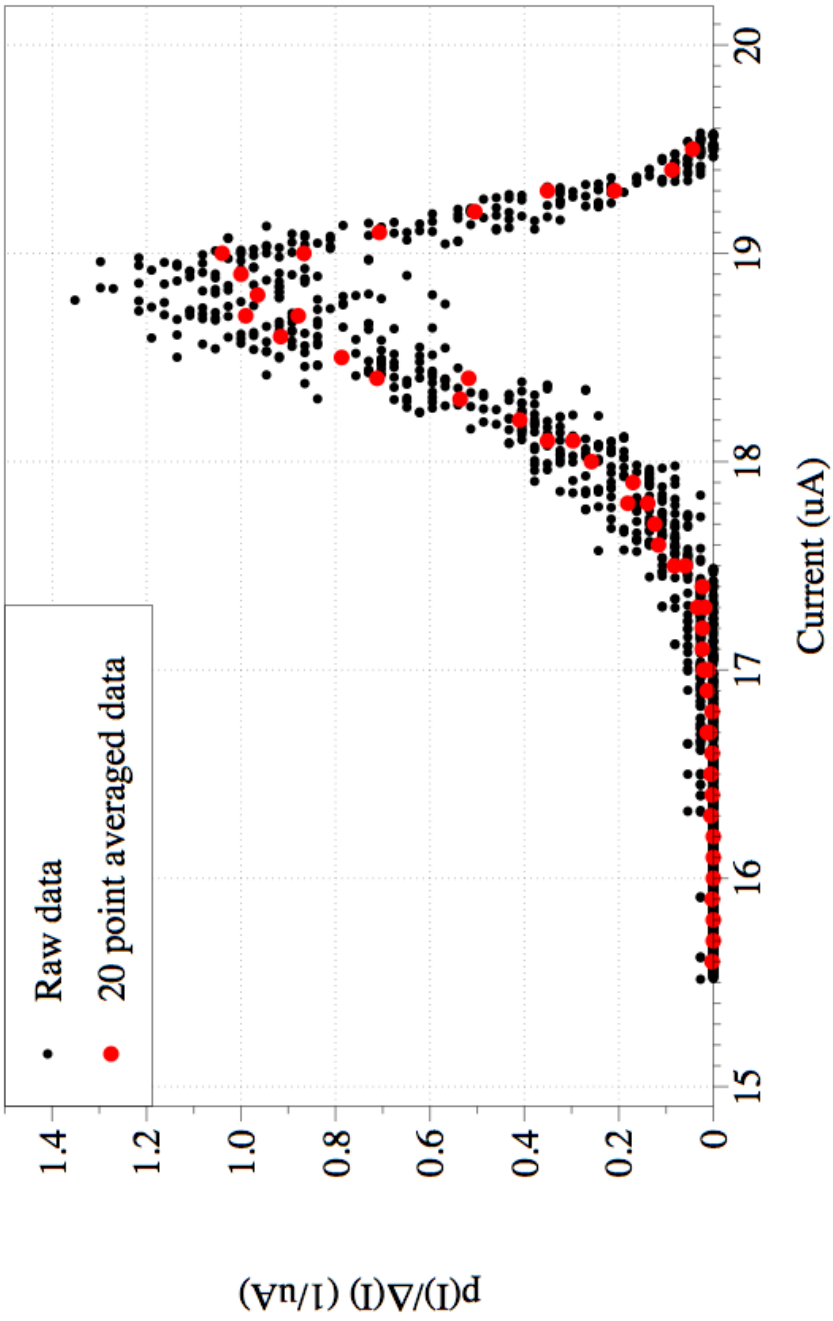

Figure 3.18: Switching current distribution histogram of branch 0 of Mk86-A3 at 6.04 K shows the switching current against the probability of switching within a bias current range I to $I+\Delta$I. Black points show the experimentally measured data with current resolution ΔI_{ADC} of 3.7 nA. Red points show the averaged data where the current bin size (ΔI) was 74 nA with 20 current bins.

3.3.4 Switching Current Distribution of Higher Order Branches

In order to measure the switching current distributions from higher order branches e.g branch 1 in Figure 3.19, a simple triangular wave current control could not be used for two reasons. First, the larger switching current of branch 0 would switch the IJJ stack to a higher voltage rather than to the closest branch i.e branch 1. Secondly the triangular current control did not have the provision for current ramp direction control based on control criterion definable by user. It would only change the ramp direction once it has reached the maximum amplitude set by the user. A new current control was designed and fabricated to measure switching-current distributions from higher-order quasiparticle branches. The original concept was proposed by Dr Paul A. Warburton.

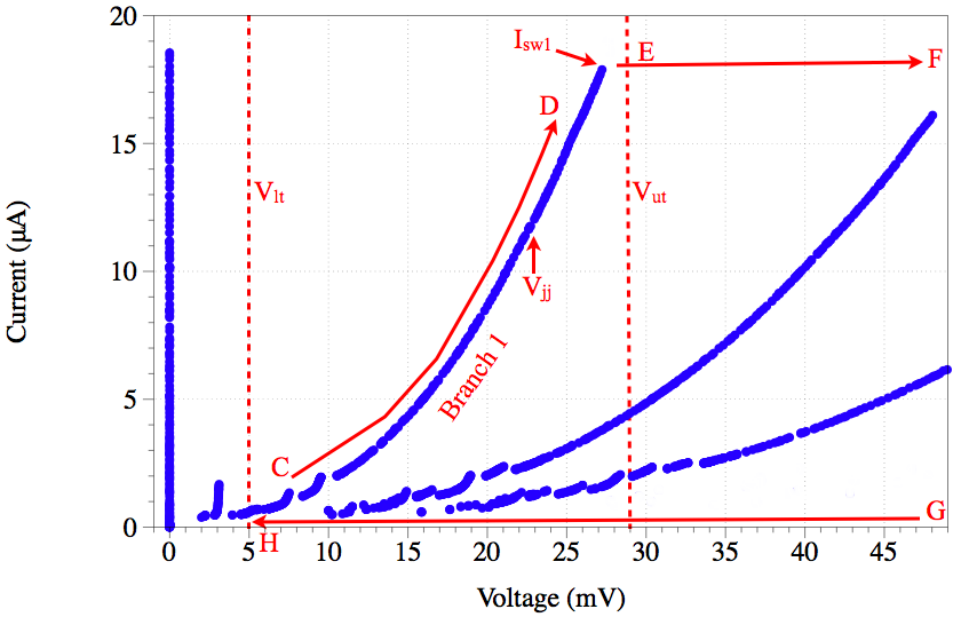

Figure 3.19: Technique for measuring switching events from branch 1. The junction stack voltage V_{jj} is continuously compared with two preset voltages, V_{ut} and V_{lt} to control the direction of current ramp.

The proposal was taken up as an undergraduate project by Mr. Hassan Ali, who designed and implemented the current control in its early form. The circuit was later redesigned and improved upon by Dr Jon Fenton and by me. The block

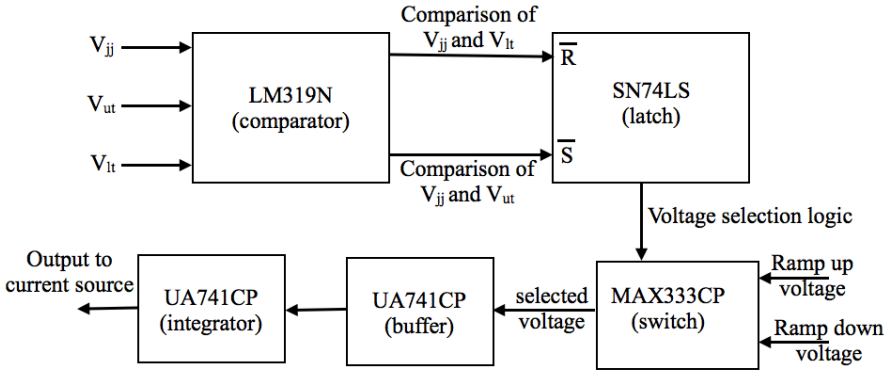

Figure 3.20: Block diagram of the automatic sweep generator. The sample voltage V_{jj} is continuously compared with two preset voltages, V_{ut} and V_{lt} to change the direction of current ramp. The latch provides input to the selector switch, which selects the ramping voltage input for the integrator.

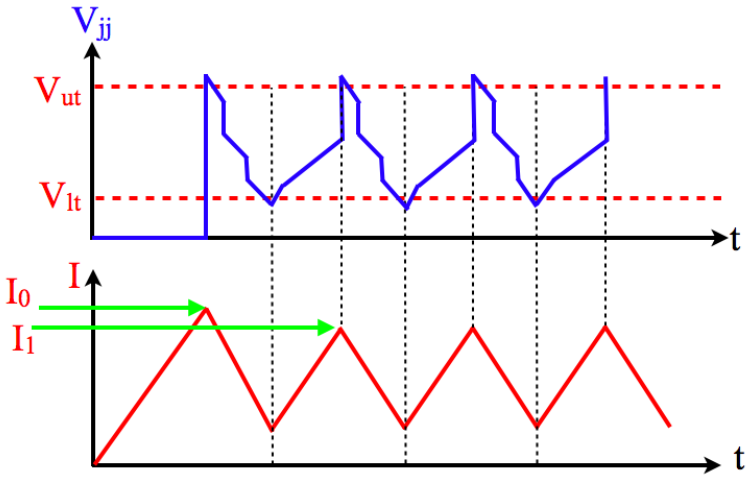

Figure 3.21: Current-Voltage pattern while measuring switching current distributions from branch 1. Comparison between the sample voltage V_{jj} (blue) is done with the two preset voltages, V_{ut} and V_{lt} (red lines in the upper picture). Changes in current ramp direction (lower picture) occurs when V_{jj} crosses any of the preset threshold. I_0 is the switching current of branch 0 which has a higher value than the I_1, switching current of branch 1.

diagram of the circuit in its final form as used is shown in Figure 3.20.

The measurement setup to measure switching current distributions from higher order quasiparticle branches consists of the same setup as described in Figure 3.14 with the manual DC current control replaced by the new automatic current control shown in Figure 3.20. The circuit works by comparing the measured sample voltage, V_{jj} across the IJJ array, against two preset threshold voltages specific to the branch being measured as shown in Figure 3.19. The two threshold voltages are termed the upper threshold voltage, V_{ut} (about 29 mV here) and the lower threshold voltage V_{lt} (about 5mV here). These threshold voltages act as the control point for current ramp direction reversal. The current is ramped up along branch 0 until the junction stack switches to a high voltage (not shown in this graph) as described in section 3.3.2. Once the junction stack has switched to high voltage, current is ramped down along the path G-H until a voltage lower than the lower threshold voltage V_{lt} is detected. The current ramp direction is reversed and the current is ramped up along the path C-D until it reaches the switching current of the branch 1 and the stack switches to a higher voltage value along the path E-F. When a junction voltage greater than V_{ut} is detected, a switch is registered. The current is ramped down once again so that junction voltage is just below V_{lt}, where the current is ramped up again to record another switch from branch 1. By making the repeated cycles a switching current histogram is built. A histogram of branch 1 is shown in Figure 3.22.

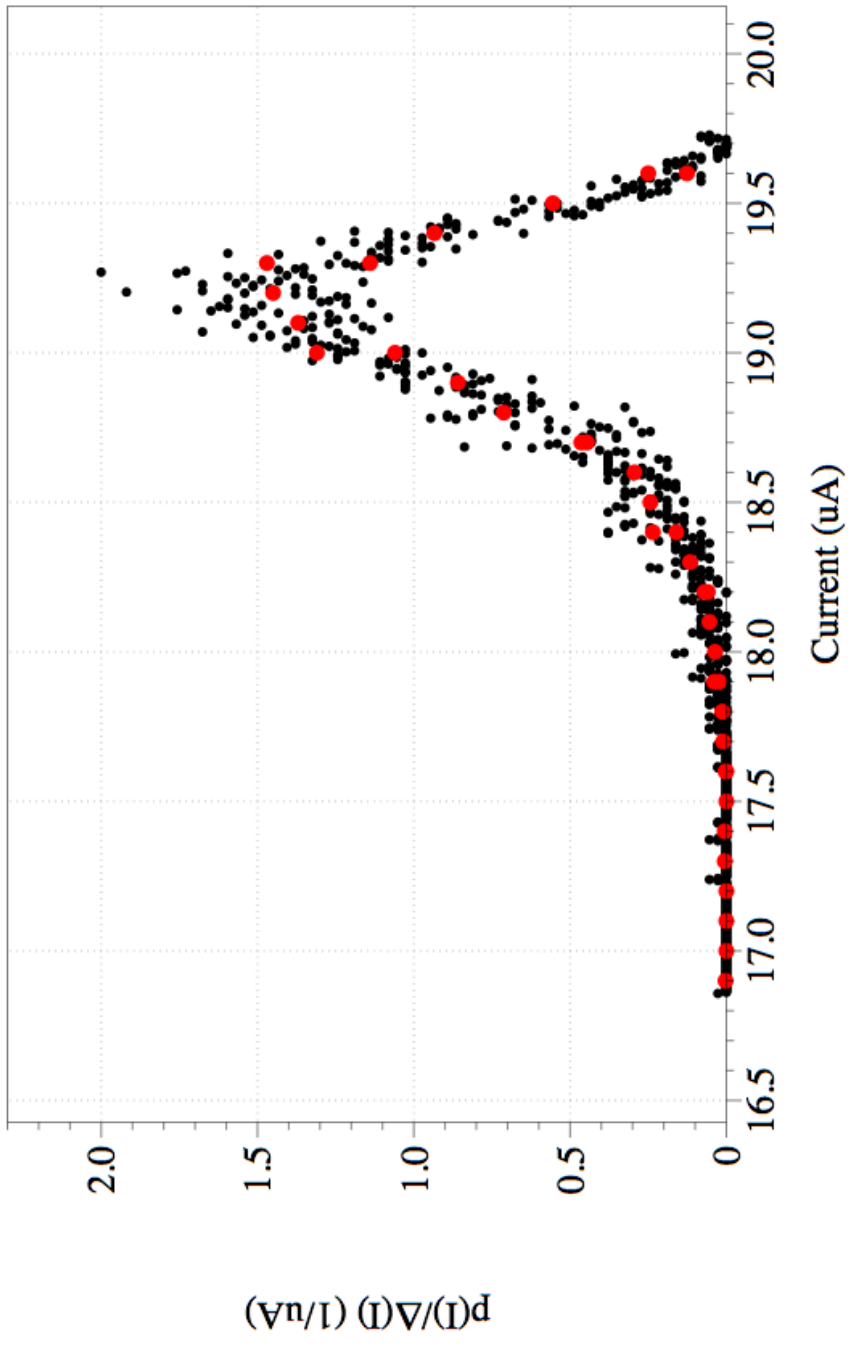

Figure 3.22: Switching current distribution histogram of branch 1 of Mk86-A3 at 6.04 K shows the switching current against the probability of switching within a bias current range I to $I+\Delta$I. Black points show the experimentally measured data with current resolution ΔI_{ADC} of 3.7 nA. Red points show the averaged data where the current bin size (ΔI) was 74 nA with 20 current bins.

The threshold voltages are set by two potentiometers connected to each comparator in LM319. The comparator output drives the SN74LS latch, which controls the analogue switch IC Max 333CP. This switches between two dc voltage levels, one for ramping the current up and the other for ramping it down. The selected voltage from the analogue switch Max 333CP is fed to a UA741CP which was configured as a buffer and then to the integrator. The output from the integrator was fed to the current source in the dip probe using a coaxial cable.

Chapter 4

Results and Analysis

4.1 Introduction

I present my findings and results in this chapter and start by establishing that the thin films are superconducting and the resistive transition temperature of the thin films is in accordance with previous results. The variation of T_c in various IJJ stack sites on the same thin film and between films is discussed. Salient features of the DC current voltage (IV) characteristics of the IJJ stacks are highlighted.

Switching current distributions from the zero-voltage branch, also known as the supercurrent branch or branch 0, and the first quasiparticle branch (branch 1) at various temperatures are presented. It is established that the switching distributions from these two branches are quite different from one another. It is also established that T^*, the temperature above which the behaviour of the junction changes from underdamped thermal activation to phase diffusion is higher for branch 1 as compared to branch 0. The higher T^* and the suppression of the switching current for branch 1 is explained in terms of the change in the dissipative environment of the IJJ stack when one junction switches to the voltage state.

Switching current measurements from branch 0 and branch 1 under the in-

fluence of RF irradiation are discussed in the following section. Suppression of the switching current of various branches is observed under the influence of RF irradiation. Switching current suppression of branch 0 is found to be strongest and suppression for the rest of the branches is very minimal. A flux-flow branch is observed at higher RF powers. The non-appearance of the flux-flow branch on the quasiparticle branches and suppression of the switching current of branch 0 is explained in terms of the environmental impedance.

The last section describes the resistive isolation of the IJJ stack from the environment. It outlines the objective for this isolation and the requirements for the resistors to be used. Typical parameters required for the resistors are calculated. Different geometries for placing the resistors on the chip are discussed and the criteria for the most suitable geometry is described. Results of the isolation and an analysis is presented. A final summary of the results concludes the chapter.

4.2 Critical Temperature

The critical temperature (T_c) of a superconductor is the temperature at which the resistance of the superconductor becomes zero. The transition temperatures in the ab plane of both a Tl2212 thin film and a Bi2212 single crystal were measured. The Tl2212 thin film was lithographically patterned using argon milling to create a track length of 40 μm and a width of 5 μm. The film thickness was 700 nm. The Bi-2212 single crystal was 3 mm long, 0.2 mm wide and 2 μm thick. Four point measurement of the dependence of the resistance on temperature in the ab plane for Tl2212 and Bi2212 samples are shown in Figure 4.1.

In the ab plane the resistivity shows a linear dependence upon temperature well above the transition temperature like a conventional metal. The resistivity starts to drop sharply at the onset of superconductivity and becomes zero at the transition temperature. The thin film sample has a T_c of 108 K. That of the Bi2212 single crystal is 88 K. The T_c value of 108 K for Tl2212 thin films is consistent with other group's measurements [Kang *et al.*, 1989; Kim *et al.*, 2003; Norton, 2004; Ozkan *et al.*, 1999]. A T_c value of 86.6 K has been reported for Bi2212 by Tachiki *et al.* [2003]. The in plane resistivity of the thin film is $\approx$ 300 $\mu\Omega$cm in the Tl2212 sample at room temperature. A resistivity value of 400 $\mu\Omega$m for thin films in ab plane has been reported by Kim *et al.* [2003].

The dependence of the c-axis resistance of a Bi2212 IJJ stack on temperature is shown in Figure 4.2. The Bi2212 stack is 1.5 μm long, 1 μm wide and 900 nm thick. Cutting, cleaving and mounting of the crystal on substrates and gold contact deposition for Bi2212 samples was done by myself; however FIB patterning and measurements for Bi-2212 samples were done by Johannes Leiner, a member of our research group. The c-axis transport is semi-conducting near the transition temperature; the resistance increases with decreasing temperature close to T_c. This difference in behaviour of the ab plane and c-axis values is known and has

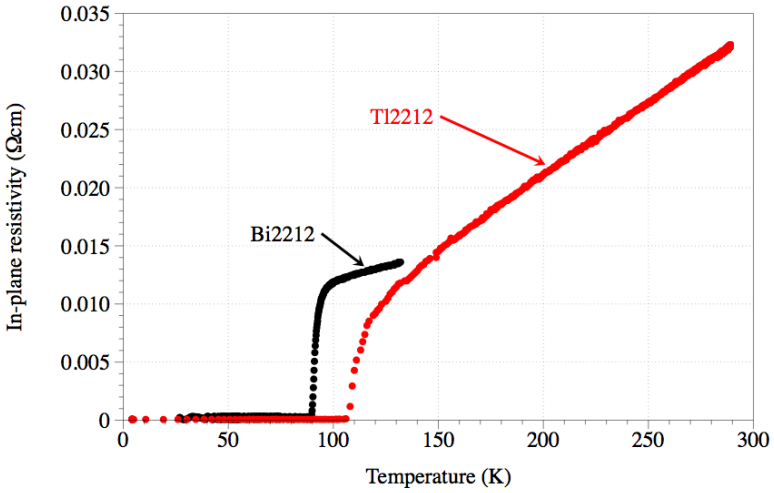

Figure 4.1: Dependence of the in-plane resistivity of a Tl2212 thin film (red points) and a Bi2212 single crystal (black points) on temperature. The T_c is 108 K (for the Tl-2212 thin film) and 88 K (for the Bi-2212 single crystal). The single crystal has a sharper resistive transition.

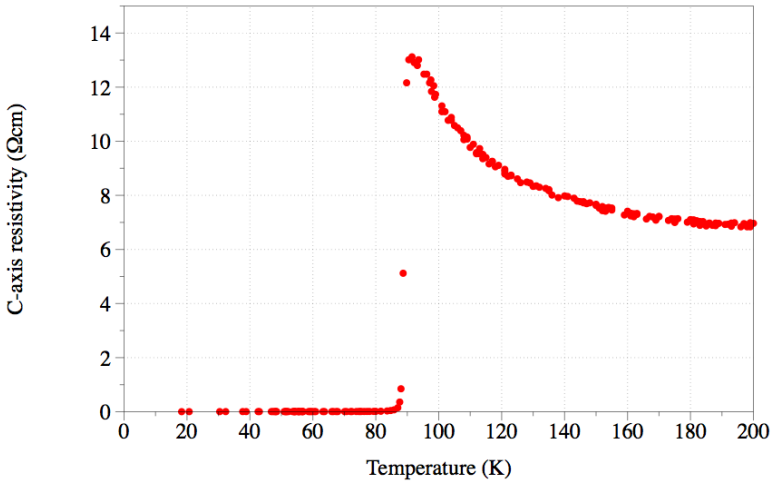

Figure 4.2: Dependence of the c-axis resistance of a Bi2212 junction stack on temperature.

been extensively studied [Ando *et al.*, 1996; Kim *et al.*, 2003; Kimura *et al.*, 1996; Martin *et al.*, 1988; Watanabe *et al.*, 1997; Yan *et al.*, 1995]. It is understood that metal like behaviour is observed due to the transport current flowing in the CuO_2 planes. In the c-axis direction the current is flowing perpendicular to the CuO_2 layers with insulating layers between them which cause the semiconducting behaviour. The c-axis resistivity of the Bi2212 sample is 13 Ωcm just above T_c and a similar value (16 Ωcm) has been measured by Tachiki *et al.* [2003]. Kim *et al.* [2003] measured the c-axis resistivity for a Tl2212 thin film to be 2.4 Ωcm. No c-axis data for Tl2212 IJJ stack was measured as c-axis measurement at room temperature destroyed the IJJ stack.

The width of the transition is a measure of the purity of the sample. The width of the resistive transition is broader for Tl2212 thin film as compared to the Bi2212 single crystal. The typical width of the broadening was found to be between 3 K and 5 K for Tl2212. A total of 18 IJJ stack sites are located on each thin film. The T_cs of various junction sites on the same thin film were found to be within 5 K of each other. The difference in T_c of IJJ stack sites on the same thin film can be due to local structural and chemical film imperfections. This difference in T_c of various IJJ stack sites did not significantly affect our experiments since they were made at a temperatures below $0.5T_c$.

4.3 Current Voltage (IV) Measurements

4.3.1 Conventional Switching Order

The electrical characteristics of FIB patterned IJJ stacks were measured in a four point configuration in liquid helium. Complete current voltage characteristics of an IJJ stack are shown in Figure 4.3. Only few branches are shown in the figure. The return branch corresponds to all IJJs in the voltage state.The low voltage region of a different IJJ stack is shown in Figure 4.4. Figure 4.4 shows only first three branches of the IJJ stack for clarity. The IV curves of the IJJ stack are multi branched, each branch corresponding to one, two, three, (etc) individual junctions switching to the quasiparticle state as the bias current exceeds the corresponding switching current.

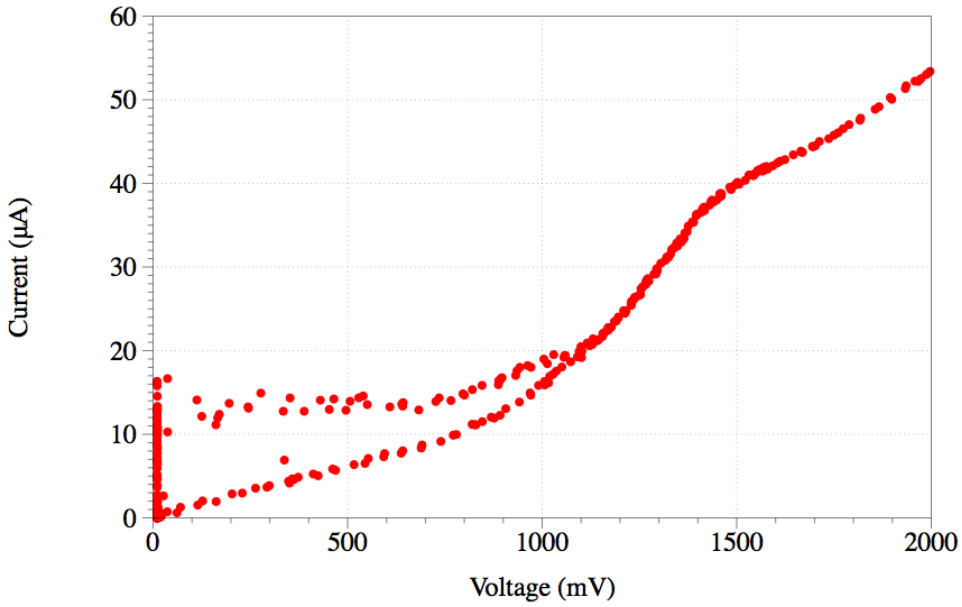

Figure 4.3: Complete IV characteristics of a Tl2212 IJJ stack at 4.2 K. Only a few branches are shown; return branch corresponds to to all IJJs in the voltage state.

The supercurrent branch is recorded when all the Josephson junctions are in the superconducting state. Once the biasing current exceeds the switching current of the junction with the smallest critical current, there is a discontinuous

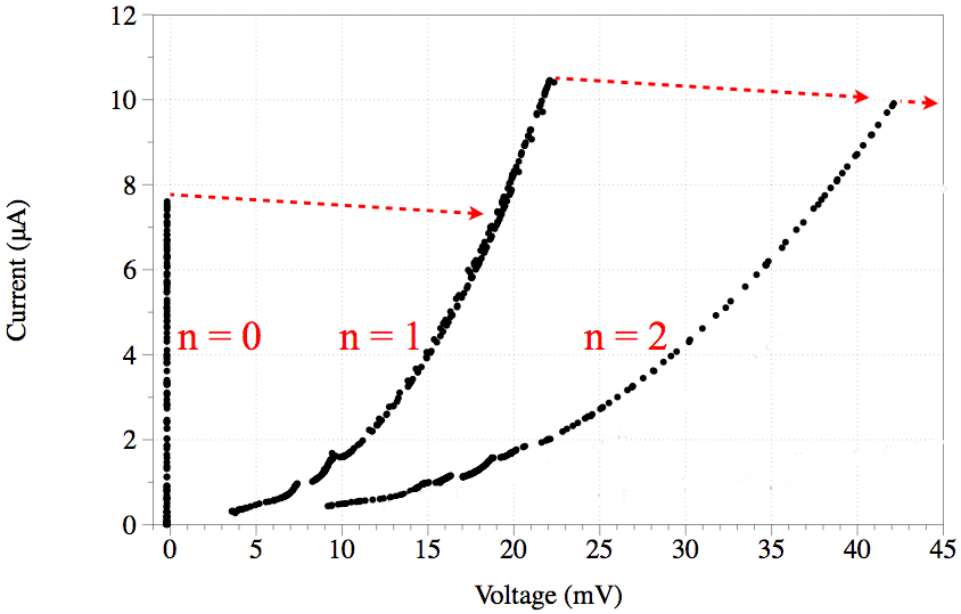

Figure 4.4: Low voltage region of IV characteristics of a Tl2212 IJJ stack at 4.2 K. Only the first three branches are shown here. Red arrows show the load line.

jump to the n=1 branch. The shapes of the resistive branches are similar to the IV characteristics of the small underdamped Josephson junction [McCumber, 1968]. The resistance of the branches increases with branch number at a fixed bias current. The curvature of the branches is explained by the V-shaped quasiparticle conductance observed in c-axis tunnelling experiments [Mandrus *et al.*, 1991]. Features present on quasiparticle branches at low voltage are termed phonon resonance and will be discussed in detail later in the chapter.

4.3.2 Current Voltage Characteristics with Anomalous Switching Order

Slightly different IV characteristics from those shown in Figure 4.4 were measured in a number of IJJ stacks. The individual junctions in these arrays were observed to switch from zero-voltage state (supercurrent branch) to the voltage state in an anomalous order, specifically the switch from the n=0 branch occurred at a significantly higher bias current than switches from other ($n \geq 1$) branches as

shown in Figure 4.5. As the switching current of supercurrent branch was higher than the rest of the branches, the switch from supercurrent branch did not happen to the closest branch i.e to branch 1. The switch from the supercurrent branch occurred to a higher voltage as shown by the arrow in Figure 4.6. This particular behaviour where the switch from the supercurrent branch apparently results in the simultaneous switching of several junctions we term Anomalous Switching Order (ASO). Similar behaviour has been observed previously by Kleiner *et al.* [1994]; Mros *et al.* [1998]; Warburton *et al.* [2003b]. Possible explanations of ASO will be discussed later in this chapter.

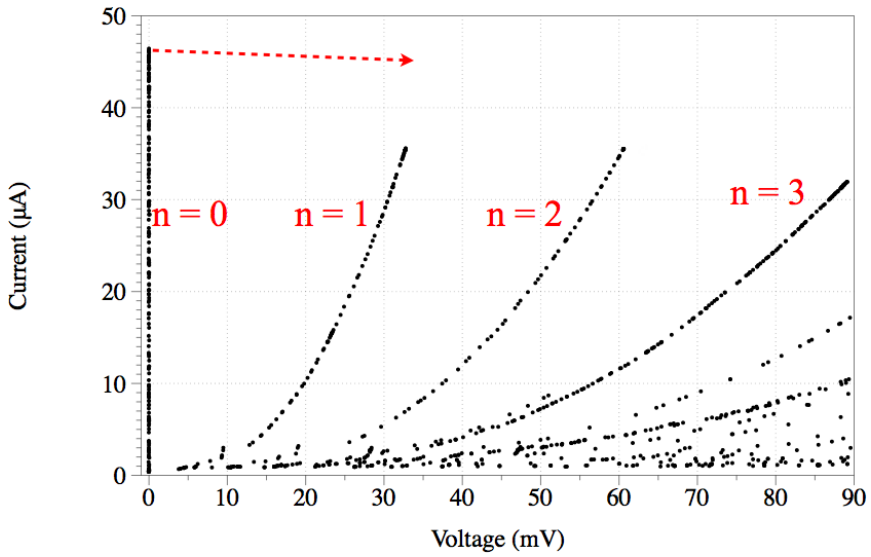

Figure 4.5: Low voltage region of IV characteristics of an Anomalous Switching Order (ASO) Tl2212, IJJ stack at 4.2 K.

4.3.3 Phonon Resonance

Each individual junction in an IJJ stack exhibits both a superconducting and resistive branch depending on the biasing current. In the low voltage region certain features are observed on the resistive branches, termed as subgap structures. These subgap structures have been observed previously by Schlenga *et al.* [1996, 1998]; Seidel *et al.* [1997]; Yurgens *et al.* [1996]. The IV characteristics of an IJJ

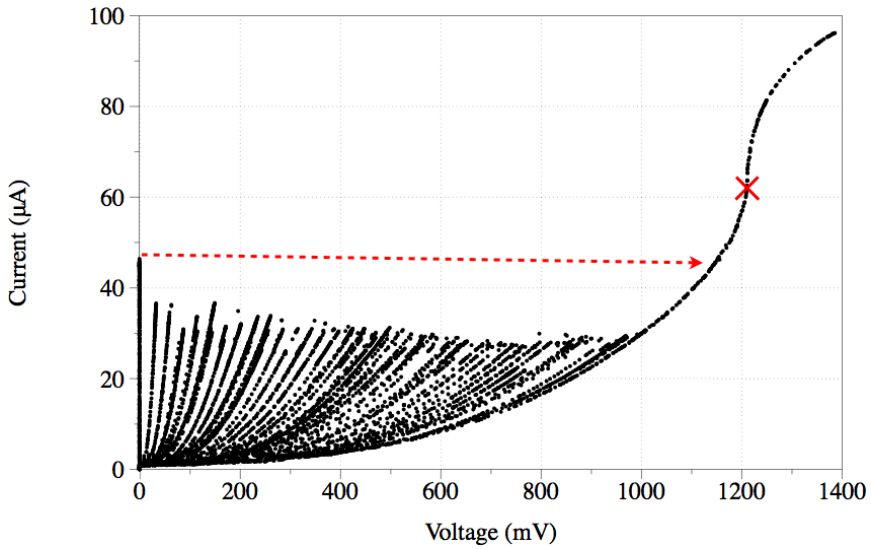

Figure 4.6: Complete IV characteristics of the Tl2212 ASO IJJ stack Mk56AD[1]-B6, shown in Figure 4.5. The switch from supercurrent branch happens along the dashed arrow to a higher voltage than to the first branch. The cross indicates the maximum value of dI/dV.

array showing particularly marked subgap structures are shown in Figure 4.7. Subgap structures appear at voltages V_1^1=7.5 mV and V_1^2=9.6 mV on the first quasiparticle branch. The subgap structure divides the quasiparticle branch IV in to three regions denoted as a, b and c. Depending on the number of junctions in the resistive state, i.e the branch number 'n', there are $2n$ hystereses in each region. Each hysteresis region contains 2n sub branches [Schlenga *et al.*, 1996]. The number of junctions in the resistive state can be ascertained by counting these sub branches or the hysteresis regions. V_n^i have the voltage value which is nth multiple of the V_1^i. Sub gap structures at similar values in Tl2223 were observed by Schlenga *et al.* [1996]. A detailed discussion of the sub gap structures and their dependence on sample geometry, number of resistive junctions, temperature, magnetic field both parallel and perpendicular to the layers, doping and microwaves is presented in Schlenga *et al.* [1998]

Subgap features are caused due to interaction between active optical c-axis phonons and oscillating Josephson currents. Active optical c-axis phonons can be

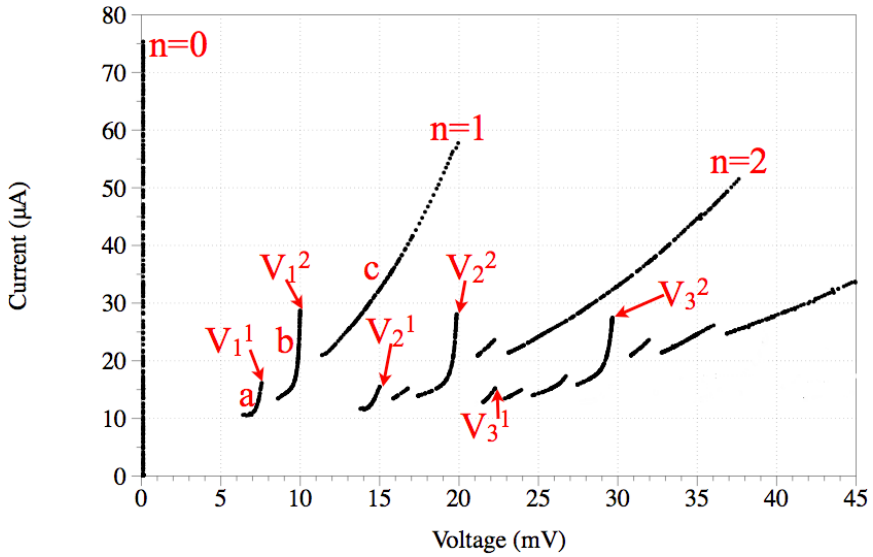

Figure 4.7: IV characteristics of a Tl2212 IJJ stack on expanded scale showing sub-gap structures at 4.2 K. V_n^i denotes the unique subgap feature where n is the branch number and i is the subgap number on that particular branch.

infrared [Helm *et al.*, 1997; Preis *et al.*, 2000] or Raman active optical phonons [Maksimov *et al.*, 1999]. This interaction leads to the appearance of current peaks on the IV characteristics when the voltage satisfies the condition $2eV = \hbar\omega_{ph}$ where ω_{ph} is the phonon frequency.

4.3.4 Self-Heating in IJJ IVs

The junction stack shown in Figure 4.6 has 42 branches. The total voltage for all branches where the hysteresis disappears is 1.0 V, which is consistent with 42 junctions at ≈ 25 mV each. The corresponding junction geometry is shown in Figure 4.8. The SEM picture shows an overlap thickness of approximately 240 nm. This thickness corresponds to about 160 junctions in series (neighbouring junctions are about 1.5 nm apart). The difference between the expected and observed number of branches might be due to the difference in the overlap area of junction on both sides of the track. Due to the 5°angle between the central track and the FIB beam during the drilling, there is a difference between the overlap area as observed by comparing Figure 4.8 and Figure 4.9. The actual overlap area is about 140 nm on the reverse side as opposed to 240 nm seen from the front of the structure. This height of 140 nm corresponds to 88 branches which is still significantly higher than the observed number of branches in the IVC. A possible reason for this could be self-heating due to which some branches can not be traced.

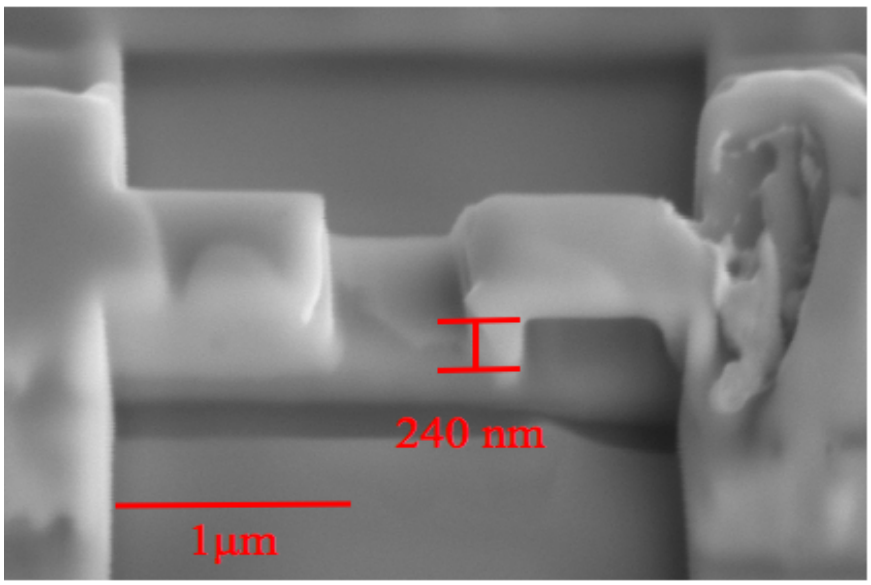

Figure 4.8: Mk56AD[1]-B6: SEM picture for the junction whose IV characteristics are shown in Figure 4.6. The overlap height is about 240 nm.

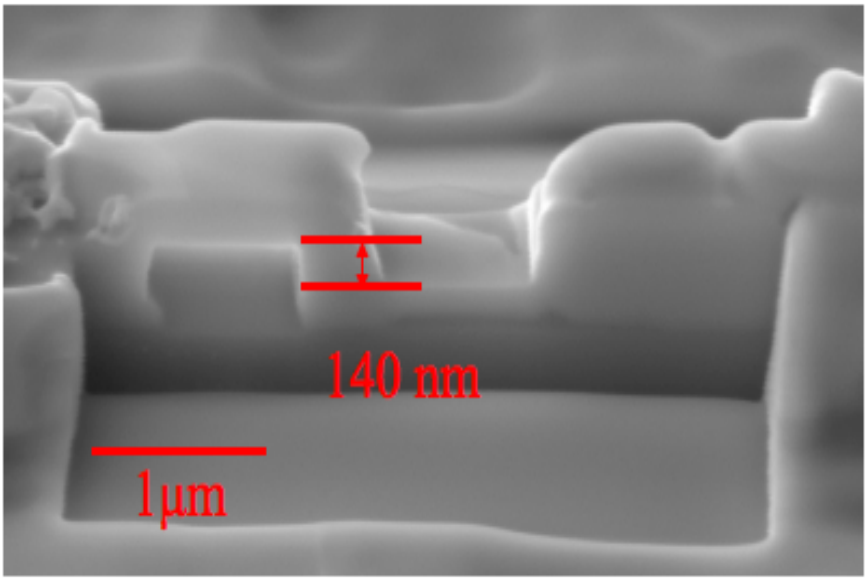

Figure 4.9: Mk56AD[1]-B6: Opposite side SEM picture for the junction whose IV characteristics are shown in Figure 4.6. The overlap height is about 140 nm, which is smaller than the height seen from the front of the junction structure.

If individual junctions in the stack are identical, then the quasiparticle branches will show uniform switching voltages in the absence of heating; at a fixed bias current the voltage on the nth branch is simply n times the voltage of the first branch. This is validated by comparing the first ten branches of the IV characteristics shown in Figure 4.10 and 4.11. Figure 4.10 shows the total voltage at a fixed bias current of 20 μA as a function of branch number. At first sight a uniform voltage spacing is observed indicating the absence of heating. The line shows a linear fit to the data from branch 2 to branch 10. The slope of the line is 23.8 mV/branch.

In Figure 4.11 we plot the current as a function of V/n, where n is the branch number. The curves for n=2,3....9 are qualitatively identical indicating that the individual junctions have similar tunnelling characteristics. In contrast to Figure 4.10, this graph does suggest the possibility of self-heating and gap suppression as the first quasiparticle branch has different characteristics from the other branches in the group. Power dissipated at top of branch one is about 1 μW and 2 μW

for branch two. Amount of self-heating is constant above 2 μW. The switching voltage of $\approx$ 30 mV is in agreement with the previously reported results [Inomata *et al.*, 2005; Jin *et al.*, 2006].

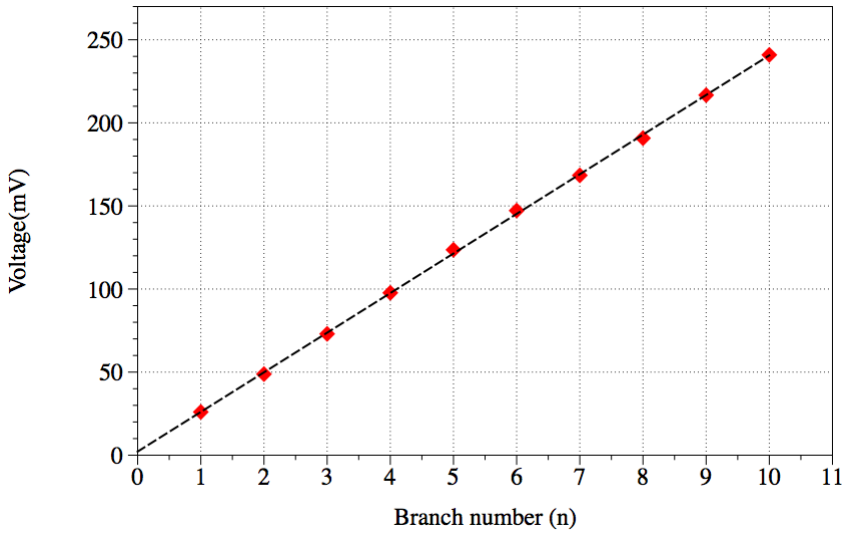

Figure 4.10: Voltage at 20 μA for the supercurrent branch and first ten quasiparticle branches of the IV characteristics of the sample Mk56AD[1]-B6, shown in Figure 4.5 at 4.2 K. The line is a linear fit to the data for branches 2 to 10. The slope of the line indicates the voltage difference between the branches.

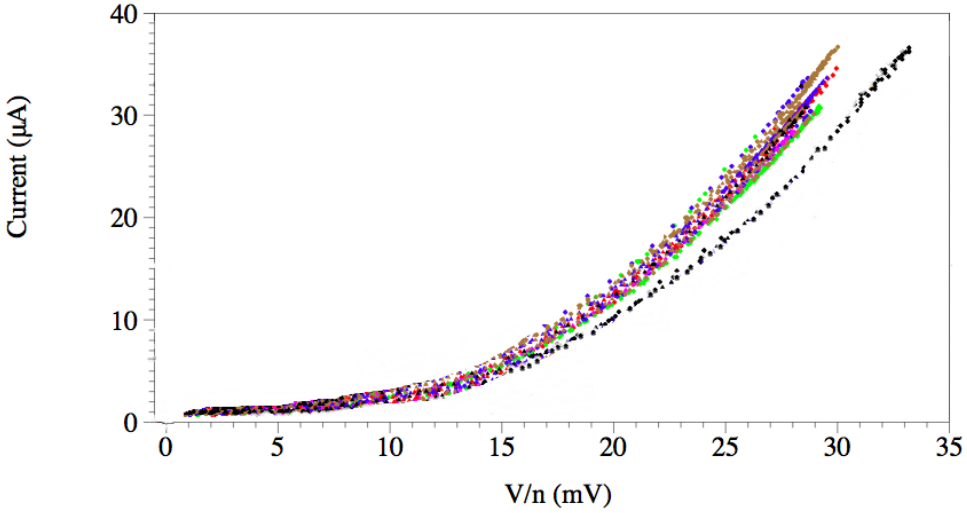

Figure 4.11: Comparison of the first ten quasiparticle branches of the IV characteristics of the sample Mk56AD[1]-B6, shown in Figure 4.5 at 4.2 K.

An apparent superconducting gap feature appears at 1211 mV as shown in

Figure 4.6. If this is a gap this would correspond to $V = 2N\Delta/e$ where N=42 is the number of branches. This gives 2Δ = 28.8 mV, similar to previously reported values [Moreland, 1989; Takeuchi *et al.*, 1989]. For 2Δ = 28.8 mV this gives I_cR_n=22.6 mV.

To investigate why the number of branches is lower than that predicted from the geometry, the same sample was measured again. Figure 4.12 shows two different IV measurements of the same junction stack two days apart. Comparison of both measurements shows that the switching current has reduced in the later measurement. Reason for reduction in switching current is not fully understood but may be attributed to some material change. This reduced switching current allows more number of branches to be traced. The number of branches has increased to 82 which is closer to the previous geometrical estimate of 88 branches. A change in the resistance of the stack is also evident. The resistance per junction has changed to 465 Ω and the new values of I_cR_n and 2Δ are 8.06 mV and 23.5 meV respectively. These measurements suggest that the maximum value of dI/dV can not be a gap feature.

In both measurements the hysteresis vanishes at approximately the same power dissipation ($\approx$ 30-35 μW); and the maximum dI/dV also occurs at the same power value ($\approx$ 70 μW) as shown by the constant power lines in Figure 4.12. Hysteresis in IJJs is temperature dependent. The hysteresis will vanish once the junction stack temperature has reached a particular value. This temperature value for Tl2212 thin films is approximately 55 K [Chana *et al.*, 1999]. I believe that in both measurements the stack temperature is raised to 55 K due to ohmic power dissipation. In the later measurement the power dissipated per branch is smaller than the former due to the reduced switching current. This allows more number of branches to be traced before the hysteresis vanishes. Dissipated power ($\approx$ 30-35 μW) and temperature (55 K), at which hysteresis vanishes are used to estimate the thermal resistance R_{th} of the sample ($\approx$ 2 K/μW).

4.3.5 Summary

This section described the general IVC of the IJJ stack including conventional and anomalous switching order. Fine features of the IVC like phonon resonances, only visible in high quality junctions were discussed. It has been established that IJJs suffer from self-heating. Self heating appears to be constant for $n \geq 2$. The value of superconducting energy gap Δ calculated from maximum value of dI/dV can not be used as a reference due to heating.

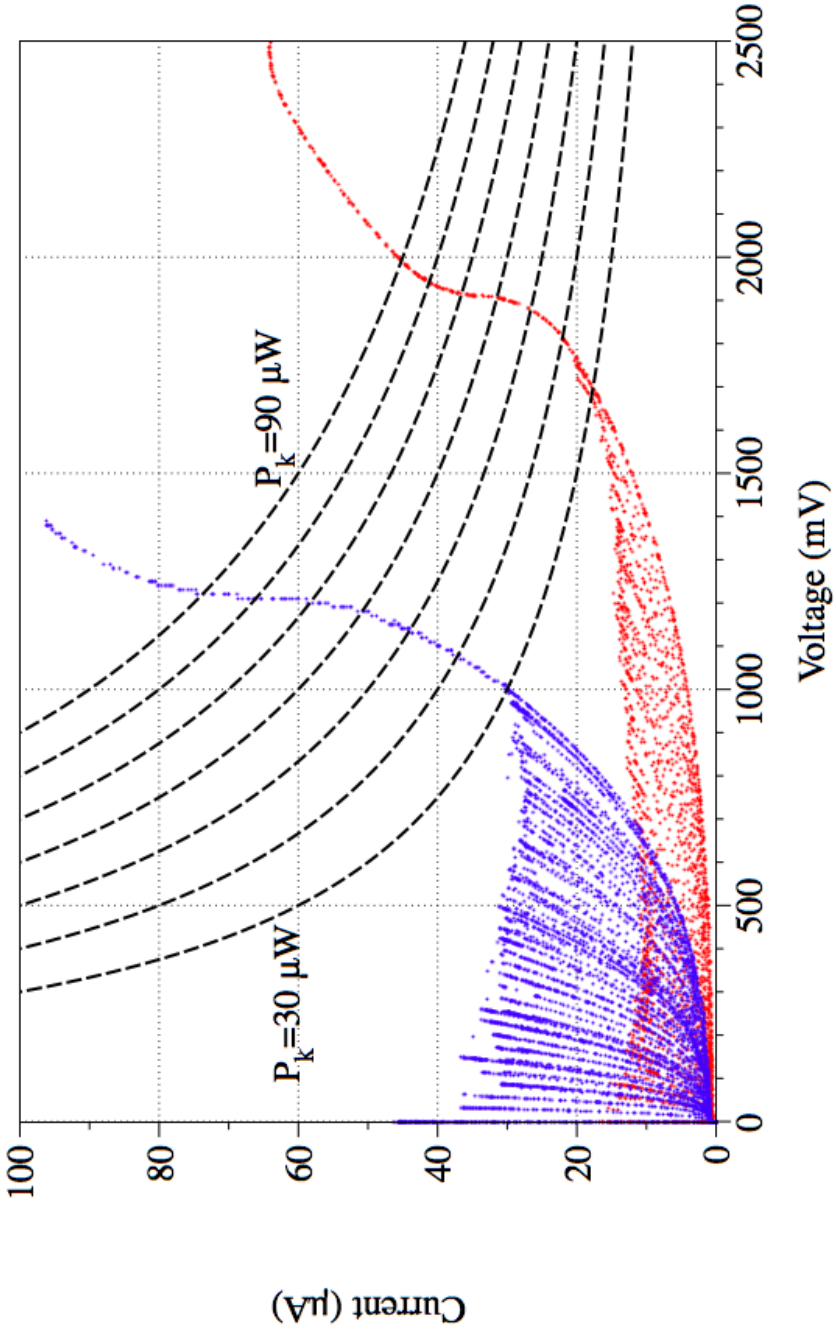

Figure 4.12: Change in IV characteristics of stack of IJJ at 4.2 K. Blue is the first measurement, red represents the same junction measured after two days. In the later measurement the switching current of all branches has increased. The lines of constant ohmic power dissipation are spaced by 10 μW.

4.4 Temperature Dependent Switching Current Distribution Measurements

4.4.1 Overview

A total of five IJJ stacks were measured to study the switching measurements from the individual branches. A list of the samples studied is shown in Figure 4.13. All the samples had an active junction area of less than one micron. Figures 4.14 and 4.15 show the IV characteristics of the IJJ stacks MK86-A2 and MK86-A3 respectively. Both the samples show uniform switching voltage between the branches. The switching voltage of 20 to 25 mV is in agreement with the previously reported results [Inomata *et al.*, 2005; Jin *et al.*, 2006].

Sample	Size (μm^2)	Branches
Mk56AD[I]-A3	0.37	0 & 1
Mk86-A2	0.23	0 & 1
Mk86-A3	0.24	0,1,2 & 3
Mk87-A8	0.3	0 & 1
Mk87-B6	0.3	0 & 1

Figure 4.13: Samples used to study the temperature dependent switching from an IJJ stacks. All junction stacks have an active area of less than one micron.

4.4.2 Current control comparison

In both the samples shown in Figure 4.14 and 4.15 we observe the anomalous switching order (ASO) i.e for $n \geq 1$ (n is the branch number) the current, I_n at which switching from branch n to n+1 occurs is less than the switching current

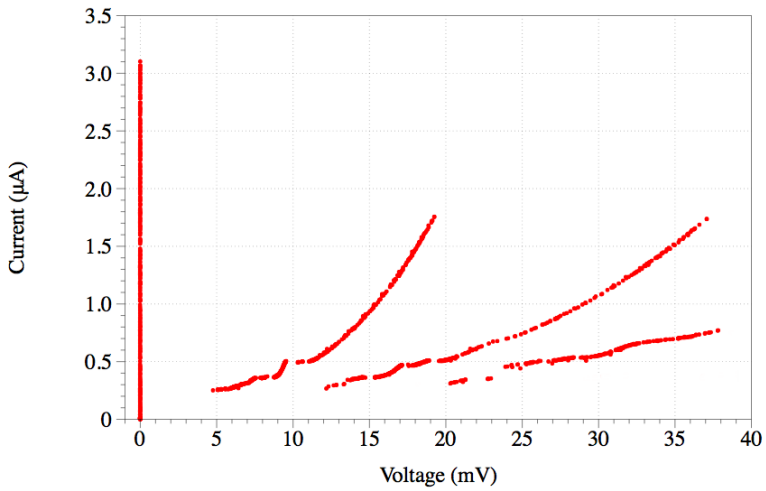

Figure 4.14: IV characteristics of Tl2212 sample MK86-A2 at 4.2 K. Only the first four branches are shown.

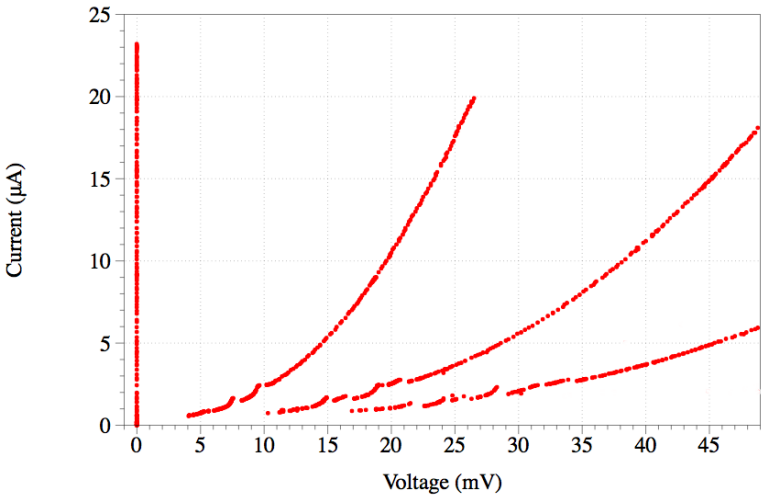

Figure 4.15: IV characteristics of Tl2212 sample MK86-A3 at 4.2 K. Only the first four branches are shown.

of zero-voltage branch. We cannot use the triangular wave to measure switching current distributions from quasiparticle branches under ASO. We designed a custom-built current ramp control with automatic direction control, which has been described in the previous chapter (section 3.3.4). This current control allowed us to measure the SCD from quasiparticle branches in ASO IJJs.

In order to ensure that the custom-built current control was suitable to measure switching current measurements from quasiparticle branches, it was compared with the existing current controls. The only branch all three current controls could measure was branch 0 of an IJJ stack. In order to make this comparison the switching current distributions from the zero-voltage branch of Mk-56AD[I]-A3 were measured using custom-built current control along with a commercial function generator and a dc triangular waveform generator (this cannot be used to measure the SCD from quasiparticle branches). The results of these measurements are shown in Figure 4.16. The escape rate from all three SCD was extracted using Equation 2.22. The corresponding plots of the escape rate as a function of biasing current shown in Figure 4.17, showing that the three current controls give identical results. Hence, with the additional inbuilt ramp direction controls, the new current control can be used for measuring SCDs from quasiparticle branches.

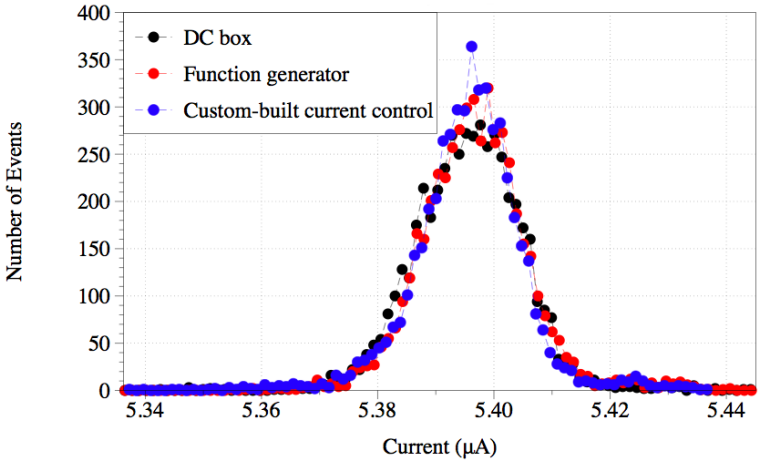

Figure 4.16: Switching current distribution measured from branch 0 of sample Mk56AD[I]-A3 using three different current controls at 5 K. All three distributions have similar data values suggesting the feasibility of the custom-built current control (blue data points) to be used for measuring the switching distributions from quasiparticle branches. The ramp rate during the three measurements was 0.3 mA/S.

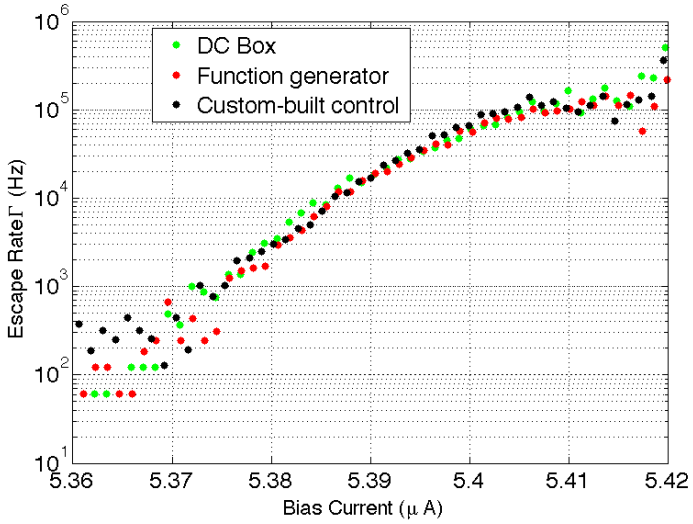

Figure 4.17: Escape rate as a function of biasing current for the three SCD (shown in Figure 4.16) measured with three different current controls at 5 K. Similar values of escape rate establish the credibility of the custom-built current source to be used for measuring SCD from quasiparticle branches.

4.4.3 SCD of branch zero and branch one - Observations

Switching current distributions, $P(I)$ for switching from both the $n = 0$ and the $n = 1$ branches were performed on both Mk86-A2 and Mk86-A3. The ramp rate for switching distributions measurements was 1.4 ± 0.1 mA/s for Mk86-A3 and 0.4 ± 0.1 mA/s for MK86-A2. Both MK86-A3 and Mk86-A2 have the same area of 0.24 μm^2. Each switching current distribution measurement comprised of 5000 points for Mk86-A3 and 3000 points for Mk86-A2 (at each temperature) in order to create the switching current histogram. The resolution, ΔI_{ADC}, of the analogue-to-digital converter for the measurement was 3.7 nA. Switching current distributions from branch 0 and 1 at various temperatures for MK86-A3 are shown in Figure 4.18.

If we compare the distributions for the two branches (n=0 and n=1) at any particular temperature (e.g at T_{bath}=26.1 K) as shown in Figure 4.19, it is observed that the mean value of I_0 (14.0 μA) is larger than that of I_1 (12.1 μA) and also the standard deviation of I_0 (0.15 μA) is smaller than that of I_1 (0.53 μA). This establishes the fact that the two junctions, junction A (the first junction to switch to resistive state) and junction B (the second junction to switch to resistive state) behave differently in a dynamical sense. In Figure 4.20 the switching current I_{sw} of the supercurrent (n=0) branch is higher than the first quasiparticle branch (n=1), establishing ASO for $T > 20$ K.

Switching current distributions $P(I)$ for branch 0 (zero-voltage branch) and branch 1 (1st quasiparticle branch) were measured from 4.2 K to 50 K for Mk86-A3 and from 4.2 K to 18 K for Mk86-A2. Figures 4.20 and 4.21 show the temperature dependence of the mean and standard deviation, σ, raised to the power three-halves for both samples. The behaviour of $\sigma^{3/2}$ can be divided into two temperature regions: (i) the temperature region where $\sigma(T)$ increases proportional to $T^{2/3}$ (ii) the temperature region where $\sigma(T)$ decreases as the temperature increases. Based on the results of Krasnov *et al.* [2005b]; Li *et al.* [2007] and others

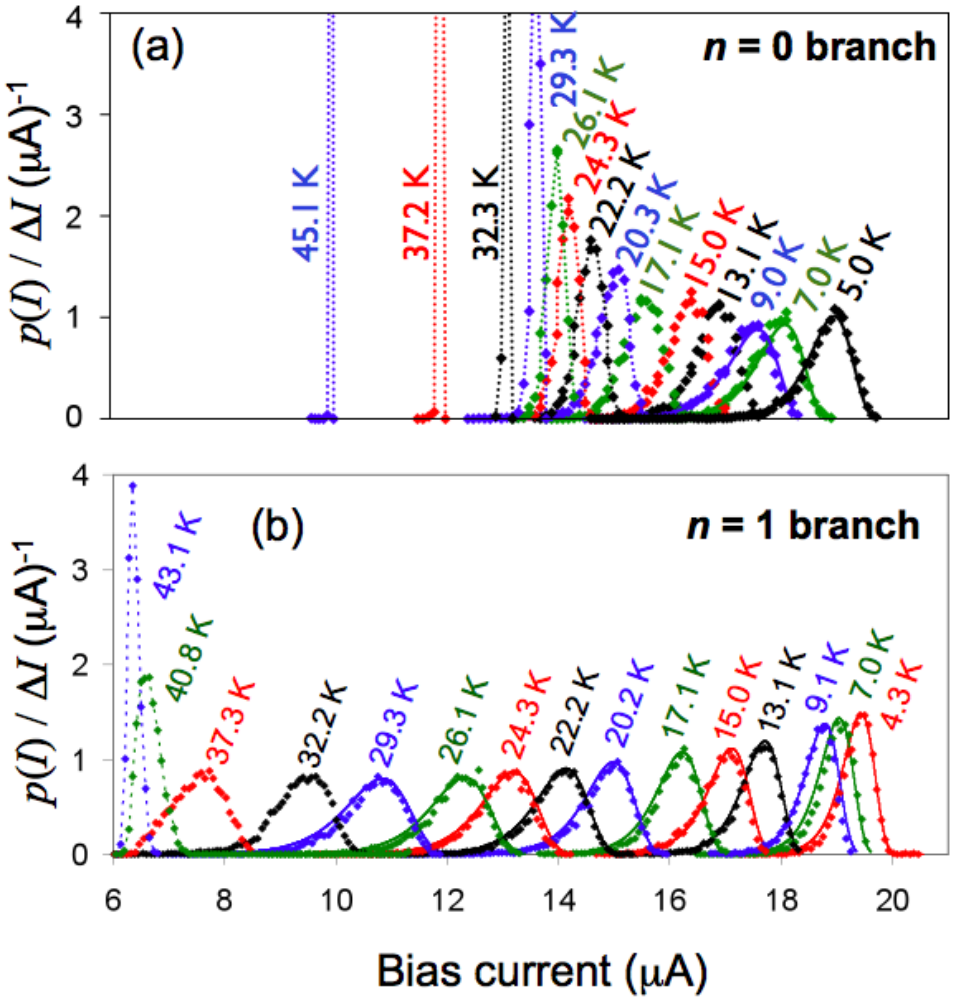

Figure 4.18: Switching current distributions for (a) the $n = 0$ and (b) the $n = 1$ branches of MK86-A3. The points show the experimentally measured values at the indicated bath temperature. $P(I)$ is the probability of switching within a bias current range I to $I + \Delta I$, where ΔI is 74 nA ($\Delta I = 20\Delta I_{ADC}$). Solid lines in (a) for 4.3 K $< T_{bath} <$ 9.0 K and (b) for 4.3 K $< T_{bath} <$ 29.3 K are fits to the Kramers thermal activation model in the limit of negligible damping for a critical current of 30.0 μA for (a) and 27 μA for (b), with the effective temperature being the fitting parameter. Dashed lines are guides to the eye.

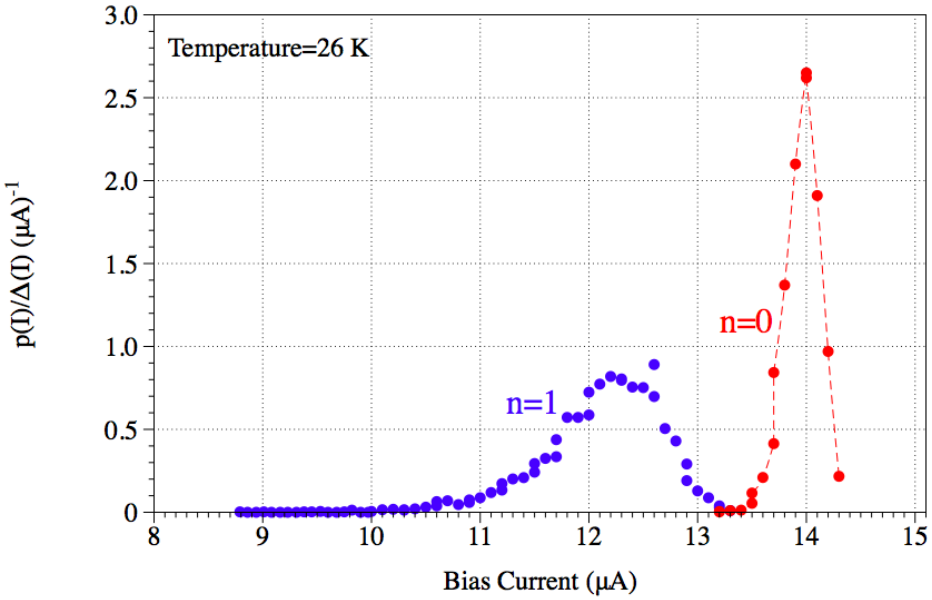

Figure 4.19: Switching current distributions for $n = 0$ and $n = 1$ branches of MK86-A3 at 26 K. The red line is a guide to the eye.

we can term the region (i) as the underdamped thermal activation (UTAD) region and region (ii) as the phase diffusion region. The crossover temperature from UTAD to phase diffusion is denoted by T_0^* for branch 0 and by T_1^* for branch 1.

The change from UTAD to phase diffusion i.e T^* for Mk86-A3 occurs at 9 K for branch 0 and at 29 K for branch 1. T^* for branch 1 of Mk86-A2 occurs at about 8 K and we do not see any change from UTAD to phase diffusion for branch 0 of Mk86-A2, suggesting that the T^* for branch 0 of Mk86-A2 is less than 4.2 K i.e. **in both Mk86-A3 and Mk86-A2, T^* for branch 1 is higher than the T^* of branch 0**. In Figure 4.20(b) the zero distribution width for branch 1, $\sigma^{3/2}$, extrapolates to $T_{bath} = -10$ K suggesting significant heating. Conversely branch 1 of Mk86-A2 does not show any apparent heating and extrapolates close to zero as shown by dashed line in Figure 4.21. The IJJ stacks in both MK86-A2 and A3 are essentially identical, however, the current density is found to be much smaller in A2 (1300 A/cm^2 compared to 9500 A/cm^2 for MK86-A3). The reasons for this change in current density are not known but are presumably can be defect

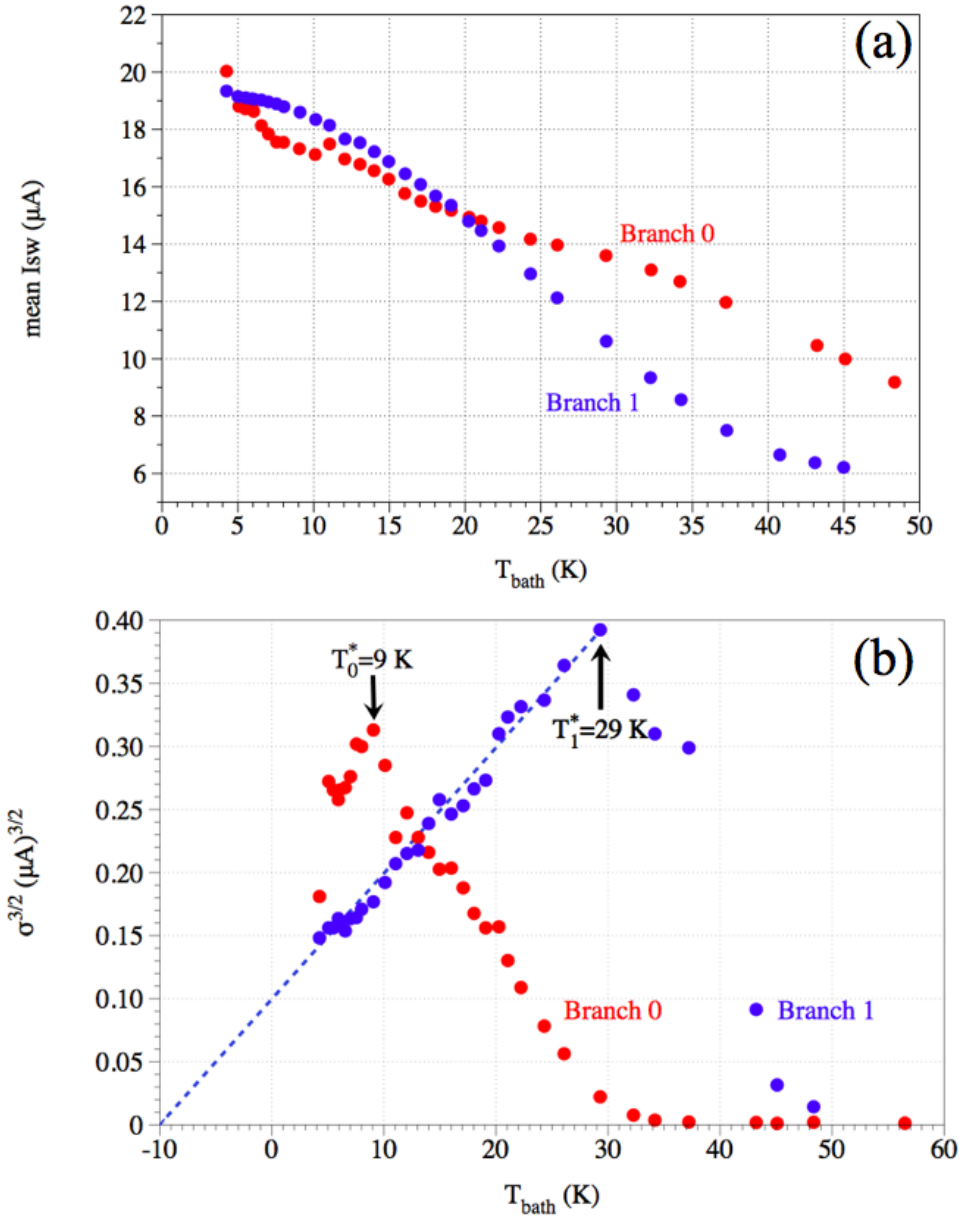

Figure 4.20: The bath-temperature-dependence of (a) the mean and (b) the standard deviation, σ, raised to the power of 3/2 of the switching current distributions for MK86-A3, shown in Figure 4.18. The red and blue points are the experimental data for branches $n = 0$ and $n = 1$ respectively. Note that T_1^* for branch one has a higher value of 29 K as compared to 9 K for T_0^*. Negative $d\sigma/dT$ is a hallmark of phase diffusion. Broken line is the linear fit to σ of branch 1. SCD of branch 1 extrapolates to $T \approx$-10 K, suggesting apparent heating on branch 1.

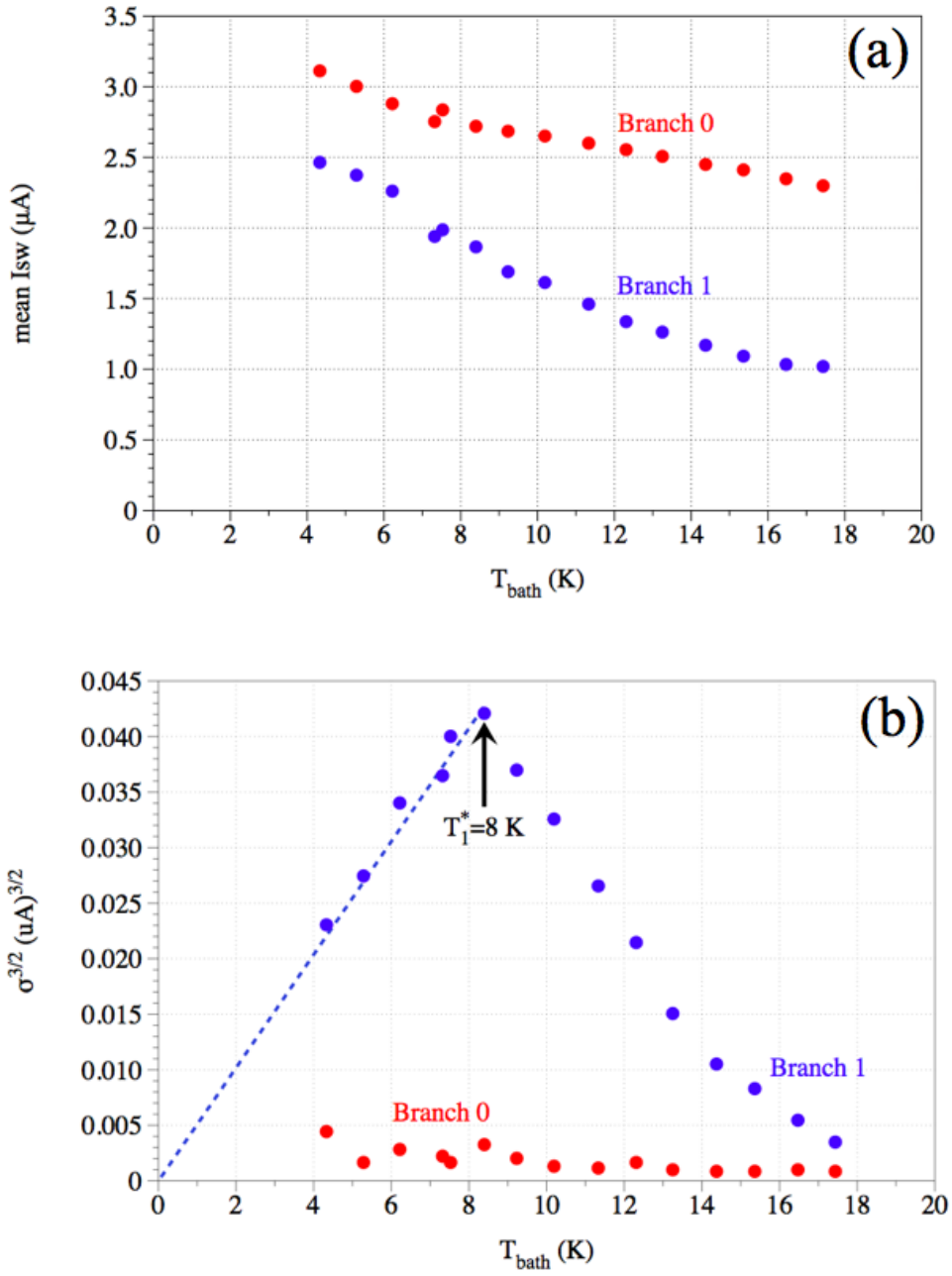

Figure 4.21: The bath-temperature-dependence of (a) the mean and (b) the standard deviation, σ, raised to the power of 3/2 for the junction IVC MK86-A2, shown in Figure 4.14. The red and blue points are the experimental data for branches $n = 0$ and $n = 1$ respectively. Note that T_1^* for branch one has value of 8 K and no T_0^* was observed. Negative $d\sigma/dT$ is a hallmark of phase diffusion. Broken line is the linear fit to $\sigma^{3/2}$ of branch 1. SCD of branch 1 extrapolates to zero indicating the apparent absence of heating.

related.

The results from the temperature dependent SCD measurements are (i) higher switching current for supercurrent branch than first quasiparticle branch in some temperature range (ii) SCD width σ scales proportional to $T^{2/3}$ for UTAD (iii) negative $d\sigma/dT$ in the phase diffusion regime (iv) a higher T^* for branch one than branch zero and (v) apparent heating for the junction stack with a larger current density.

4.4.4 SCD of branch zero and branch one - Analysis

This section will look at various possible explanations of ASO. These explanations include heating, suppression of the first quasiparticle branch switching current due to the A.C. Josephson effect and a change in the dissipative environment of the IJJ stack.

4.4.4.1 ASO caused by Heating

One possible cause of ASO can be self-heating of the IJJ stack. Self-heating can reduce the switching current of the Josephson junction. Self-heating can be estimated by comparing the experimental SCD with the standard model of thermal activation in UTAD regime. Matlab code for the standard model of thermal activation was written by Dr J. C. Fenton with some modifications by me. The input parameters for the simulation are the bias current ramp rate and the junction capacitance. The program performs a two parameter fit to the experimental data where both the effective temperature and the unfluctuated critical current are used as fitting parameters. It generates a number of theoretical curves $P(I)$ using Equation 2.18 with different values of effective temperature and critical current, comparing each theoretical curve with the experimental data. The critical current and temperature value which results in the minimum error between the experimental and theoretical data are reported as the fit parameters for the experimental SCD. It is also possible to perform a single parameter fit by fixing either the effective temperature or the critical current at the particular value.

The simulation code described was used to perform a two parameter fit on the n=0 branch shown in Figure 4.18. $P(I)$ data from Mk86-A3 branch 0 was fitted to the standard model of thermal activation as applied to a single Josephson junction [Fulton & Dunkleberger, 1974] (see section 2.6.1.1). The capacitance, C of the junction was calculated using an estimate of 6 $\mu F/cm^2$ for the specific capacitance

[Warburton *et al.*, 2004]. The extracted critical current and extracted effective temperature as a function of bath temperature for the n=0 branch (red data points) for $T_{bath} < T_0^*$ are shown in Figure 4.22. It is observed that the switching distributions for I_0 are very much broader than predicted by the standard thermal activation model. Although the simulation gives a good visual fit as shown in Figure 4.18, the fit temperature is significantly higher than the bath temperature.

Possible explanations for this deviation include MQT, Ohmic heating and the presence of Josephson fluxons. The crossover temperature from UTAD to MQT can be calculated using $\hbar\omega_p/2\pi k_B$. Using a critical current of 29 μA, the plasma frequency is calculated as 395 GHz. This gives a crossover temperature of $\approx$ 3.0 K, which is much smaller than the observed value of 15 K. This proves that the temperature independent behaviour in this graph is not caused by MQT. Self-heating on branch zero can be ruled out due to the absence of any voltage on the supercurrent branch. Josephson fluxons make the experimentally measured $P(I)$ distribution wider, compared to the theoretical $P(I)$ obtained from the standard thermal activation model for the same value of peak switching current. The wider experimental $P(I)$ distribution (with same peak switching current as that of theoretical distribution) provides a higher effective temperature as shown in Figure 4.18. We therefore conclude that the high effective temperature can be only explained by the presence of Josephson fluxons in the IJJ stack [Mros *et al.*, 1998; Warburton *et al.*, 2004].

Branch 1 cannot be measured in the absence of self-heating since there is certainly some dissipation (of order hundreds of nW) resulting from junction A being in the voltage state. In order to establish an upper bound on the Ohmic self-heating on the $n = 1$ branch $P(I)$ data from Mk86-A3 branch 1 was fitted to the standard model of thermal activation using a two parameter fit. The extracted critical current and extracted effective temperature as a function of bath temperature for the n=1 branch for $T_{bath} < T_1^*$ are shown in Figure 4.22

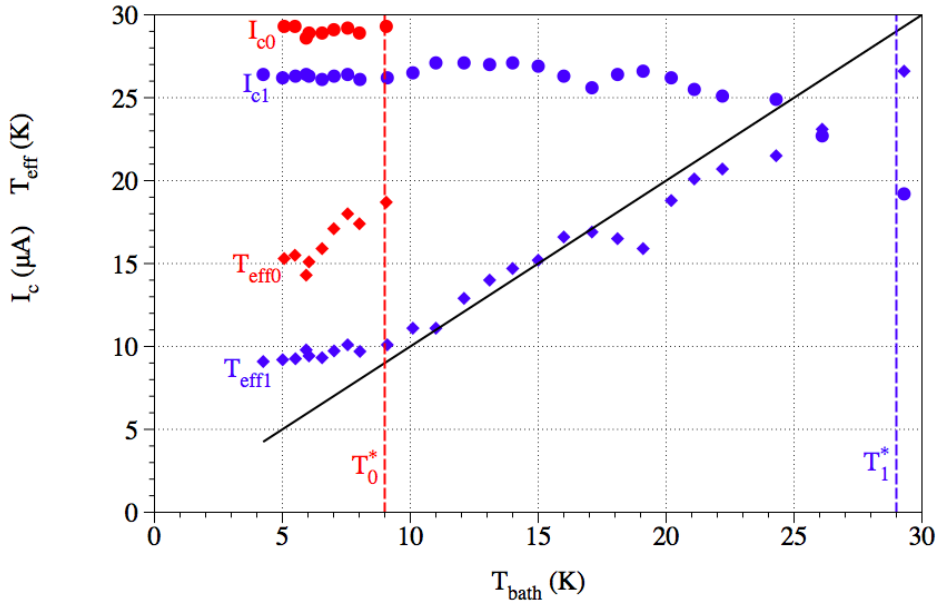

Figure 4.22: The bath temperature dependence of the extracted critical current I_c and extracted fit temperature (T_{eff}) for n=0 and n=1 branch. The black line is $T_{eff} = T_{bath}$.

(blue data points). The average value of the critical current (I_{cB}) obtained from fitting is 27 μA. The extracted temperature T_{eff1} is about 5 K higher than the bath temperature at T_{bath}=4.2 K.

This deviation could also be caused by MQT, self-heating or the presence of fluxons. One might argue that this temperature independent behaviour below 11 K is due to the onset of MQT. The crossover temperature from UTAD to MQT can be calculated using $\hbar\omega_p/2\pi k_B$. Using a critical current of 27 μA, the plasma frequency is calculated as 381 GHz. This gives a crossover temperature of $\approx$ 2.9 K, which is much smaller than the observed value of 9 K. This proves that the approximately temperature-independent behaviour for branch one in this graph is not caused by MQT. Another reason for this behaviour could be Josephson fluxons. Comparison of T_{eff0} and T_{eff1} shows that T_{eff1} is almost independent of T_{bath} in contrast to T_{eff0}. This suggests that the T_{bath} independent behaviour of T_{eff1} is not caused by thermally-activated Josephson fluxons. The most probable cause for the temperature independent behaviour on branch one at $T_{bath} < 10$ K

is therefore self-heating due to one junction being in voltage state.

The extracted fits in Figure 4.22 were obtained by a two parameter fit. Uncertainties in the fitting procedure result in $T_{eff1} < T_{bath}$ at some bath temperatures which is not possible. To address this problem a fixed value of I_{c0} (27 μA) was used (consistent with the Ambegaokar-Baratoff model) and T_{eff} is extracted using a one parameter fit. Figure 4.23 shows the T_{bath}-dependence of the T_{eff} of branch 1 of Mk86-A3 by fitting to the $P(I)$ for each temperature ($P(I)s$ are shown in Figure 4.18). In our results for branch 1, in the temperature range 11 K $< T_{bath} <$ 29 K, the determined effective temperature is within 1 K of the bath temperature. For $T_{bath} <$ 11 K there is an increasing amount of self-heating as the bath temperature is lowered, although the fits to the distribution as shown in Figure 4.18 are still good provided $T_{eff} > T_{bath}$ is used. Thus the degree of ohmic self-heating in the 11 K to 29 K range for branch 1 of Mk86A-A3 is less than 1 K.

The degree of self-heating can be used to extract the thermal resistance as shown in Figure 4.24. ΔT is obtained by subtracting the bath temperature from effective temperature. It is seen that, at low temperature the thermal resistance decreases with increasing T_{bath} and flattens out at higher temperatures. Qualitatively similar results have been reported by Krasnov *et al.* [2005c] for Bi2212 as shown in Figure 4.25. The thermal resistance in my sample is however three orders of magnitude higher than that reported for Bi2212 by Krasnov *et al.* [2005c]. This difference is due to the fact that Krasnov *et al.* use a bigger mesa structure with a cross sectional area of 10 μm^2.

Self heating on branch 0 should ideally be zero. In some cases a very small voltage due to incoherent phase slips may be present. This incoherent phase slip voltage is less than the voltage noise (1.0 μV r.m.s calculated from supercurrent branch). Thus the power dissipated on the n=0 branch is at least four orders of magnitude smaller than the power dissipated on the n=1 branch. It is safely

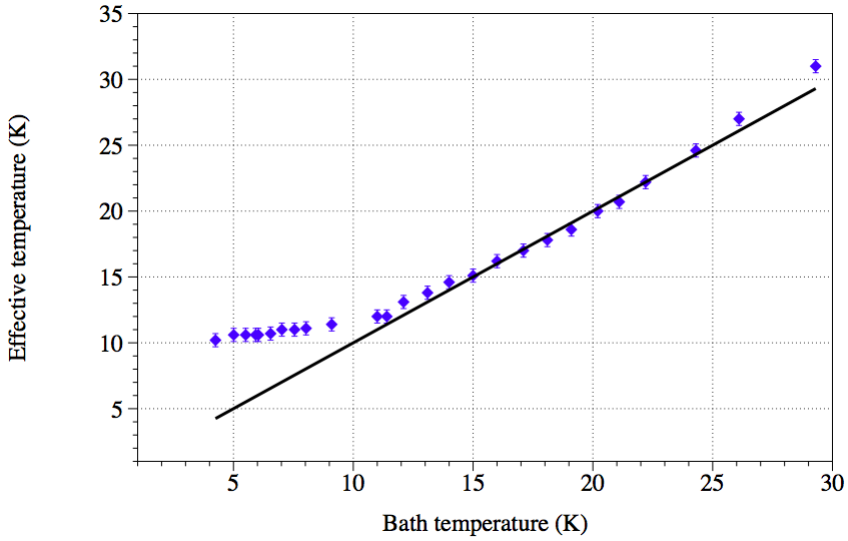

Figure 4.23: The bath-temperature-dependence of the effective temperature extracted from the fits to the switching current distributions for the $n = 1$ branch of MK86-A3 shown in Figure 4.18. The solid line shows $T_{eff} = T_{bath}$. The values of I_c and C were kept constant throughout the entire temperature range.

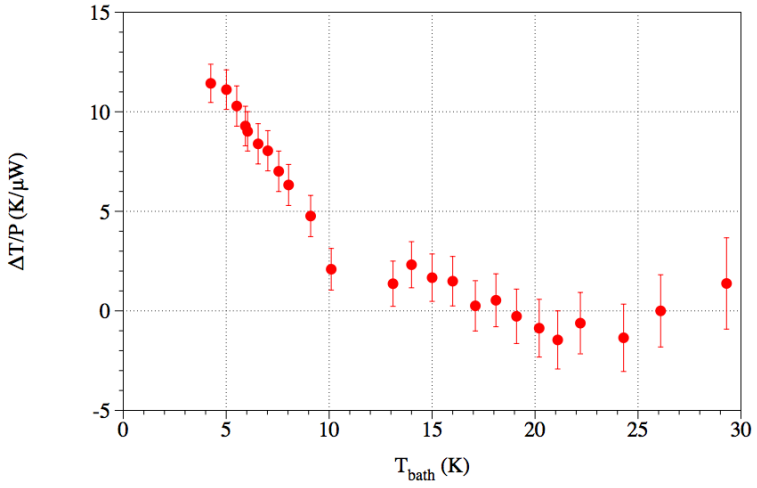

Figure 4.24: Thermal resistance for n=1 branch of MK86-A3 as a function of bath temperature. ΔT is the difference between effective temperature and bath temperature shown in Figure 4.23. P is the electrical power dissipated at the top of n=1 branch.

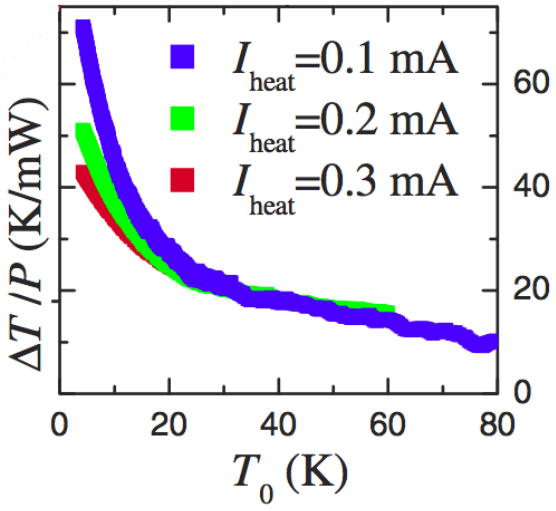

Figure 4.25: Self-heating in a Bi2212 mesa structure with cross sectional area of 10 μm^2. Figure from Krasnov *et al.* [2005c].

concluded that both the n=0 and n=1 branches are negligibly affected by self-heating in the 11 K to 29 K range.

In Figure 4.26 the bath temperature dependence of the mean and the standard deviation of the distributions of I_0 and I_1 of Mk86-A3 are re-plotted. For $T_{bath} > 20$ K the mean value of I_0 exceeds that of I_1 (i.e. the switching order is anomalous), and the degree of self-heating is negligible at least in the range 20 K $< T_{bath} <$ 29 K. In this temperature range the standard deviation of I_0 is also significantly lower than that of I_1.

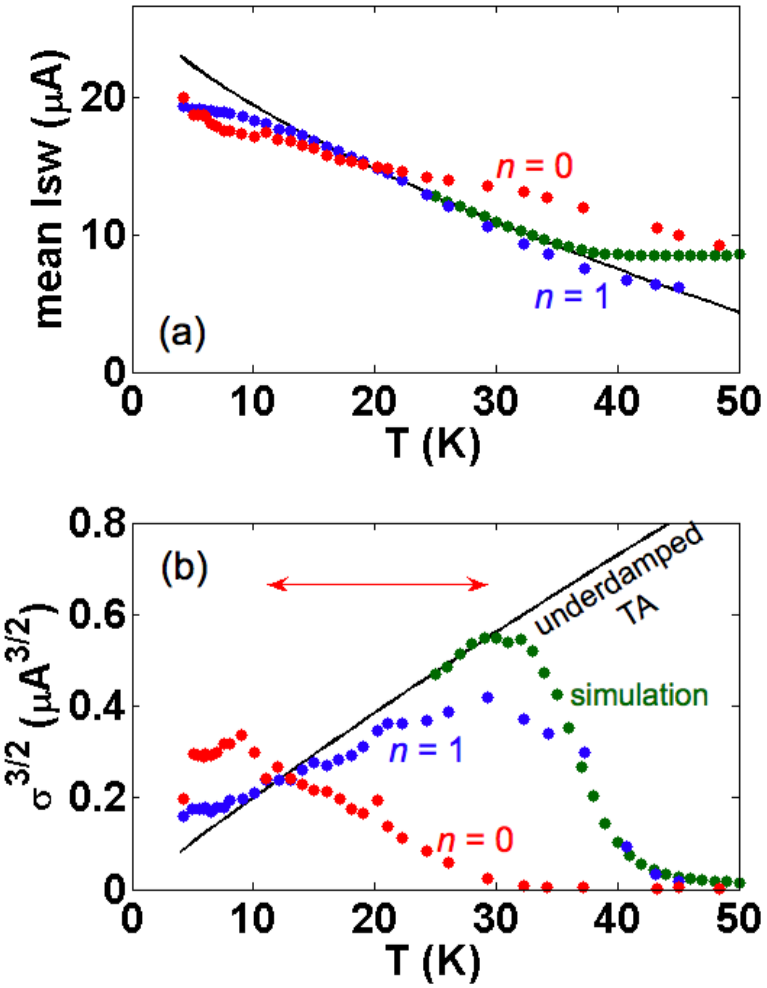

Figure 4.26: The bath-temperature-dependence of (a) the mean and (b) the standard deviation, σ, raised to the power of 3/2 of the switching current distributions of MK86-A3 shown in Figure 4.18. The red and blue points are the experimental data for branches $n = 0$ and $n = 1$ respectively. The green points are the results of Monte Carlo simulations of the repeated escape and retrapping events with fitting parameters $I_{cB} = 27.0$ μA (from the fits to the distributions for $T_{bath} <$ 29.3 K and $Q_B = 8.6$, both being taken to be independent of temperature. The black line shows the result of the standard underdamped thermal activation model with $I_{cB} = 27.0$ μA and $T_{eff} = T_{bath}$. The temperature range where the degree of self-heating is certainly less than 1 K on both branches is shown by the red arrow.

4.4.4.2 ASO caused by Josephson radiation

The second possible cause for the suppression of the switching current of branch 1 (junction B) can be Josephson emission of radiation from junction A when junction A is in voltage state. The suppression of the critical current in underdamped junctions was deduced by Kautz [1981] as

$$i_0 = J_0(\tilde{i}) \tag{4.1}$$

and $\tilde{i}$ is given as

$$\tilde{i} = i_l \Omega^{-1}(1 + \Omega^2\beta^2)^{-1/2}. \tag{4.2}$$

Here $i_0 = I_0/I_c$ where I_0 is dc bias current and I_c is the critical current of the junction. J_n is the Bessel function of n^{th} order. $\Omega = \omega(\hbar/2eI_cR)$ where ω is the RF frequency, $\beta = 2eI_cR^2C/\hbar$. $i_l = I_l/I_c$ is the RF current magnitude normalised to the critical current.

The maximum voltage of junction A is 26.7 mV as seen in IVC in Figure 4.15 at the top of first quasiparticle branch. This gives a frequency ω of 12.9 THz. This frequency is used to calculate the value of Ω. The I_cR_n value used to normalise Ω has been estimated from the 0 K energy gap for Tl2212 given by $2\Delta(0) = 3.52kT_c$. The calculated energy gap (16.7 meV) yields an I_cR_n value of 26.7 mV. The other parameters used to estimate the switching current suppression were Q_B=8.6 and $i_l = 1$. $i_l = 1$ was used as the worst case scenario in which RF current magnitude is as large as the switching current of the Josephson junction. Figure 4.27 shows the solution of Equation 4.1 in normalised units using the above parameters. This shows that even for an a.c Josephson current amplitude in junction A as large as its critical current I_{CA} i.e ($i_l = 1$), the suppression of the critical current I_{CB},

in junction B is less than 1% for all frequencies larger than 3.35 THz (i.e. 0.26 $I_{CB}R_B$).

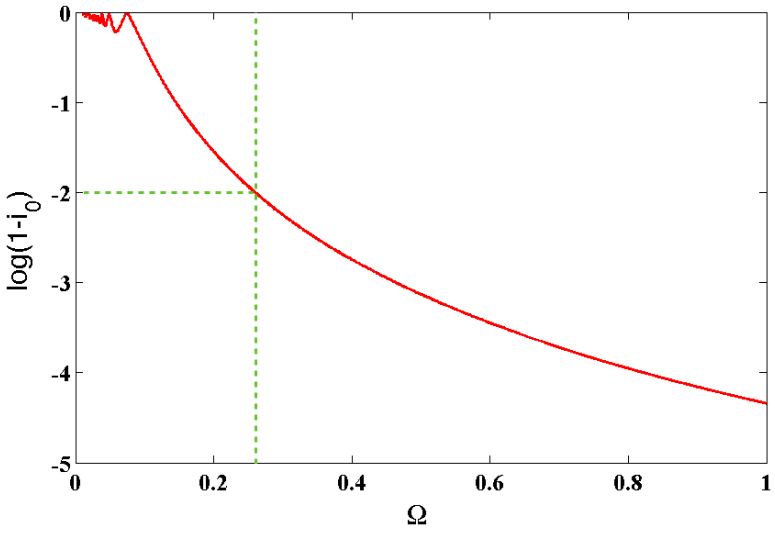

Figure 4.27: Frequency dependent critical current suppression by Josephson emissions. i_0 is the normalised switching current and Ω is the normalised frequency. The horizontal dashed line corresponds to a 1% suppression of the critical current.

4.4.4.3 ASO caused by different dissipation on branch 0 and 1

Another possibility is that the ASO and higher T^* are caused by different dissipation on the two branches. Dissipation in the washboard model is measured by $Q = \omega_p RC$. In Figure 4.20 for $T_{bath} > T_n^*$ (n is the branch number) it is not possible to achieve a good fit to the Kramers model with any $T_{eff} \geq T_{bath}$. This behaviour has been observed in a number of Josephson junction types [Kivioja *et al.*, 2005; Mannik *et al.*, 2005] including cuprate intrinsic junctions [Krasnov *et al.*, 2005b]. It results from rapid retrapping of the junction back into the zero-voltage state after it has entered the phase-slip state. To fit to the data for the $n = 1$ branch of Mk86-A3, the model of Fenton & Warburton [2008] was used with the temperature-independent value of I_{cB} extracted from fits to the data for $T < T_1^*$. The Stewart McCumber parameter, $\beta_{cB} = Q_B^2$, is likely to be temperature-dependent due to the dissipative effect of thermally-excited quasiparticles. In the absence of any prior knowledge of the form of its temperature-dependence, however, it was assumed to be independent of temperature, the value $Q_B = 8.6$ being selected so as to give a maximum in the switching distribution width at the same value as the experiment. In spite of this simplification a reasonable qualitative fit to the data for the $n = 1$ branch was achieved. The simulations shown in Figure 4.26 were performed by Dr Jon Fenton.

In summary for switching from n=1 branch we have I_{CB}=27.0 μA, Q_B=8.6 and plasma frequency of f_{pB} of about 400 GHz, using the relation $\omega_{pB} = [2eI_c/\hbar C]^{1/2}$. The real part of the impedance seen by junction B (300 Ω) is calculated from $Q = \omega_p RC$. Under the assumption that the junctions are structurally identical, it is assumed that $I_{cA} = I_{cB}$= 27.0 μA. Fenton & Warburton [2008] have shown that the temperature T^* at which the distribution width is maximum occurs when the escape rate, $\Gamma_{esc}(T^*, I)$ is equal to both the retrapping rate $\Gamma(T^*, I)$ and the normalised current bias sweeprate $I^{-1}dI/dt$ at some value of bias current I. Numerically solving Equation 2.33 and 2.21 for $I_{cA} = 27.0$ μA and $T_0^* = 9$ K,

the value of Q_A is obtained ($Q_A = 3.1$). The real part of the impedance seen by junction A, is thus of the order 100 Ω.

This suggests that, when increasing the bias current, the first intrinsic junction to switch (junction A) does so at a higher current than the second intrinsic junction to switch (junction B) due to the fact that the value of the Stewart-McCumber parameter when all junctions are in the zero-voltage state is significantly lower ($\beta_{cA} = Q_A^2 = 9.6$) than when one junction is in the voltage state ($\beta_{cB} = Q_B^2 = 74$). A similar dissipative-enhancement of the supercurrent in the thermal activation regime has previously been measured in LTS junctions [Tesche *et al.*, 1989]. They observed high values of switching current of Josephson junctions at temperatures where thermally activated switching was expected to drastically lower the maximum switching current. These large switching currents were shown to be due to retrapping during the transition to the voltage state.

In the current range $I_1 < I < I_0$ the state of each junction is entirely determined by dissipation. On the $n = 0$ branch the viscosity is sufficiently high that a thermally-activated escape event from the zero-voltage state to the phase-slip state in junction A is rapidly followed by retrapping to the zero-voltage state as shown in Figure 2.5. On the $n = 1$ branch, however, the viscosity of junction B is low enough that retrapping is unlikely and the steady phase-slip state develops. At $I = I_0$ on the $n = 0$ branch the energy provided by the bias current is sufficient to overcome the viscous retrapping and junction A enters the steady phase-slip state.

Three different explanations for ASO were offered which included self-heating, change in the dissipative environment and suppression of the switching current due to Josephson emission. It has been shown that self-heating and Josephson emission can not account for the suppression of the switching current of quasiparticle branches. A simple electrical model to validate the change in dissipative

environment is proposed.

4.4.5 Proposed Electrical Model

To explain why the dissipative enhancement of the supercurrent is greatest on the $n = 0$ branch, a simple high-frequency current-source model shown in Figure 4.28 is used. The model also includes the impedance, $Z_{env}(f)$, of the environment of the Josephson junction array. When all junctions are in the zero-voltage state (Figure 4.28 (a)) the impedance seen by any junction in the array is $Z_{env}(f)$. At $f = f_P$, the environmental impedance is approximately 100 Ω, which is the typical impedance of the current bias wiring lines attached to the junction [Tinkham, 1996]. When one junction is in the voltage state (Figure 4.28 (b)), the impedance seen by the other junctions in the array is now $Z_{env}(f) + R$, where R is the ac resistance of a single junction (of the order of a few hundred ohms). This increased impedance leads to an increase in Q and therefore a significant reduction in the dissipative enhancement of the supercurrent. The applicability of this model to IJJ arrays in which R exceeds 100 Ω has also been confirmed by measurements of thermally-activated phase diffusion [Fenton *et al.*, 2007] and microwave-induced Josephson vortex flow (see [Saleem *et al.*, 2009] and section 4.5).

In summary two major results were observed, (i) higher switching current for branch zero than branch 1 termed as ASO and (ii) higher T^* for branch 1 than branch 0. Both these results can be explained by the change in dissipative environment when one junction switches to the voltage state. This change in dissipation enhances the supercurrent in an IJJ array in the thermal-activation regime above that which would be expected for an underdamped junction of equal critical current. The dissipation results from the shunting impedance of the environment and can therefore be reduced (leading to a reduction in the supercurrent) by switching a single IJJ into the voltage state. This results in the anomalous switching order often observed in IJJ experiments and a higher T^* for

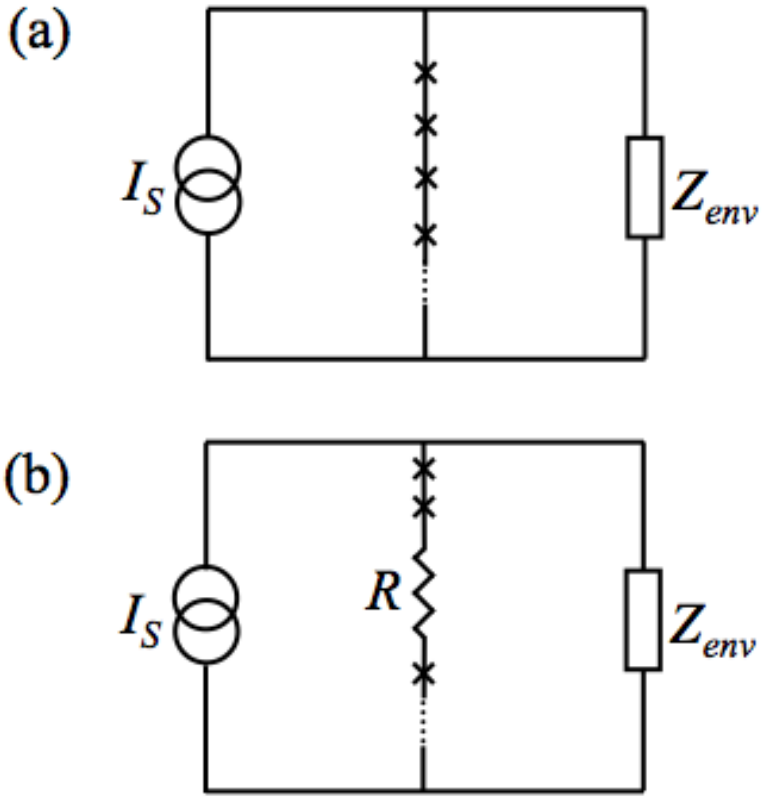

Figure 4.28: Circuit model showing the change of high-frequency impedance seen by any junction in the series array when one junction switches from the zero-voltage state (a) to the voltage state (b). Each junction is shown as a cross and is modelled as having negligible impedance when in the zero-voltage state. I_S is a d.c. current source of infinite impedance. Z_{env} models the impedance of the environment of the array. R models the ac resistance of a single junction when in the voltage state.

higher order branch as compared to the supercurrent branch.

4.5 Switching Current Measurements under RF Irradiation

4.5.1 Overview

A total of seven IJJ stacks were irradiated with RF between 2 and 20 GHz, to understand the dynamical behaviour of the junction stack under microwave irradiation. Both static and switching-current-distribution measurements were made on these samples. An overview of the type of measurements performed on these samples is shown in Figure 4.29.

The frequency was chosen by observing the suppression of the switching current of supercurrent branch. The frequency at which maximum suppression of the switching current of the supercurrent branch was observed was selected to perform subsequent measurements. It is pertinent to mention that the selected frequency is much lower than the plasma frequency ($f \ll f_p$). Systematic frequency-dependent measurements were not performed due to different coupling to the IJJ stack at different frequencies. The system is poorly matched at certain RF frequencies resulting in insufficient power reaching the sample at those frequencies.

4.5.2 Results

Figure 4.30 shows the dependence of the dc current-voltage characteristics of the junction stack shown in Figure 4.4 upon the RF power level at 6.37 GHz. At zero microwave power the current-voltage characteristics are multi-branched and hysteretic, similar to all the junction stacks mentioned in Figure 4.29. The supercurrent branch is at zero voltage. Once the current bias exceeds the switching current of the supercurrent branch (here 7.6 μA), it is possible to sweep out N quasiparticle branches where N is the number of IJJs in the stack. (N is ap-

Sample	Branch(es) from which switching current distribution were measured	Static IVs at different RF power
Mk56AD[I]-A9	0	Yes
Mk56AD[I]-A4	0	Yes
Mk87-B1	Nil	Yes
Mk86-A3	0	No
UCL3-A6	0	No
UCL3-A7	0, 2	No
UCL5a-B6	0, 1, 2	No

Figure 4.29: Samples used to study the effects of RF on IJJ stacks and types of measurements along with the branch number.

proximately 100 for junction array reported here.) For clarity only the first and second quasiparticle branches are shown in Figure 4.30. A more detailed view of the supercurrent branch and sub-branch is shown in Figure 4.31.

Major changes in the DC IVs for non zero RF power as seen in Figure 4.30 and 4.31 include the following three observations:

- Suppression of the switching current of the supercurrent branch with increasing RF power.
- The appearance of a sub-branch between the supercurrent and first quasiparticle branch; the voltage of the sub-branch increases with increasing rf power.
- Very small switching current suppression and the absence of sub-branches for the first and second quasiparticle branches.

All the above observations will be discussed and analysed in this section.

4.5.3 Analysis

4.5.3.1 Suppression of switching current of branch zero

Suppression of the switching current for the supercurrent branch can be understood with the help of the tilted washboard model. The tilt of the washboard and the barrier height have one fixed value at any given DC bias current. The applied RF current causes the tilt of the washboard and the height of the energy barrier to oscillate around their mean value. An increase in the washboard tilt and reduction in the energy barrier means that the particle needs less energy to escape from the local minimum, thus resulting in the particle escaping at a lower value of d.c. switching current. Thus the application of RF current results in suppression of the switching current for the supercurrent branch. This suppression increases with the RF power as shown in Figure 4.31.

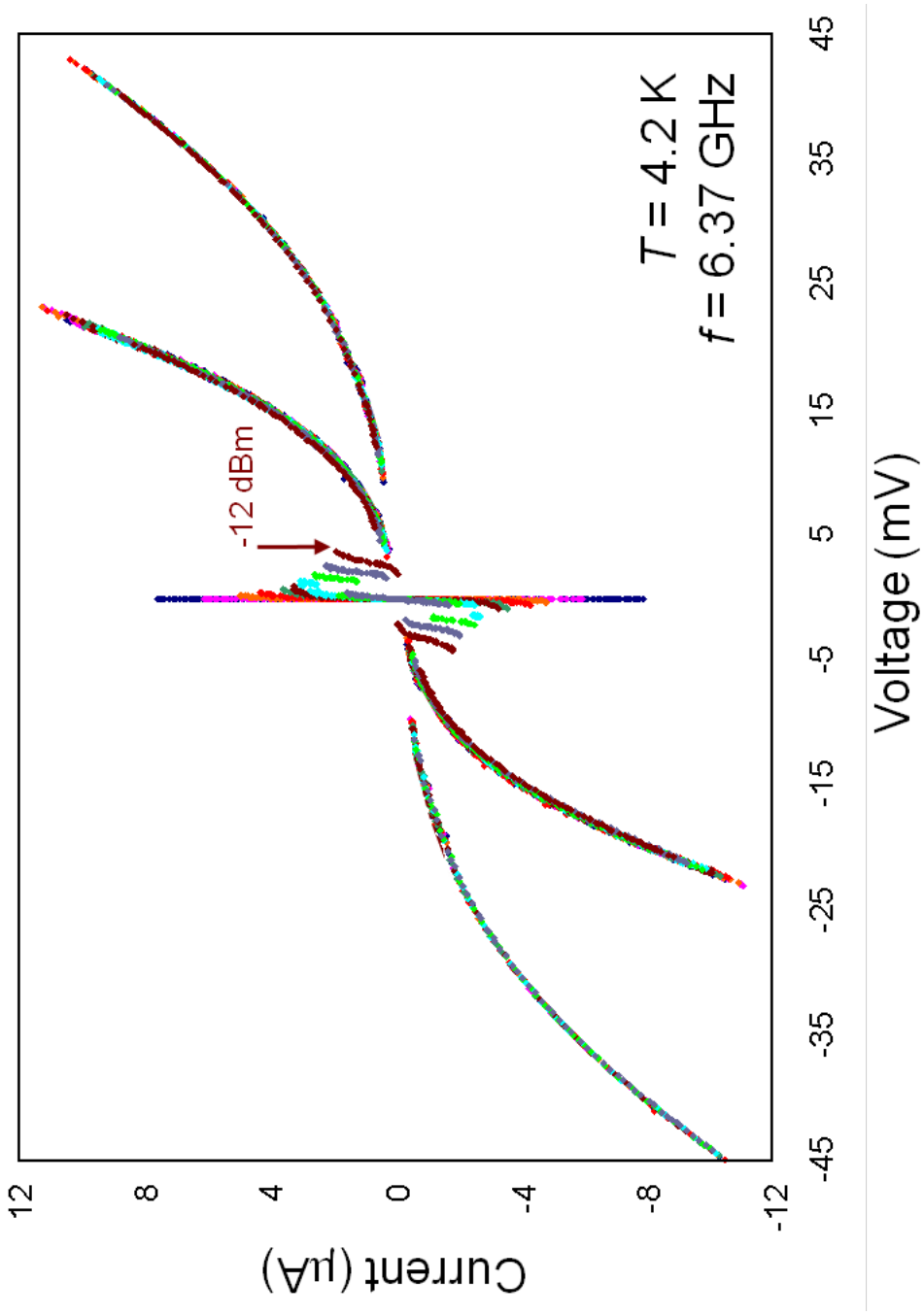

Figure 4.30: DC Current-Voltage characteristics of the IJJ stack when the RF power is varied from 0 to -12 dBm. Only first three branches (the supercurrent branch and first two quasiparticle branches) are shown. The arrow indicates the vortex flow branch when RF power is -12 dBm.

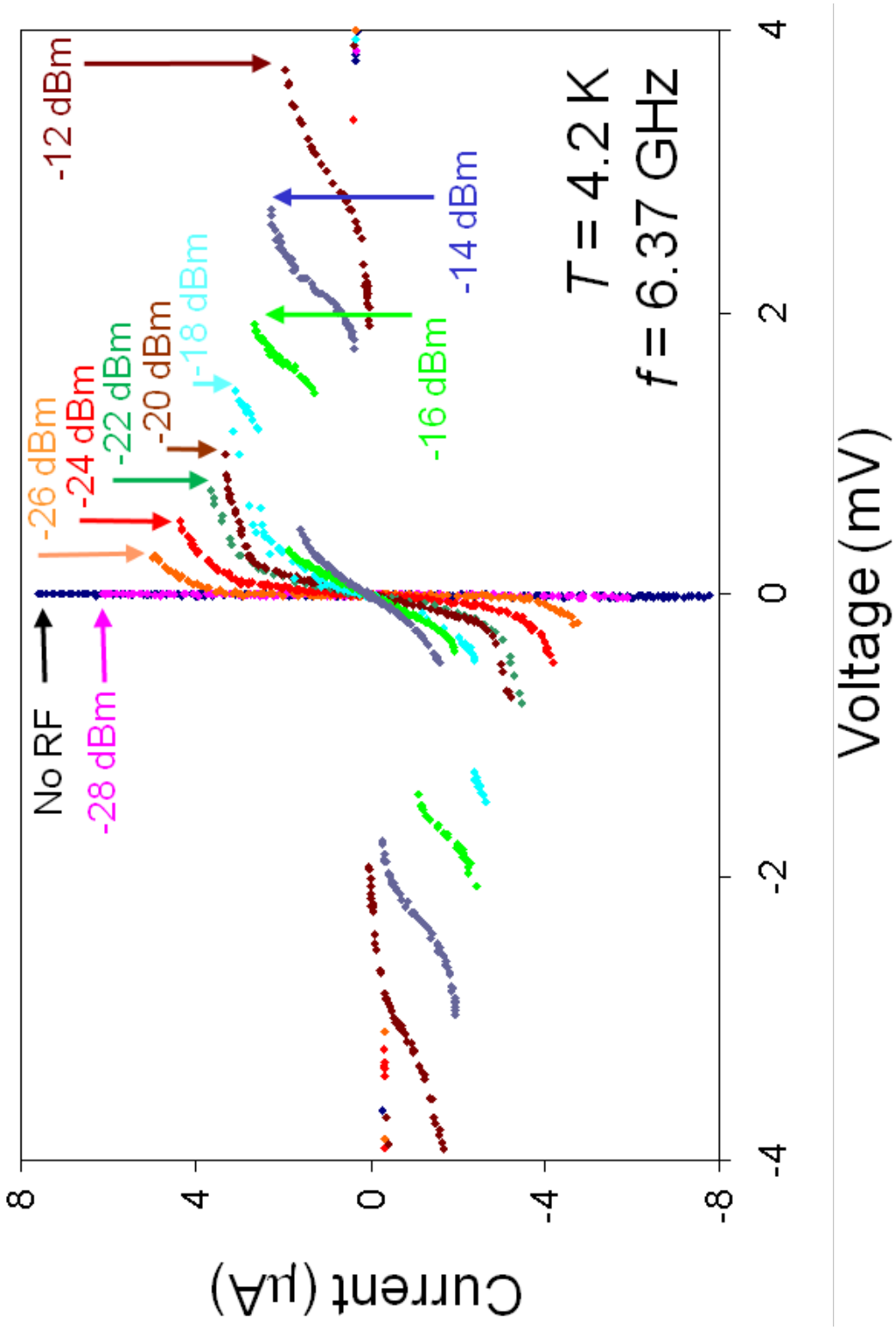

Figure 4.31: Low voltage region of the of the dc Current-Voltage characteristics. Arrows point to the maximum voltage on the vortex-flow branch. Power levels are referred to the output of the source.

4.5.3.2 Appearance and movement of Vortex flow branch

At higher RF powers a low-voltage branch appears between the supercurrent branch and the quasiparticle branch as shown in Figure 4.30. The dependence of the voltage at the top of this low-voltage branch upon the microwave current is shown in Figure 4.32. Data presented in this graph can be divided in two distinct regions. Region I is for microwave currents below 0.04 units. Within this region the voltage of the low-voltage branch is zero. Region II is for the microwave currents greater than 0.04 units. In this region the step voltage of the low-voltage branch has a linear dependence on the microwave current. Similar behaviour has been observed by number of other research groups [Barkov *et al.*, 2004; Helm *et al.*, 2000; Hirata *et al.*, 2001; Irie *et al.*, 2003; Tachiki & Uchida, 2008].

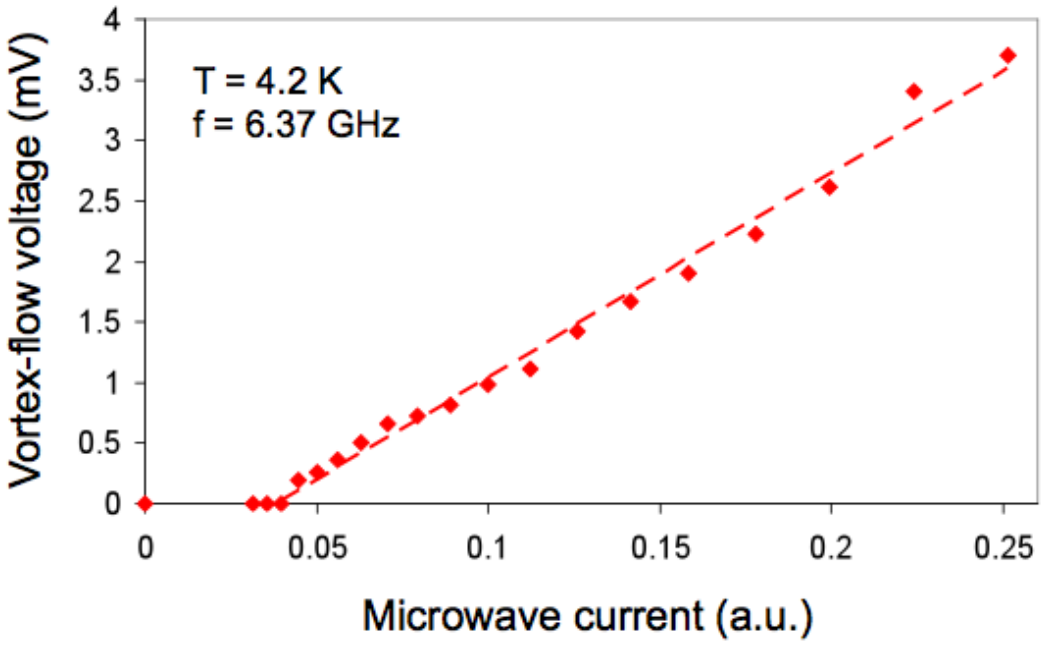

Figure 4.32: Maximum voltage of the vortex flow branch as a function of the RF current. The line is a linear fit to the data above 0.04 microwave current units.

In region II the linear dependence of the step voltage on microwave current is very similar to the magnetic field dependence of the voltage of the flux flow step

for a conventional long Josephson junction as described in 2.4.2.2. This suggests that the microwaves insert fluxons in junctions due to their magnetic component [Oya & Irie, 1996]. The bias current then accelerates the inserted fluxons due to Lorentz force, resulting in the step voltage of the low-voltage branch. The number of fluxons in the junction is increased by increasing the power of the microwaves and hence the step voltage also increases. The linear dependence of the step voltage on microwave power confirms that the dissipation mechanism on this low-voltage branch is microwave-induced Josephson vortex-flow [Irie & Oya, 1995; Irie *et al.*, 1996]. In region I either there are no Josephson fluxons present or any Josephson fluxons present are pinned.

4.5.3.3 Absence of vortex flow branch on quasiparticle branches

The microwave-induced vortex-flow branch only appears close to the supercurrent branch; when a single intrinsic junction is in the voltage state the vortex-flow branch is totally suppressed. The absence of vortex flow branch on quasiparticle branches can be interpreted in two ways i.e (i) dissipation due to quasiparticle tunnelling suppresses the flow of Josephson vortices; or (ii) when one junction is in the voltage state there are no Josephson vortices in the array. These explanations can be understood by plotting the dependence of the first three switching currents upon the applied microwave current which is shown in Figure 4.33. It is observed that the switching current on the zeroth branch is rapidly suppressed by the RF current, whereas that of the subsequent branches is only marginally suppressed. Scatter in the measurements on branches 1 and 2 is due to thermal fluctuations. The vertical bar shows the theoretically calculated standard deviation of the switching current for branch 1 using the thermal underdamped model explained in 4.4.4.

I argue that higher suppression of the switching current on the supercurrent branch as compared to quasiparticle branches indicates that the microwave field

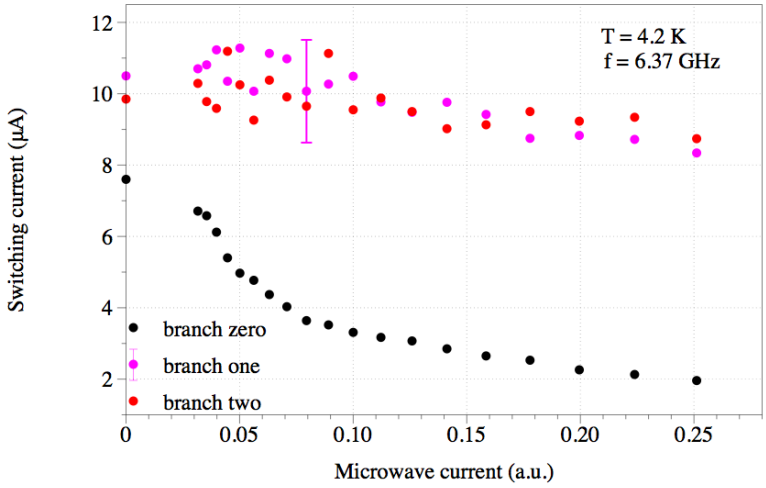

Figure 4.33: Switching current dependence of supercurrent (branch 0) and first (branch 1) and second (branch 2) quasiparticle branches on the RF current. The vertical bar shows the calculated standard deviation of the switching current for branch one at 10 μA and 4.2 K.

couples much less strongly to the IJJ array when a single intrinsic junction is in the voltage state than when all the junctions are in the superconducting state. This accounts for the observation that the microwave-induced Josephson vortex-flow branch can only be observed when all the junctions are in the superconducting state; since the microwave field couples poorly when a single junction is in the voltage state, no Josephson vortices are inserted in the junction stack.

It has been shown in section 4.4.4 and by Fenton *et al.* [2007] that thermally activated phase diffusion occurs only on the supercurrent branch and not on the quasiparticle branches. Phase diffusion can only be observed in hysteretic Josephson junctions when the junction resistance is larger than the RF impedance of the environment which is of order 100 Ω for a current biased Josephson junction [Tinkham, 1996]. This suggests that the environmental impedance may also be playing a role in determining how well the microwave field couples to the junction array.

4.5.4 Proposed Electrical Model

A simple circuit model similar to the model presented in Figure 4.28 is shown in Figure 4.34 to explain these results.

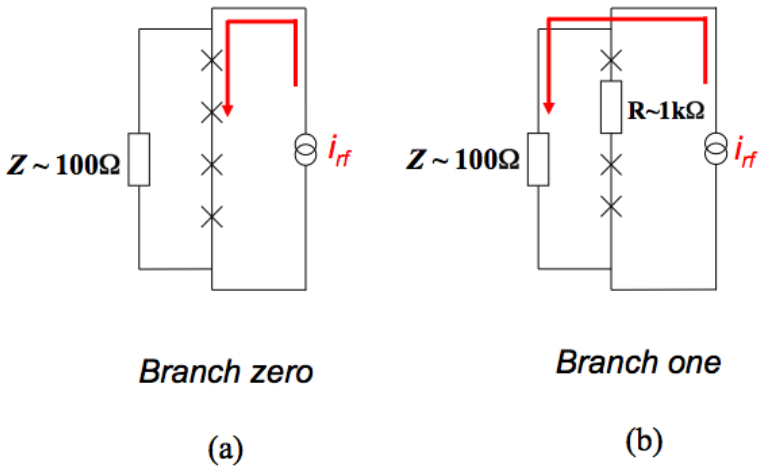

Figure 4.34: Switching current dependence of supercurrent (branch 0) and first (branch 1) and second (branch 2) quasiparticle branches on the RF current

In this model the microwave irradiation is modelled by using an RF current source due to the low impedance of the Josephson junction. When all the junctions are in the superconducting state the RF impedance of the junction array is low. The inductive reactance of the Josephson junction is calculated using $X_L = 2\pi f L$ where L is given by $\Phi_0/2\pi I_c$. For a critical current of order of 10 μA and frequency of 6.7 GHz, the inductive reactance is of the order 1 Ω. Hence, the RF current flows through the junction array. The AC resistance of a single junction in the voltage state determined from the slope of the current-voltage characteristics from Figure 4.30 is between 1 kΩ and 10 kΩ. With one junction in the voltage state therefore the junction is effectively shorted by the environmental impedance and very little RF current couples to the junction array.

Bae *et al.* [2003] showed that below some cut-off frequency (in their case around 80 GHz) the RF fields were uniformly distributed in the junction stack, whereas above this cut-off frequency a standing wave was set up between the

top and the bottom of the stack. The main difference between their results and mine is that I do not see any suppression of switching currents for quasiparticle branches. My junctions were irradiated at a much lower frequency than in Bae *et al.* [2003] so that uniform irradiation across the stack is expected, provided the radiation couples to the junction at all. It has been shown that coupling only occurs when all the junctions are in the superconducting state. The difference between my data and those of Bae et al. arises from the much smaller junction area in my case compared to Bae *et al.* [2003]. A large junction area of 18 μm^2 in their experiment leads to a lower junction resistance in the voltage state which means that the environmental impedance plays no role.

This section described the effects of microwaves on the DC IVs of IJJs. RF induced observations included higher suppression of the switching current for the supercurrent branch than the quasiparticle branches, the appearance of a vortex-flow branch and the absence of the vortex-flow branch for quasiparticle branches. These results were analysed with the help of the proposed electrical model. It was found that microwaves couple to the IJJ when all the junctions are in the superconducting state and no vortices are inserted when a junction is in the voltage state.

4.6 Environmental Isolation of IJJ Stacks

4.6.1 Overview

All the results in the preceding two sections in this chapter are explained with reference to the environmental impedance. The next step in this research was, therefore, to try to isolate the IJJ stack from its environment so as to test the validity of this explanation. Isolating the Josephson junction from its environmental impedance with resistors would change the value of the impedance seen by the junctions and hence would change the damping in the system, as $Q = \omega_p RC$. Changing the damping in-situ at 4.2 K would confirm the proposed explanation for the anomalous switching order.

Josephson junctions have been isolated from their environment previously using resistors [Kuzmin & Haviland, 1991]. A lead-alloy junction with an area of 0.01 μm^2 was isolated from its electromagnetic environment by high resistance metallic resistors inserted into the current and voltage leads.

4.6.2 Key requirements for isolating resistors

One key requirement was the value of the isolating resistors. This must exceed the environmental impedance and be less than the resistance of quasiparticle branch to effectively isolate the junction array from its environment while still permitting switching current measurements. Keeping these requirements in view, each resistor should have a value between 100 Ω and 500 Ω.

The second requirement for the isolating resistors was their distance from the IJJ stack. In order for the junction to see a pure resistance and not a complex impedance, the isolating resistors must be within close proximity of the junction stack. The plasma frequency in our IJJ stacks is nearly 10^{12} Hz; the dielectric constant of the substrate is about 10 so that the wavelength is about 100 microns. It was decided to put the isolating resistors 6 μm away on each side of the IJJ

stack, well within one wavelength.

The third requirement for the resistors was their capability to change resistance in-situ, so as to measure the IV characteristics and switching distributions with and without the effect of the environmental impedance. It was decided to use FIB-deposited tungsten as resistors, as FIB deposited tungsten is known to act as a superconductor with a critical temperature of about 5.3 K [Li *et al.*, 2009]. With FIB-deposited tungsten resistors and the IJJ stack at 4.2 K, we would expect to see similar results as discussed in this chapter, as the entire structure, (i.e the IJJ stack and tungsten resistors on either side) will be superconducting. It was envisioned that once the sample temperature will be raised to $\approx$ 6 K (above the critical temperature of FIB-deposited tungsten), the resistors will isolate the junction stack from its environment. A complete IJJ stack with isolating resistors is shown in 4.35.

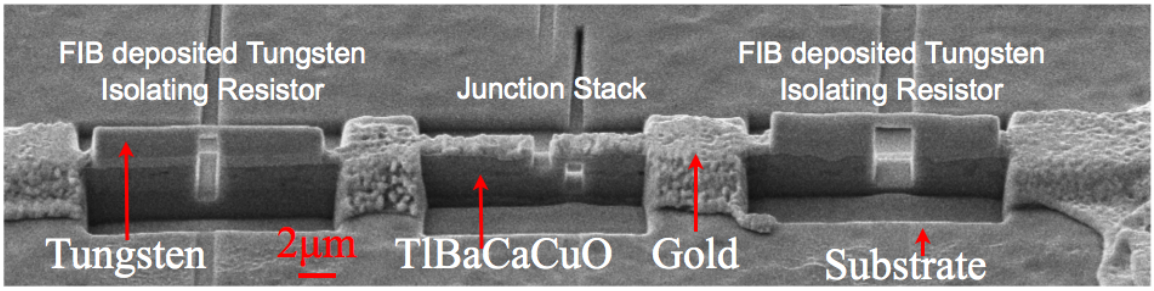

Figure 4.35: Complete IJJ stack with isolating resistors. FIB deposited resistors are 6 μm apart on either side of the IJJ stack. The gold in the picture is on top of the Tl2212 track.

4.6.3 Approaches to FIB tungsten deposition

Three different approaches were used to deposit the FIB tungsten resistors. The first approach was to cut the central Tl2212 track and then deposit the tungsten as in Figure 4.36a. This approach did not produce consistent results in terms of the value of the resistance obtained from sample to sample due to incomplete step coverage. A layering effect was also observed in the deposited tungsten.

This approach suffered from the nozzle shadowing effect (discussed later on in this section) depending on the orientation of the central track with respect to the Gas Injection System (GIS) nozzle.

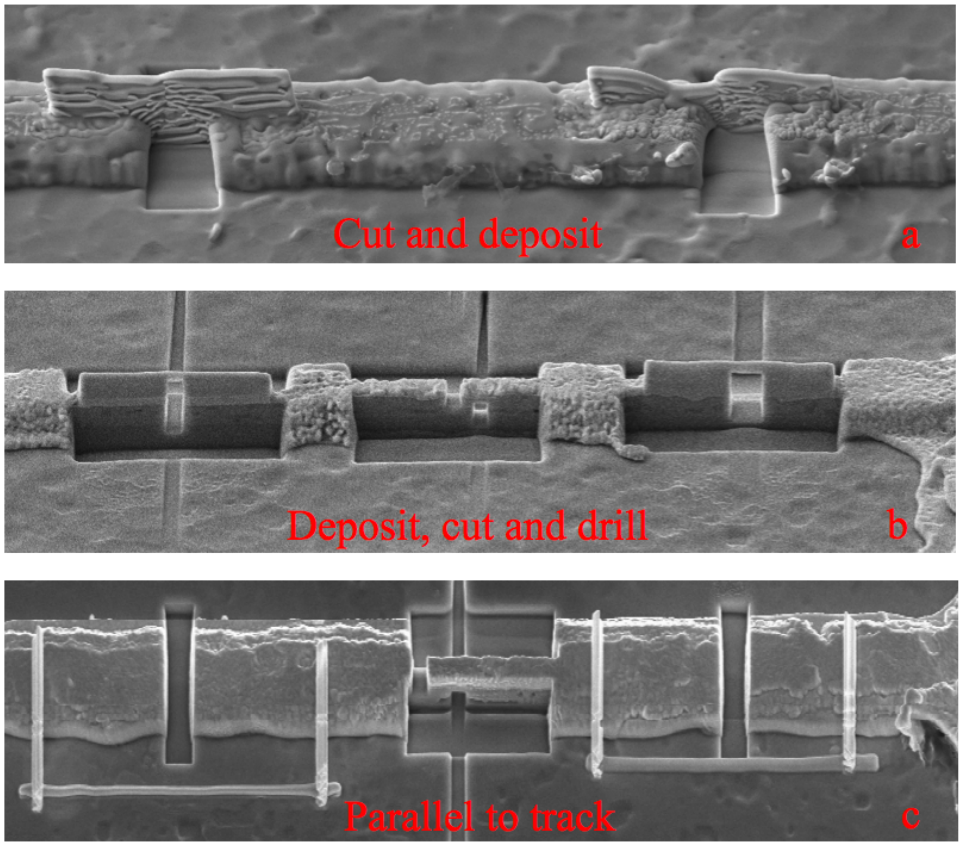

Figure 4.36: Three different approaches to the FIB tungsten deposition. (a) The central track is cut first and then tungsten is deposited in the hole. Due to the step height a break in deposition occurred. Note the layering effect in the deposition as well. (b) Tungsten resistors were deposited first and then narrowed down from the side and drilled under to obtain the desired resistance value. Dimensional control of the deposited tungsten in milling step was difficult. (c) Central track is cut and then tungsten is deposited parallel to the central track. The step height in this approach is smaller as compared to (a) and extra tungsten pads ensure that no break in the deposition occurs. Dimensional control of resistors is easier as compared to (b).

The second approach is shown in Figure 4.36b. In this approach tungsten resistors were deposited first on top of the central Tl2212 track and then the track was narrowed down from both sides and then the narrowed track was drilled underneath the resistors in order to obtain the desired value of the resistors. This

approach produced consistent results as there were no breaks in the tungsten deposition with this approach. However dimension control of the deposited resistors while milling after deposition was difficult. Not being able to thin and narrow the deposited resistors to the required dimensions and the lack of a facility to measure the resistance in-situ while milling forced us to abandon this approach.

The third approach which was successful and finally used for this research is shown in Figure 4.36c. In this approach the central Tl2212 track was cut in the middle and then tungsten was deposited parallel to the central track. In this approach the height of the step over which tungsten is deposited was smaller than the first approach. Extra patches of tungsten were deposited where the step occurred to ensure a good contact. The dimensional control of resistors was easier in this approach as compared to the second approach.

Samples initially used for the deposition of tungsten suffered from high resistance. The source of high resistance in first approach was incomplete step coverage and the interface resistance between the deposited tungsten and the top of the track. In second approach the interface between the deposited tungsten and top of the central track was isolated as the source for high resistance. The initial samples did not had a uniform gold layer and hence suffered from high resistance. An extra gold layer on later samples ensured that the contact resistance was less than 1 Ω.

4.6.4 Nozzle shadow effect

One observation during the resistor deposition was that some samples provided comparably good results using the first approach than other samples on the same chip. A number of control experiments confirmed that this difference between the resistance value of the samples on the same chip was due to the different orientation of the sample with respect to the GIS nozzle during deposition. This effect we term as the 'nozzle shadowing effect'.

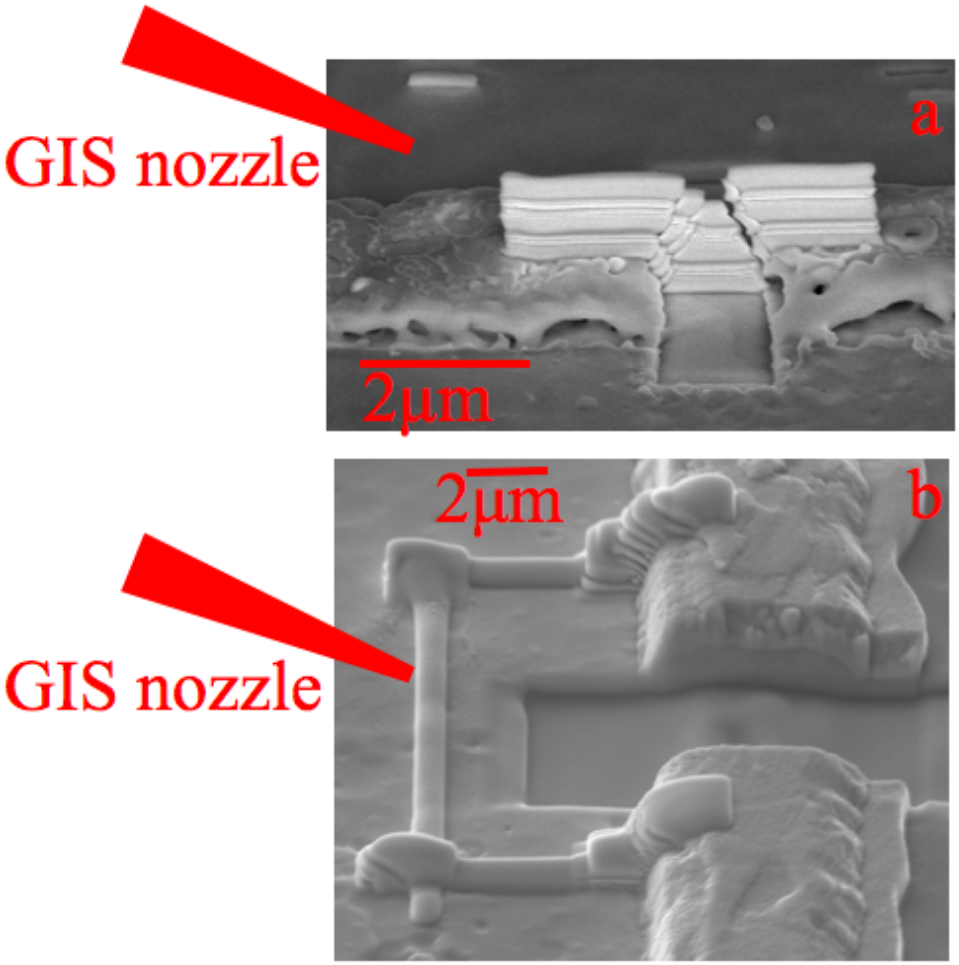

Figure 4.37: Nozzle shadow effect. Deposition in the cut/step would produce different results based on the orientation of the sample with respect to GIS Nozzle. (a) suffers from the nozzle shadow effect where a break in the deposition is observed whenever there is a step. (b) The nozzle shadow effect can be avoided by orienting the TBCCO track perpendicular to the nozzle.

The nozzle shadowing effect is explained in Figure 4.37. It was learnt that whenever the central track was oriented parallel to the GIS nozzle as in Figure 4.37 a, deposited tungsten suffered from some minor break in the deposition and the value of the resistance obtained was high. In contrast samples where the central track was oriented perpendicular to the GIS nozzle as in Figure 4.37b did not suffer from a break in the deposition. All the samples prepared afterwards were oriented perpendicular to the GIS nozzle to avoid the nozzle shadowing.

4.6.5 Results and Analysis

Three point IV characteristics of a single FIB deposited tungsten resistor are shown in Figure 4.38. The dimensions of the FIB-deposited patch parallel to the central track in Figure 4.37 b and also in the inset of Figure 4.38 marked with an arrow, are 7 μm, 0.3 μm and 0.3 μm. The resistor was deposited using a 20 pA FIB probe current with an X scan frequency of 20 kHz and Y scan frequency of 0.2 Hz at a $W(CO)_6$ partial pressure of 0.23×10^{-5} mbar. IV characteristics of the deposited resistor at 4.2 K show a critical current of 165 μA. The other two transitions in the IV at 4.2 K are from the extra tungsten patches to ensure step coverage in the deposition. The transitions seen in the IV at 4.2 K are not present in the measurement at 11 K establishing the fact that these transitions are originating from the FIB deposited tungsten. The most probable cause of hysteresis in the IV is heating.

The dependence of the resistance of the fib-deposited tungsten is shown in Figure 4.39. The resistive transition of TlBaCaCuO is also visible close to 100 K. From the measurements we extract the resistivity of tungsten (160 $\mu\Omega$cm) and its critical current density (2100×10^6 A/m^2). These values are in line with the previously reported results [Prestigiacomo *et al.*, 2005; Ross *et al.*, 2006; Sadki *et al.*, 2004].

After the successful deposition of one tungsten resistor and confirming its

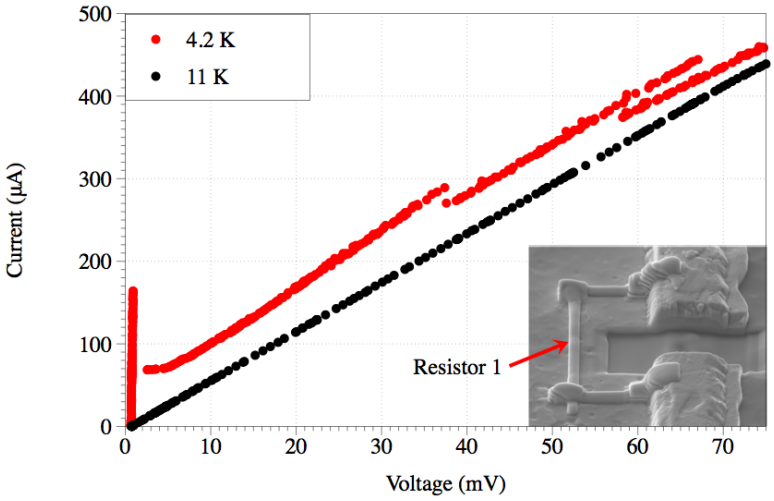

Figure 4.38: Current voltage characteristics of FIB deposited tungsten resistor at 4.2 K (red points) and 11 K (black points). Resistor dimensions parallel to central track are 7 μm, 0.3 μm and 0.3 μm as shown in the inset.

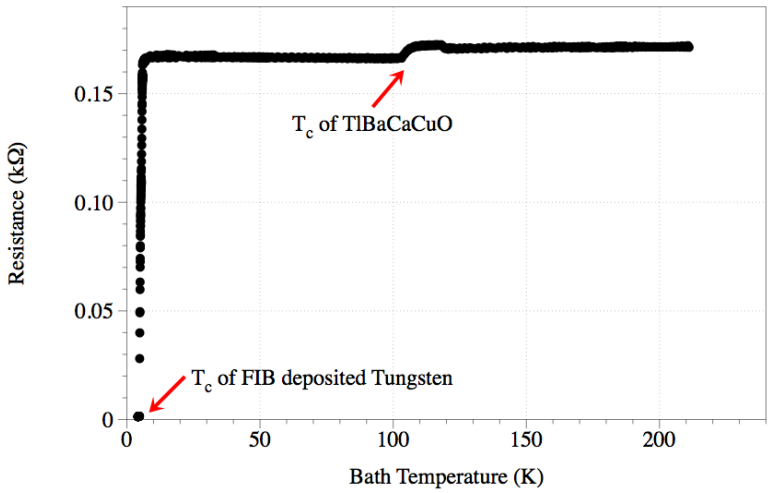

Figure 4.39: Resistance dependence of tungsten on temperature. FIB deposited tungsten has a T_c of about 5.3 K.

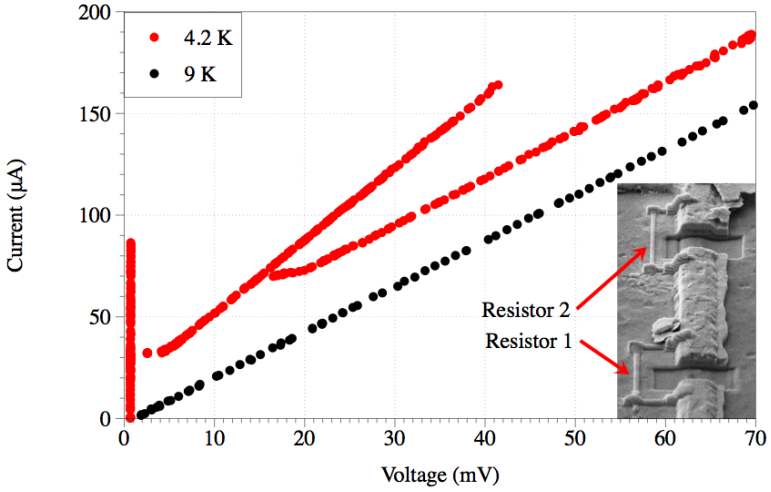

Figure 4.40: Current voltage characteristics of the series combination of resistor 1 and resistor 2 at 4.2 K (red points) and 9 K (black points). Resistor 2 dimensions parallel to central track are 7 μm, 0.2 μm and 0.2 μm as shown in inset. Electrical characteristics of resistor 1 are shown in Figure 4.38 and 4.39.

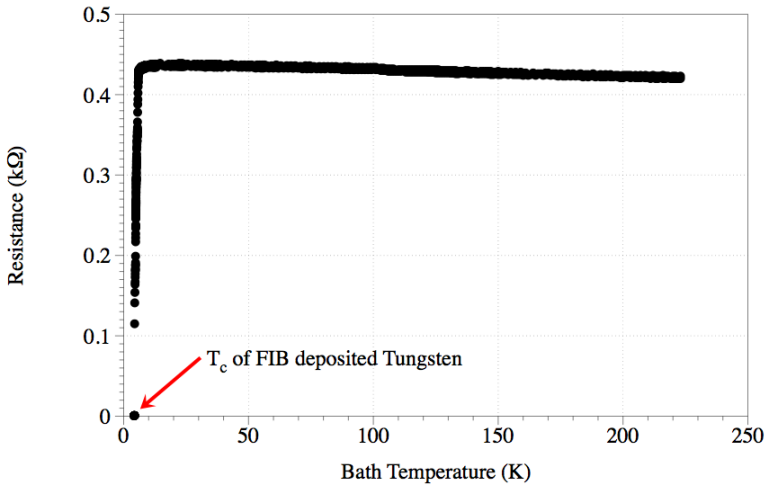

Figure 4.41: Dependence of the resistance of the series combination of resistor 1 and resistor 2 on temperature. FIB deposited tungsten has a T_c of about 5 K. The resistance of the complete structure is 430 Ω.

superconductivity and resistance value, a second resistor was deposited on the same sample, in series with the first resistor. The combined current voltage (IV) characteristics of the second resistor at 4.2 K and 9 K are shown in Figure 4.40. The critical current of the second resistor is about 90 μA which is less than the critical current of first resistor as the cross-sectional area of the second resistor is smaller than that of the first resistor. The I_c at 170 μA is from resistor one. Similar to the first resistor we do see some other transition in the IV of the second resistor at 4.2 K originating from the patches in the tungsten deposition. Measurement of the IV at 9 K confirms the origin of these transitions to be FIB-deposited tungsten. The temperature dependence of the resistance of the whole structure was measured and is shown in Figure 4.41. Due to the use of a four point measurement the TBCCO transition seen in 4.39 is not resolvable here. The resistance of the structure has increased from 167 Ω to 430 Ω as the area of the second resistor is smaller than the area of the first resistor. The T_c of the tungsten was again found to be above 5 K. A number of tungsten resistors was deposited which were 7 μm long and 0.2 μm wide and 0.2 μm thick. The critical current of these resistors was found to be 40 μA $\pm$ 10 μA. The contact resistance was always found to be less than 5 Ω. The typical value of these resistors was found to be between 100 Ω and 500 Ω.

A completed structure consisting of a junction stack between two resistors is shown in Figure 4.42. This we refer to as the RJR structure. The RJR structure was fabricated in a single cycle in the FIB without breaking vacuum. Its IV characteristics at 4.2 K are shown in Figure 4.43. The IV of the RJR structure is multi-branched indicating presence of the IJJ array. The inter-branch voltage difference of 20 to 25 mV is in agreement with a standalone IJJ array. An important point to note is the absence of the supercurrent branch, despite the fact that the whole structure (Resistance - Junction - Resistor) is superconducting at 4.2 K. It is possible that the first branch we see in this IV is the supercurrent

branch with some additional resistance of unknown origin. The value of the resistance on the first branch at 4 μA is $\approx$ 16 $k\Omega$.

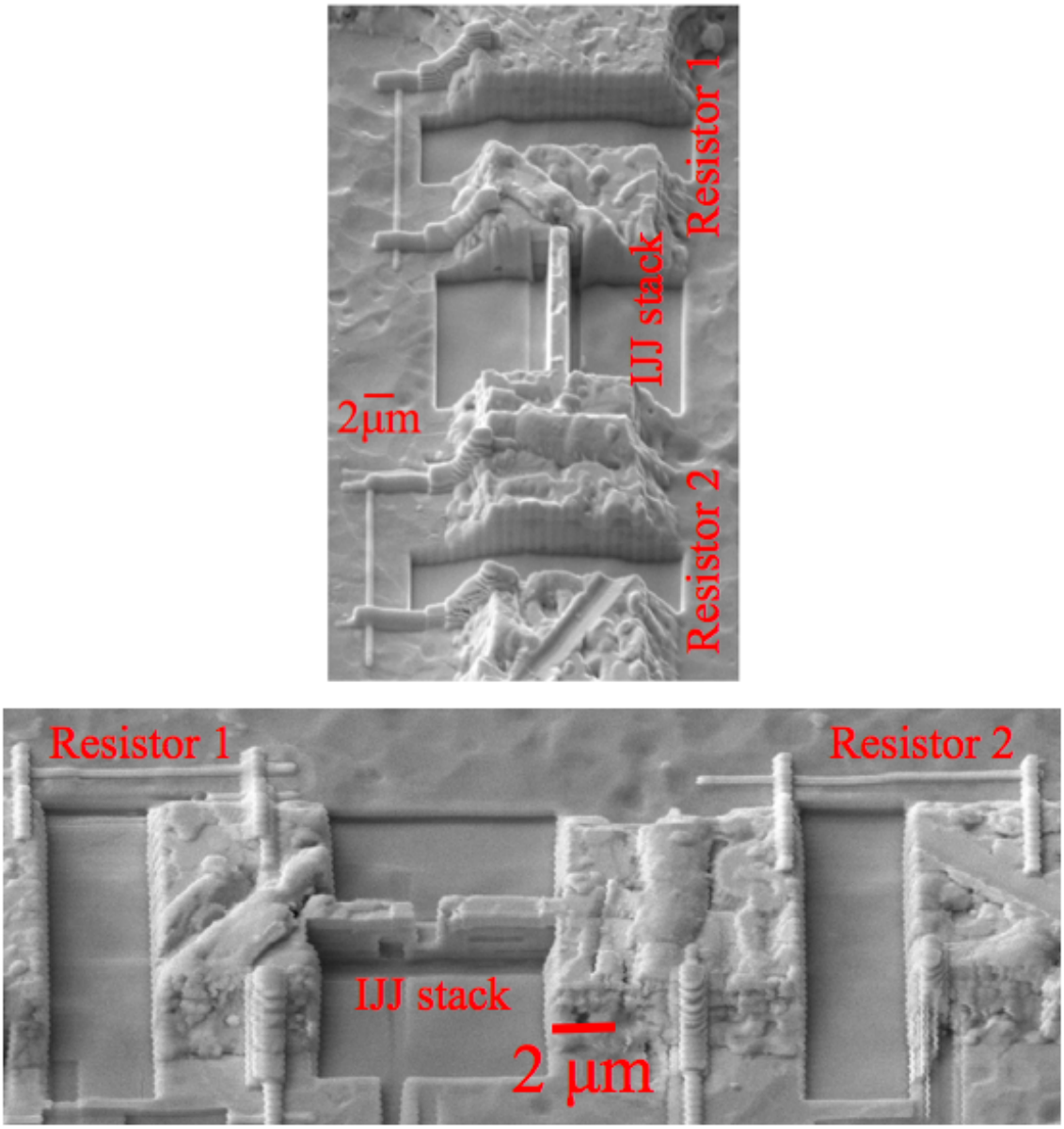

Figure 4.42: Complete Resistor-junction stack-Resistor structure perpendicular (top) and parallel (bottom) to GIS nozzle (top). Both resistors have an area of 0.2 μm by 0.2 μm and a length of 7 μm. The junction stack width is 667 nm and length is 352 nm.

The high resistance at 4.2 K is not present when we fabricate and measure only the junction stack without the isolating resistors nor vice-versa. The contact

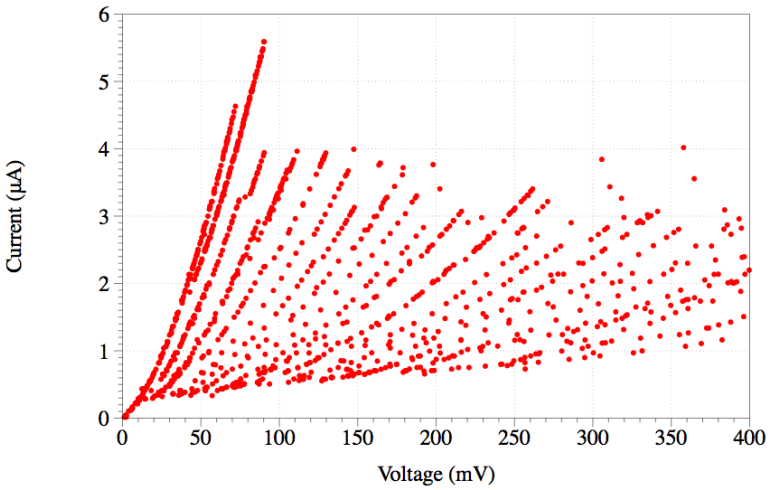

Figure 4.43: Current-Voltage characteristics of the RJR structure shown in Figure 4.42 at 4.2 K.

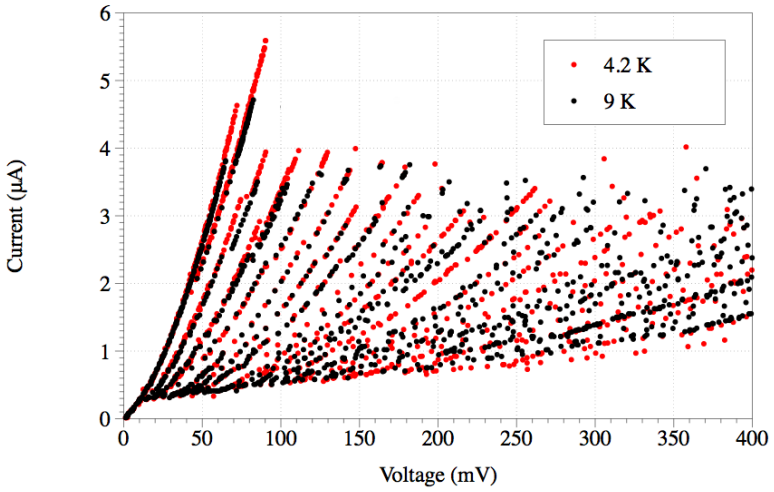

Figure 4.44: Current-Voltage characteristics of the RJR structure shown in Figure 4.42 at 4 K (red data points) and 9 K (black data points).

resistance is minimal and its typical value is less than 5 Ω. Figure 4.44 shows the IV of same structure at both 4 K (red data points) and 9 K (black data points). They appear to be the same, however on closer inspection at low voltage the resistance has increased. This increased branch resistance at 9 K originates from the non superconductivity of FIB deposited tungsten at 9 K.

This increase in resistance can be estimated from Figure 4.45. This figure shows the first branch above (black data points) and below (red data points) the expected transition temperature of the tungsten. The green data points are obtained by adding a fix value resistance of 300 Ω to the data below the transition temperature of tungsten. Green data points lie on top of the black data indicating the value of change in resistance of tungsten above its critical temperature as compared to the resistance value below the transition temperature. This gives a resistance value of ≈ 150 Ω per isolating resistor, which is within the required designed value of 100 Ω to 500 Ω.

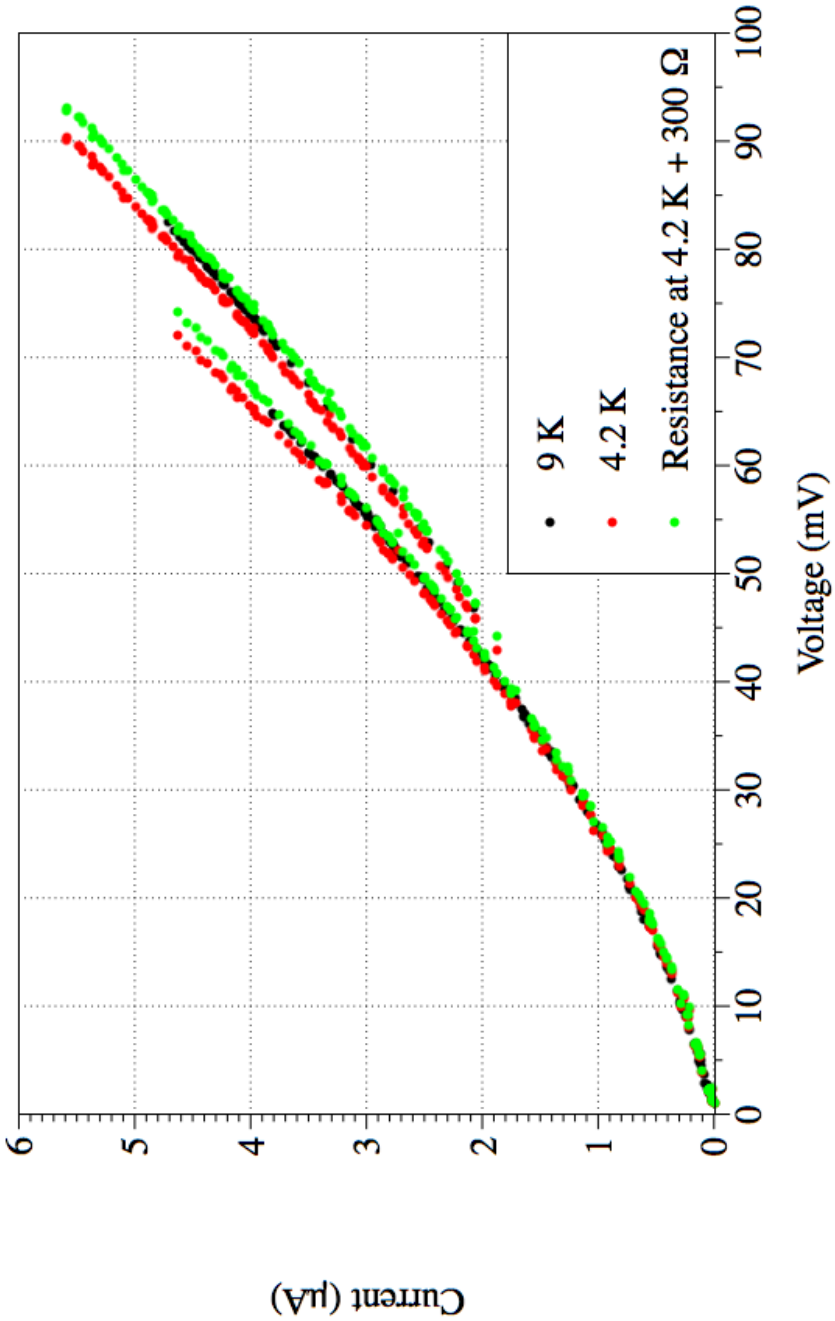

Figure 4.45: First branch of DC IVs shown in Figure 4.43. Data above (black data points) and below (red data points) the tungsten superconducting transition as shown. Green data points are obtained by adding a resistance value of 300 Ω to the tungsten IV below the transition temperature. A good fit between the black and green data points indicates a resistance of 150 Ω per resistor.

A possible reason for the high resistance can be that the switching current of the junction stack is higher than the critical current of the deposited tungsten. It has been established that the critical current of the deposited tungsten is about 40 μA $\pm$ 10 μA, where as the switching current of the IJJ stack is less than 10 μA and hence this can not cause the high resistance to appear. Even if the critical current of the deposited tungsten is exceeded, it is expected that the value of the tungsten resistance would increase to its value above T_c which is between 100 Ω and 500 Ω. Hence we conclude that the resistors and junction stack on their own behave normally and their IV characteristics are as explained above. It is the placing of the two structures together which somehow makes this large resistance come in to play. It seems that the presence of the tungsten (even below its T_c) shifts the supercurrent branch of the IJJ array to finite voltage. More work is needed to understand this behaviour and identify the root cause.

4.7 Summary

This chapter presented the evidence to establish the superconductivity of the samples used in this research. High quality of junction fabrication was established by the observation of fine features like phonon resonance in the IVC. ASO was investigated using SCD measurements. Possible explanations of ASO were discussed. It was shown that ASO is caused by the change in dissipative environment of the junction stack. Switching current measurements under RF showed a higher suppression of switching current for supercurrent branch than the quasiparticle branches. Vortex-flow branch was observed between the supercurrent branch and 1st quasiparticle branch. These observations were explained in terms of change in environmental impedance. IJJ stack was isolated from tis environment using FIB deposited tungsten. Presence of FIB deposited tungsten causes an additional resistance on the supercurrent branch. More work is needed to understand the

origin of this additional resistance.

Chapter 5

Conclusions

This study has been carried out to investigate the dynamical behaviour of Tl2212 thin film IJJ arrays. The main aim of the research was to investigate the phenomenon of uniform switching or ASO. As a first step, Josephson effects from Tl2212 thin film FIB-patterned bridge structures were recorded. The critical temperature, T_c of these films was found to be 110 K, in agreement with previous results. Fine features on the IV were observed which indicated the high quality of the films and fabrication techniques.

ASO was investigated by measuring the switching current distributions when switching from the supercurrent branch with those when switching from the first quasiparticle branch. It was observed that T^* for branch 1 was higher than supercurrent branch. Possible explanations for higher T^* for the first branch were discussed. It was explained that supercurrent branch was overdamped at the escape frequency whereas the first quasiparticle branch was underdamped, resulting in a larger switching current for the former than the latter. Hence, it was concluded that ASO is caused by the change in the dissipative environment of the IJJ array.

The effect of this change in dissipative environment on the RF coupling to the IJJ stack was also investigated. Increased suppression of the switching current for the supercurrent branch was observed as compared to the quasiparticle branches. A flux-flow branch was also observed. These results were explained in terms

of the environment in which the junctions were embedded, and, furthermore, that switching of a single IJJ into the voltage state significantly changes the environmental impedence.

A reliable technique has been developed to make FIB deposited tungsten connections with the IJJ stack. The orientation of the sample with respect to the nozzle position and the surface layer of the sample was shown to have a major effect on the contact resistance. It was shown that FIB-deposited tungsten can act both as a superconductor and a resistor. It was shown that the presence of FIB tungsten results in a large additional resistance of unknown origin on supercurrent branch.

Research work presented in this study can be extended further. One area of further research is to investigate the origin of the high resistance due to the presence of FIB-deposited tungsten in the close proximity to the IJJ stack. Another area of research includes the possibility of observing MQT on the first quasiparticle branch. Observation of MQT at elevated temperatures requires a junction with high plasma frequency ω_p. This is a material property and depends on the critical current density J_c. Observation of MQT on quasiparticle branches requires the self-heating to be lower than the T_{MQT}. In the junction discussed in section 4.4.4.1 with an I_c of 27 μA, the calculated value of T_{MQT} is 3 K and value of self heating ΔT is approximately 10 K as $T \rightarrow 0$. In order to observe MQT on the first quasipartcile branch ΔT needs to be at least one order of magnitude lower than T_{MQT} i.e $\Delta T = 0.3$ K. The value of I_c needs to be reduced by a factor of 30 times to about 1 μA to achieve the desired value of ΔT, assuming the value of thermal resistance does not change. I_c can be reduced by reducing the junction area. The present junction area of 0.25 μm^2 needs to be reduced to about 0.01 μ m^2 (100 nm by 100 nm) for I_c to have a value of 1 μA. Hence it is predicted that MQT phenomena should be observable on the first quasiparticle branch in a junction with I_c of 1 μA, provided the thermal resistance does not change.

References

Ambegaokar, V. & Baratoff, A. (1963). Tunnelling Between Superconductors. *Physical Review Letters*, **10**, 486.

Ambegaokar, V. & Halperin, B.I. (1969). Voltage Due to Thermal Noise in the Dc Josephson Effect. *Physical Review Letters*, **22**, 1364.

Anderson, P.W. (1963). Image of the Phonon Spectrum in the Tunnelling Characteristic Between Superconductors. *Physical Review Letters*, **10**, 334.

Ando, Y., Boebinger, G.S., Passner, A., Wang, N.L., Geibel, C. & Steglich, F. (1996). Metallic In-Plane and Divergent Out-Of-Plane Resistivity of a High- T_C Cuprate in the Zero-Temperature Limit. *Physical Review Letters*, **77**, 2065.

Bae, M.H., Lee, H.J., Kim, J. & Kim, K.T. (2003). Microwave Distribution in Stacked $BI_2SR_2CaCU_2O_{8+X}$ Intrinsic Josephson Junctions in a Transmission-Line Geometry. *Applied Physics Letters*, **83**, 2187.

Barbara, P., Cawthorne, A.B., Shitov, S.V. & Lobb, C.J. (1999). Stimulated Emission and Amplification in Josephson Junction Arrays. *Physical Review Letters*, **82**, 1963–1966.

Bardeen, J., Cooper, L.N. & Schrieffer, J.R. (1957). Microscopic Theory of Superconductivity. *Physical Review*, **106**, 162.

Barkov, F.L., Fistul, M.V. & Ustinov, A.V. (2004). Microwave-Induced Flow of Vortices in Long Josephson Junctions. *Physical Review B*, **70**, 134515.

Barone, A. & Pagano, S. (1994). Weakly Coupled High T_c Superconductors - an Overview. *Journal of Superconductivity*, **7**, 375–380.

Bauch, T., Lombardi, F., Tafuri, F., Barone, A., Rotoli, G., Delsing, P. & Claeson, T. (2005). Macroscopic Quantum Tunnelling in D-Wave $YBa_2CU_3O_{7-\Delta}$ Josephson Junctions. *Physical Review Letters*, **94**.

Bednorz, J.G. & Muller, K.A. (1986). Possible High Superconductivity in the $Ba - La - Cu - O$ System. *Physic B*, **64**, 189.

Benjacob, E., Bergman, D.J., Matkowsky, B.J. & Schuss, Z. (1982). Lifetime of Oscillatory Steady States. *Physical Review A*, **26**, 2805–2816.

Bramley, A.P., O'Connor, J.D. & Grovenor, C.R.M. (1999). Thallium-Based HTS Thin Films, Processing, Properties and Applications. *Superconductor Science and Technology*, **12**, R57–R74.

Bulaevskii, L.N., Domnguez, D., Maley, M.P., Bishop, A.R. & Ivlev, B.I. (1996). Collective Mode and the C-Axis Critical Current of a Josephson-Coupled Superconductor at High Parallel Magnetic Fields. *Physical Review B*, **53**, 14601.

Castellano, M.G., Leoni, R., Torrioli, G., Chiarello, F., Cosmelli, C., Costantini, A., DiambriniPalazzi, G., Carelli, P., Cristiano, R. & Frunzio, L. (1996). Switching Dynamics of $Nb/AlO_X/Nb$ Josephson Junctions: Measurements for an Experiment of Macroscopic Quantum Coherence. *Journal of Applied Physics*, **80**, 2922–2928.

Chana, O.S., Hyland, D.M.C., Kinsey, R.J., Booij, W.E., Blamire, M.G., Grovenor, C.R.M., Dew-Hughes, D. & Warburton,

P.A. (1999). Josephson Effects in Misaligned Tl-2212 Films. *Physica C-Superconductivity and Its Applications*, **327**, 104–110.

Clarke, J. (1989). Principles and Applications of Squids. *Proceedings of the IEEE*, **77**, 1208.

Cooper, L.N. (1956). Bound Electron Pairs in a Degenerate Fermi Gas. *Physical Review*, **104**, 1189.

Darula, M., Doderer, T. & Beuven, S. (1999). Millimetre and Sub-mm Wavelength Radiation Sources Based on Discrete Josephson Junction Arrays. *Superconductor Science and Technology*, **12**, R1–R25.

Delin, K.A. & Kleinsasser, A.W. (1996). Stationary Properties of High-Critical-Temperature Proximity Effect Josephson Junctions. *Supercond. Sci. Technol*, **9**, 227.

Devoret, M.H., Martinis, J.M. & Clarke, J. (1985). Measurements of Macroscopic Quantum Tunnelling out of the Zero-Voltage State of a Current-Biased Josephson Junction. *Physical Review Letters*, **55**, 1908.

Duan, H.M., Kiehl, W., Dong, C., Cordes, A.W., Saeed, M.J., Viar, D.L. & Hermann, A.M. (1991). Anisotropic Resistivity and Paraconductivity of $Tl_2Ba_2CaCu_2O_8$ Single Crystals. *Physical Review B*, **43**, 12925.

Fenton, J.C. & Warburton, P.A. (2008). Monte Carlo Simulations of Thermal Fluctuations in Moderately Damped Josephson Junctions: Multiple Escape and Retrapping, Switching- and Return-Current Distributions, and Hysteresis. *Physical Review B (Condensed Matter and Materials Physics)*, **78**, 054526.

Fenton, J.C. & Warburton, P.A. (2009). Skewness Variations of Switching-Current Distributions in Moderately Damped Josephson Junctions Due to

Thermally Induced Multiple Escape and Retrapping. *Journal of Physics: Conference Series*, **150**, 052052.

Fenton, J.C., Thomas, P.J., Yang, G. & Gough, C.E. (2002). System for Fast Time-Resolved Measurements of C-Axis Quasiparticle Conductivity in Intrinsic Josephson Junctions of $Bi_2Sr_2CaCu_2O_{8+\Delta}$. *Applied Physics Letters*, **80**, 2535.

Fenton, J.C., Korsah, M., Grovenor, C.R.M. & Warburton, P.A. (2007). Switchable Phase Diffusion in Intrinsic Josephson Junction Arrays. *Physica C: Superconductivity*, **460-462**, 1470–1471.

Feynman, R.P. (1966). *the Feynman Lectures on Physics: Volume III*.

Franz, A., Koval, Y., Vasyukov, D., Mller, P., Schneidewind, H., Ryndyk, D.A., Keller, J. & Helm, C. (2004). Thermal Fluctuations in Ultrasmall Intrinsic Josephson Junctions. *Physical Review B*, **69**, 014506.

Fulton, T.A. (1977). *Equivalent Circuits and Analogs of the Josephson Effect*.

Fulton, T.A. & Dunkleberger, L.N. (1974). Lifetime of the Zero-Voltage State in Josephson Tunnel Junctions. *Physical Review B*, **9**, 4760.

Gaifullin, M.B., Latyshev, Y.I., Yamashita, T. & Matsuda, Y. (2003). Shapiro Step Response in $Bi_2Sr_2CaCu_2O_{8+\Delta}$ in Parallel and Tilted Magnetic Field. *Physica C: Superconductivity*, **392-396**, 319–322.

Giaever, I. (1965). Detection of the Ac Josephson Effect. *Phys. Rev. Lett.*, **14**, 904.

Gough, C.E. (1987). Flux Quantization in a High-T_c Superconductor. *Nature*, **326**, 855.

Gough, C.E., Thomas, P.J., Fenton, J.C. & Yang, G. (2000). Quasiparticle Tunnelling and Field-Dependent Critical Current in 2212-BSCCO. In *International Conference on Materials and Mechanisms of Superconductivity High Temperature Superconductors VI*, vol. 341, 1539–1542, Houston, Texas, part 3.

Gross, R., Alff, L., Beck, A., Froehlich, O.M., Koelle, D. & Marx, A. (1997). Physics and Technology of High Temperature Superconducting Josephson Junctions. *IEEE Transactions on Applied Superconductivity*, **7**, 2929–2935.

Helm, C., Preis, C., Forsthofer, F., Keller, J., Schlenga, K., Kleiner, R. & Mller, P. (1997). Coupling Between Phonons and Intrinsic Josephson Oscillations in Cuprate Superconductors. *Physical Review Letters*, **79**, 737.

Helm, C., Odagawa, A., Sakai, M., Adachi, H., Setsune, K. & Kleiner, R. (2000). Interpretation of a Microwave Induced Current Step in a Single Intrinsic Josephson Junction on a Bi-2223 Thin Film. *Physica C-Superconductivity and Its Applications*, **341**, 2645.

Hirata, K., Ooi, S. & Mochiku, T. (2001). Excitation of Josephson Plasma by Josephson Vortex Flow. *Physica C: Superconductivity*, **362**, 114.

Hollmann, E.K., Vendik, O.G., Zaitsev, A.G. & Melekh, B.T. (1994). Substrates for High-T_c Superconductor Microwave Integrated Circuits. *Superconductor Science and Technology*, 609.

Inomata, K., Sato, S., Nakajima, K., Tanaka, A., Takano, Y., Wang, H.B., Nagao, M., Hatano, H. & Kawabata, S. (2005). Macroscopic Quantum Tunnelling in a D-Wave High-T_c $Bi_2Sr_2CaCu_2O_{8+\Delta}$ Superconductor. *Physical Review Letters*, **95**, 107005.

Irie, A. & Oya, G. (1995). Microwave Response of Intrinsic Josephson Junctions in BSCCO Single-Crystals. *IEEE Transactions on Applied Superconductivity*, **5**, 3267–3271.

Irie, A. & Oya, G. (1997). Microwave Phase Locking Steps in Intrinsic J0sephson Junctions of $Bi_2Sr_2CaCu_2O_Y$ Single Crystals. *Physica C-Superconductivity and Its Applications*, **293**, 249.

Irie, A., Sakakibara, M. & Oya, G. (1994). Growth and Tunnelling Properties of $(Bi, Pb)_2Sr_2CaCu_2O_Y$ Single-Crystals. *IEICE Transactions on Electronics*, **E77C**, 1191–1198.

Irie, A., Iwama, M. & Oya, G. (1996). Novel Microwave-Induced Steps of Intrinsic Josephson Junctions in Mesa-Shaped BSCCO Single Crystals. *Superconductor Science Technology*, **9**, A14.

Irie, A., Heim, S., Schromm, S., Moble, M., Nachtrab, T., Godo, M., Kleiner, R., Muller, P. & Oya, G. (2000). *Phys. Rev. B*, **62**, 6681.

Irie, A., Kurosu, Y. & Oya, G. (2003). RF-Induced Steps in Intrinsic Josephson Junctions in $Bi_2Sr_2CaCu_2O_Y$. *IEEE Transactions on Applied Superconductivity*, **13**, 908.

Jackel, L.D., Gordon, J.P., Hu, E.L., Howard, R.E., Fetter, L.A., Tennant, D.M., Epworth, R.W. & Kurkijarvi, J. (1981). Decay of the Zero-Voltage State in Small-Area, High-Current-Density Josephson Junctions. *Physical Review Letters*, **47**, 697.

Jaklevic, R.C. (1964). Quantum Interference from a Static Vector Potential in a Field-Free Region . *Phys. Rev. Lett.*, **12**, 274 – 275.

Jin, X.Y., Lisenfeld, J., Koval, Y., Lukashenko, A., Ustinov, A.V. & Muller, P. (2006). Enhanced Macroscopic Quantum Tunnelling in

$Bi_2Sr_2CaCu_2O_{8+\Delta}$ Intrinsic Josephson Junction Stacks. *Physical Review Letters*, **96**, 177003–4.

Johnson, H.L., Hechtfischer, G., Gotz, G., Kleiner, R. & Muller, P. (1997). Zero-Crossing Steps in Intrinsic Josephson Junctions of $Bi_2Sr_2CaCu_2O_{8+\Delta}.JournalofAppliedPhysics, \mathbf{82}, 756.$

Josephson, B. (1962). Possible New Effects in Superconductive Tunnelling. *Phys. Lett.*, **1**, 251.

Kang, J.H., Kampwirth, R.T. & Gray, K.E. (1989). Superconducting Properties of Magnetron Sputtered High-T_c Thin-Films Containing Oxide Compounds of Yttrium, Bismuth, or Thallium. *IEEE Transactions on Magnetics*, **25**, 2226.

Kashiwaya, H., Matsumoto, T., Shibata, H., Kashiwaya, S., Eisaki, H., Yoshida, Y., Kawabata, S. & Tanaka, Y. (2008). Switching Dynamics of $Bi_2Sr_2CaCu_2O_{8+\Delta}$ Intrinsic Josephson Junctions: Macroscopic Quantum Tunnelling and Self-Heating Effect. *Journal of the Physical Society of Japan*, **77**, 104708.

Kashiwaya, H., Matsumoto, T., Shibata, H., Eisaki, H., Yoshida, Y., Kawabata, S., Tanaka, Y. & Kashiwaya, S. (2009). Switching Dynamics and MQT in Bi-2201 Intrinsic Josephson Junctions. *Physica C: Superconductivity*, **469**, 1593–1595.

Kautz, R.L. (1981). The Ac Josephson Effect in Hysteretic Junctions: Range and Stability of Phase Lock. *Journal of Applied Physics*, **52**, 3528–3541.

Kautz, R.L. & Martinis, J.M. (1990). Noise-Affected I-V Curves in Small Hysteretic Josephson Junctions. *Physical Review B*, **42**, 9903.

Kim, H.J., Chowdhury, P., Kang, W.N., Zang, D.J. & Lee, S.I. (2003). Superconducting Fluctuation Probed by In-Plane and Out-Of-Plane Conductivities in $Tl_2Ba_2CaCu_{O8+Y}$ Single Crystals. *Physical Review B*, **67**, 144502.

Kim, S.J., Latyshev, Y.I. & Yamashita, T. (1999). Submicron Stacked-Junction Fabrication from $Bi_2Sr_2CaCu_2O_{8+\Delta}$ Whiskers by Focused-Ion-Beam Etching. *Applied Physics Letters*, **74**, 1156–1158.

Kimura, T., Miyasaka, S., Takagi, H., Tamasaku, K., Eisaki, H., Uchida, S., Kitazawa, K., Hiroi, M., Sera, M. & Kobayashi, N. (1996). In-Plane and Out-Of-Plane Magnetoresistance in $La_{2-X}Sr_XCuO_4$ Single Crystals. *Physical Review B*, **53**, 8733–8742.

Kivioja, J.M., Nieminen, T.E., Claudon, J., Buisson, O., Hekking, F.W.J. & Pekola, J.P. (2005). Observation of Transition from Escape Dynamics to Underdamped Phase Diffusion in a Josephson Junction. *Physical Review Letters*, **94**, 247002.

Kleiner, R., Steinmeyer, F., Kunkel, G. & Muller, P. (1992). Intrinsic Josephson Effects in $Bi_2Sr_2CaCu_2O_8$ Single Crystals. *Physical Review Letters*, **68**, 2394.

Kleiner, R., Muller, P., Kohlstedt, H., Pedersen, N.F. & Sakai, S. (1994). Dynamic Behaviour of Josephson-Coupled Layered Structures. *Physical Review B*, **50**, 3942.

Kleinsasser, A.W. (2001). High Performance Nb Josephson Devices for Petaflops Computing. *IEEE Transactions on Applied Superconductivity*, **11**, 1043–1049.

Koyama, T. & Tachiki, M. (1996). I-V Characteristics of Josephson Coupled Layered Superconductors With Longitudinal Plasma Excitations. *Physical Review B*, **54**, 16183.

KRAMERS, H.A. (1940). Brownian Motion in a Field of Force and the Diffusion Model of Chemical Reactions. *Physica (Amsterdam)*, **7**, 284.

KRASNOV, V.M., MROS, N., YURGENS, A. & WINKLER, D. (1999). Fiske Steps in Intrinsic $Bi_2Sr_2CaCu_2O_{8+X}$ Stacked Josephson Junctions. *Physical Review B*, **59**, 8463–8466.

KRASNOV, V.M., BAUCH, T. & DELSING, P. (2005a). Probing the Intrinsic Josephson Coupling Potential in $Bi_2Sr_2CaCu_2O_{8+\Delta}$ Superconductors by Thermal Activation. *Physical Review B*, **72**, 212501.

KRASNOV, V.M., BAUCH, T., INTISO, S., HRFELD, E., AKAZAKI, T., TAKAYANAGI, H. & DELSING, P. (2005b). Collapse of Thermal Activation in Moderately Damped Josephson Junctions. *Physical Review Letters*, **95**, 157002.

KRASNOV, V.M., SANDBERG, M. & ZOGAJ, I. (2005c). In Situ Measurement of Self-Heating in Intrinsic Tunnelling Spectroscopy. *Physical Review Letters*, **94**, 077003.

KURTER, C., GRAY, K.E., ZASADZINSKI, J.F., OZYUZER, L., KOSHELEV, A.E., LI, Q., YAMAMOTO, T., KADOWAKI, K., KWOK, W.K., TACHIKI, M. & WELP, U. (2008). Thermal Management in Large Bi2212 Mesas Used for Terahertz Source. *IEEE Transactions on Applied Superconductivity.*, **19**, 428.

KUZMIN, L.S. & HAVILAND, D.B. (1991). Observation of the Bloch Oscillations in an Ultrasmall Josephson Junction. *Physical Review Letters*, **67**, 2890.

LATYSHEV, Y.I., MONCEAU, P. & PAVLENKO, V.N. (1997). Intrinsic Josephson Effects on Stacks Fabricated from High Quality BSCCO 2212 Single Crystal Whiskers. *Physica C: Superconductivity*, **293**, 174–180.

Latyshev, Y.I., Orlov, A.P., Nikitina, A.M., Monceau, P. & Klemm, R.A. (2004). C-Axis Transport in Naturally Grown $Bi_2Sr_2CaCu_2O_{8+X}$ Cross-Whisker Junctions. *Physical Review B*, **70**, 094517.

Lee, P.A. (1971). Effect of Noise on Current-Voltage Characteristics of a Josephson Junction. *Journal of Applied Physics*, **42**, 325.

Li, S.X., Qiu, W., Han, S., Wei, Y.F., Zhu, X.B., Gu, C.Z., Zhao, S.P. & Wang, H.B. (2007). Observation of Macroscopic Quantum Tunnelling in a Single $Bi_2Sr_2CaCu_2O_{8+X}$ Surface Intrinsic Josephson Junction. *Physical Review Letters*, **99**, 037002.

Li, W.X., Fenton, J.C. & Warburton, P.A. (2009). Focused-Ion-Beam Direct-Writing of Ultra-Thin Superconducting Tungsten Composite Films. *IEEE Transactions on Applied Superconductivity*, **19**, 2819–2822.

Likharev, K. (1986). *Dynamics of Josephson Junction and Circuits*. Gordon and Breach Publishers.

Machida, M. & Koyama, T. (2004). Localized Rotating-Modes in Capacitively Coupled Intrinsic Josephson Junctions: Systematic Study of Branching Structure and Collective Dynamical Instability. *Physical Review B*, **70**, 024523.

Machida, M., Koyama, T. & Tachiki, M. (1999). Dynamical Breaking of Charge Neutrality in Intrinsic Josephson Junctions: Common Origin for Microwave Resonant Absorptions and Multiple-Branch Structures in the I-V Characteristics. *Physical Review Letters*, **83**, 4618.

Maksimov, E.G., Arseyev, P.I. & Maslova, N.S. (1999). Phonon Assisted Tunnelling in Josephson Junctions. *Solid State Communications*, **111**, 391–395.

Mandrus, D., Forro, L., Koller, D. & Mihaly, L. (1991). Giant Tunnelling Anisotropy in the High- T_C Superconductor $Bi_2Sr_2CaCu_2O_8$. *Nature*, **351**, 460.

Mannik, J., Li, S., Qiu, W., Chen, W., Patel, V., Han, S. & Lukens, J.E. (2005). Crossover from Kramers to Phase-Diffusion Switching in Moderately Damped Josephson Junctions. *Physical Review B*, **71**, 220509.

Martin, S., Fiory, A.T., Fleming, R.M., Schneemeyer, L.F. & Waszczak, J.V. (1988). Temperature-Dependence of the Resistivity Tensor in Superconducting $Bi_2Sr_{2.2}Ca_{0.8}Cu_2O_8$ Crystals. *Physical Review Letters*, **60**, 2194.

Martinis, J.M. & Kautz, R.L. (1989). Classical Phase Diffusion in Small Hysteretic Josephson Junctions. *Physical Review Letters*, **63**, 1507.

Martinis, J.M., Devoret, M.H. & Clarke, J. (1987). Experimental Tests for the Quantum Behaviour of a Macroscopic Degree of Freedom - the Phase Difference Across a Josephson Junction. *Physical Review B*, **35**, 4682.

McCumber, D.E. (1968). Effect of Ac Impedance on Dc Voltage-Current Characteristics of Superconductor Weak-Link Junctions. *Journal of Applied Physics*, **39**, 3113–3118.

Moreland, J. (1989). Evidence for the Superconducting Proximity Effect in Junctions Between the Surfaces of $YBa_2Cu_3O_X$ Thin Films. *Appl. Phys. Lett*, **54**, 1477.

Mros, N., Krasnov, V.M., Yurgens, A., Winkler, D. & Claeson, T. (1998). Multiple-Valued C-Axis Critical Current and Phase Locking in $Bi_2Sr_2CaCu_2O_{8+X}$ Single Crystals. *Physical Review B*, **57**, R8135.

Norton, D.P. (2004). Synthesis and Properties of Epitaxial Electronic Oxide Thin-Film Materials. *Materials Science Engineering R-Reports*, **43**, 139–247.

Odagawa, A., Sakai, M., Adachi, H. & Setsune, K. (1999). I-V Characteristic of a Single Intrinsic Tunnel Junction on Bi-2223 Thin Film. *IEEE Transactions on Applied Superconductivity*, **9**, 3012–3015.

Ota, K., Hamada, K., Takemura, R., Ohmaki, M., Machi, T., Tanabe, K., Suzuki, M., Maeda, A. & Kitano, H. (2009a). Comparative Study of Macroscopic Quantum Tunnelling in $Bi_2Sr_2CaCu_2O_Y$ Intrinsic Josephson Junctions With Different Device Structures. *Physical Review B (Condensed Matter and Materials Physics)*, **79**, 134505–11.

Ota, K., Maeda, A., Machi, T., Tanabe, K. & Kitano, H. (2009b). Comparison Between the First- and the Second-Junction Switchings in a Small Stack of $Bi_2Sr_2CaCu_2O_Y$ Intrinsic Josephson Junctions. *Journal of Physics: Conference Series*, **150**, 052205.

Oya, G. & Irie, A. (1996). Fluxon Motion in the Stacked Intrinsic Josephson Junctions in $Bi_2Sr_2CaCu_2O_Y$ Single Crystals. *Physica C*, **263**, 453–456.

Oya, G., Aoyama, N., Irie, A., Kishida, S. & Tokutaka, H. (1992). Observation of Josephson Junction-Like Behavior in Single-Crystal $(Bi, Pb)_2Sr_2CaCu_2O_Y$. *Japanese Journal of Applied Physics Part 2-Letters*, **31**, L829–L831.

Ozkan, H., Topal, U., Gasanly, N.M., Albiss, B. & Kayed, T. (1999). Voltage-Current Characteristics of the Thallium-Based Ceramic Superconductors. *Superconductor Science Technology*, **12**, 592–596.

Ozyuzer, L., Koshelev, A.E., Kurter, C., Gopalsami, N., Li, Q., Tachiki, M., Kadowaki, K., Yamamoto, T., Minami, H., Yamaguchi,

H., Tachiki, T., Gray, K.E., Kwok, W.K. & Welp, U. (2007). Emission of Coherent Thz Radiation from Superconductors. *Science*, **318**, 1291.

Phillips, J.M. (1996). Substrate Selection for High-Temperature Superconducting Thin Films. *Journal of Applied Physics*, **79**, 1829–1848.

Poole, C.P. (2007). *Superconductivity*. Elsevier/Academic Press, Amsterdam; Boston.

Preis, C., Helm, C., Schmalzl, K., Walter, C. & Keller, J. (2000). Microscopic Theory of the Coupling of Intrinsic Josephson Oscillations and Photons. *Physica C: Superconductivity*, **341-348**, 1543–1546.

Prestigiacomo, M., Bedu, F., Jandard, F., Tonneau, D., Dallaporta, H., Roussel, L. & Sudraud, P. (2005). *Applied Physics Letters*, **86**, 192112–3.

Prusseit, W., Rapp, M., Hirata, K. & Mochiku, T. (1997). Intrinsic Josephson Junctions Under Microwave Irradiation. *Physica C*, **293**, 25–30.

Rapp, M., Murk, A., Semerad, R. & Prusseit, W. (1996). C-Axis Conductivity and Intrinsic Josephson Effects in $YBa_2Cu_3O_{7-\Delta}$. *Physical Review Letters*, **77**, 928.

Ross, I.M., Luxmoore, I.J., Cullis, A.G., Orr, J., Buckle, P.D. & Jefferson, J.H. (2006). Characterisation of Tungsten Nano-Wires Prepared by Electron and Ion Beam Induced Chemical Vapour Deposition. *Journal of Physics: Conference Series*, **26**, 363–366.

Ruggiero, B., Granata, C., Palmieri, V.G., Esposito, A., Russo, M. & Silvestrini, P. (1998). Supercurrent Decay in Extremely Underdamped Josephson Junctions. *Physical Review B*, **57**, 134–137.

Sadki, E.S., Ooi, S. & Hirata, K. (2004). Focused-Ion-Beam-Induced Deposition of Superconducting Nanowires. *Applied Physics Letters*, **85**, 6206–6208.

Saleem, S., Fenton, J.C., Korsah, M., Speller, S., Grovenor, C.R.M. & Warburton, P.A. (2009). RF-Current Effects on Intrinsic Josephson Junctions. *IEEE Transactions on Applied Superconductivity*, **19**, 734–736.

Schlenga, K., Hechtfischer, G., Kleiner, R., Walkenhorst, W., Muller, P., Johnson, H.L., Veith, M., Brodkorb, W. & Steinbeiss, E. (1996). Subgap Structures in Intrinsic Josephson Junctions of $Tl_2Ba_2Ca_2Cu_3O_{1+\Delta}$ and $Bi_2Sr_2CaCu_2O_{8+\Delta}$. *Physical Review Letters*, **76**, 4943.

Schlenga, K., Kleiner, R., Hechtfischer, G., Mle, M., Schmitt, S., Muller, P., Helm, C., Preis, C., Forsthofer, F., Keller, J., Johnson, H.L., Veith, M. & Steinbei, E. (1998). Tunnelling Spectroscopy With Intrinsic Josephson Junctions in $Bi_2Sr_2CaCu_2O_{8+\Delta}$ and $Tl_2Ba_2Ca_2Cu_3O_{1+\Delta}$. *Physical Review B*, **57**, 14518.

Schulze, H., Behr, R., Kohlmann, J., Muller, F. & Niemeyer, J. (2000). Design and Fabrication of 10 VSINIS Josephson Arrays for Programmable Voltage Standards. *Superconductor Science Technology*, **13**, 1293–1295.

Seidel, P., Pfuch, A., Hbner, U., Schmidl, F., Schneidewind, H., Ecke, T. & Scherbel, J. (1997). One-Dimensional Intrinsic Josephson Arrays Based on HTS Thin Films. *Physica C: Superconductivity*, **293**, 49–54.

Silsbee, F. (1916). A Note on Electrical Conduction in Metals at Low Temperatures. *J. Wash. Acad. Sci.*, **6**, 597.

Simmonds, M. & Parker, W.H. (1970). Thermal Fluctuations in Superconducting Weak Links. *Physical Review Letters*, **24**, 876–.

SMT, C.Z. (2007). 1540XB Crossbeam Original Instructions.

SMT, C.Z. (2008). Software Manual for Smart SEM.

Speller, S. (2003). *Microstructural Development and Control in Tl2212 Thin Films*. Ph.D. thesis.

Stewart, W.C. (1968). Current-Voltage Characteristics of Josephson Junctions. *Appl. Phys. Lett*, **12**, 277.

Subramanian, M.A. (1988). Crystal Structure of the High Temperature Superconductor Tl-2212. *Nature*, **332**, 420–422.

Tachiki, T. & Uchida, T. (2007). Investigation of Microwave-Induced Zero-Current-Crossing Steps Observed in BSCCO Intrinsic Josephson Junctions. *IEEE Transactions on Applied Superconductivity*, **17**, 237–240.

Tachiki, T. & Uchida, T. (2008). Microwave Response of Long Intrinsic Josephson Junctions Fabricated on Bi-2212 Single Crystals. *Journal of Physics: Conference Series*, **97**, 012157.

Tachiki, T., Uchida, T. & Yasuoka, Y. (2003). BSCCO Intrinsic Josephson Junctions for Microwave Detection. *IEEE Transactions on Applied Superconductivity*, **13**, 901–903.

Tachiki, T., Someya, S., Uchida, T. & Yasuoka, Y. (2005). Microwave-Induced Steps Observed in Bi-2212 Intrinsic Josephson Junctions. *IEEE Transactions on Applied Superconductivity*, **15**, 185–188.

Takahashi, H., Igawa, K., Arii, K., Kamihara, K., Hirano, M. & Hosono, H. (2008). Superconductivity at 43 K in an Iron-Based Layered Compound $LaO_{1-X}F_XFeAs$. *Nature*, **453**, 376.

Takeuchi, I., Tsai, J.S., Shimakawaa, Y., Manakoa, T. & Kuboa, Y. (1989). Energy Gap of $Tl - Ba - Ca - Cu - O$ Compounds by Tunnelling. *Physica C*, **158**, 83.

Taur, Y., Richards, P. & Auracher, F. (1974). Application of the Shunted Junction Model to Point-Contact Josephson Junctions. In K. Timmerhaus, ed., *LT-13*, vol. 3, 276–280, Plenum Press, New York.

Tesche, C.D., Kirtley, J.R., Gallagher, W.J., Kleinsasser, A.W., Sandstrom, R.L. & Raider, S.I. (1989). Anomalously Large Josephson Switching Currents in Low Dissipation Josephson Junctions. *IEEE Transactions on Magnetics*, **25**, 1424–1427.

Thomas, P.J., Fenton, J.C., Yang, G. & Gough, C.E. (2000). Intrinsic C-Axis Transport in 2212-BSCCO. In *International Conference on Materials and Mechanisms of Superconductivity High Temperature Superconductors VI*, vol. 341, 1547–1550, Houston, Texas, part 3.

Tinkham, M. (1996). *Introduction to Superconductivity*. New York: McGraw-Hill, 2nd edn.

Van Duzer, T.V. & Turner, C.W. (1998). *Principles of Superconductive Devices and Circuits*. Prentice Hall.

Voss, R.F. & Webb, R.A. (1981). Macroscopic Quantum Tunnelling in 1μm Nb Josephson Junctions. *Physical Review Letters*, **47**, 265–268.

Waldram, J.R. (1996). *Superconductivity of Metals and Cuprates*. Taylor Francis.

Wang, H.B., Aruga, Y., Chen, J., Nakajima, K., Yamashita, T. & Wu, P.H. (2000a). Individual Shapiro Steps Observed in Resistively Shunted

Intrinsic Josephson Junctions on $Bi_2Sr_2CaCu_2O_{8+X}$ Single Crystals. *Applied Physics Letters*, **77**, 1017–1019.

Wang, H.B., Chen, J., Aruga, Y., Tachiki, T., Mizugaki, Y., Nakajima, K., Yamashita, T. & Wu, P.H. (2000b). Investigation of Microwave Responses in BSCCO-2212 Intrinsic Josephson Junctions up to Short Millimeter Wavebands. *Physica C: Superconductivity*, **341-348**, 2737–2738.

Wang, H.B., Wu, P.H. & Yamashita, T. (2001). Stacks of Intrinsic Josephson Junctions Singled out from Inside $Bi_2Sr_2CaCu_2O_{8+X}$ Single Crystals. *Applied Physics Letters*, **78**, 4010–4012.

Wang, N.L. & Ma, Y.C. (2005). Crystal Growth and in Plane Optical Properties of Tl2212 Superconductors. *Physical Review B*, **72**, 104518.

Warburton, P.A. (2007). Coexistence of Linear and Non-Linear Dissipative Branches in the CurrentVoltage Characteristics of Intrinsic Josephson Junction Arrays. *Superconductor Science and Technology*, **20**, S14–S17.

Warburton, P.A., Kuzhakhmetov, A.R., Bell, C., Burnell, G., Blamire, M.G., Wu, H., Grovenor, C.R.M. & Schneidewind, H. (2003a). Sub-Micron Thin Film Intrinsic Josephson Junctions. *IEEE Transactions on Applied Superconductivity*, **13**, 821–824.

Warburton, P.A., Kuzhakhmetov, A.R., Burnell, G., Blamire, M.G. & Schneidewind, H. (2003b). Decoupling of a Current-Biased Intrinsic Josephson Junction from Its Environment. *Physical Review B*, **67**, 184513.

Warburton, P.A., Kuzhakhmetov, A.R., Chana, O.S., Burnell, G., Blamire, M.G., Schneidewind, H., Koval, Y., Franz, A., Muller, P., Hyland, D.M.C., Dew-Hughes, D., Wu, H. & Grovenor, C.R.M. (2004). Josephson Fluxon Flow and Phase Diffusion in Thin-Film Intrinsic Josephson Junctions. *Journal of Applied Physics*, **95**, 4941–4948.

Watanabe, T., Fujii, T. & Matsuda, A. (1997). Anisotropic Resistivities of Precisely Oxygen Controlled Single-Crystal $Bi_2Sr_2CaCu_2O_{8+\Delta}$: Systematic Study on Spin Gap Effect. *Physical Review Letters*, **79**, 2113–2116.

Yan, Y.F., Matl, P., Harris, J.M. & Ong, N.P. (1995). Negative Magnetoresistance in the C-Axis Resistivity of $Bi_2Sr_2CaCu_2O_{8-\Delta}$ and $YBa_2Cu_3O_{6+X}$. *Physical Review B*, **52**, R751.

Yanson (1965). *Sov. Phys.-JETP*, **21**, 655–656.

Yao, N. (2007). *Focused Ion Beam Systems Basics and Applications*. Cambridge University Press.

Young, K.H., Negrete, G.V., Eddy, M.M., Sun, J.Z., James, T.W., Robinson, M. & Smith, E.J. (1991). Comparisons of High Temperature Superconductor Thin Films on Various Substrates for Microwave Applications. *Thin Solid Films*, **206**, 116–121.

Yurgens, A., Winkler, D., Zavaritsky, N.V. & Claeson, T. (1996). Strong Temperature Dependence of the C-Axis Gap Parameter of $Bi_2Sr_2CaCu_2O_{8+\Delta}$ Intrinsic Josephson Junctions. *Physical Review B*, **53**, R8887–R8890.

Yurgens, A.A. (2000). Intrinsic Josephson Junctions: Recent Developments. *Superconductor Science and Technology*, **13**, R85R100.

Appendix A

Published Papers

- RF-Current Effects on Intrinsic Josephson Junctions, **Sajid Saleem**, Jon C. Fenton, Michael Korsah, Susannah Speller, Chris R. M. Grovenor, and Paul A. Warburton, *IEEE Transactions on Applied Superconductivity*, **19**, 734 (2009).

- Dissipative Enhancement of the Supercurrent in $Tl_2Ba_2CaCu_2O_8$ Intrinsic Josephson Junctions, P. A. Warburton, **S. Saleem**, J. C. Fenton, M. Korsah, and C. R. M. Grovenor, *Physical Review Letters*, **103**, 217002 (2009).

- The radio-frequency impedance of individual intrinsic Josephson junctions, Johannes Leiner, **Sajid Saleem**, J. C. Fenton, Takashi Yamamoto, Kazuo Kadowaki, and P. A. Warburton, *Appl. Phys. Lett.*, **95**, 252505 (2009).